UNIVERSITY OF PADOVA
Department of Information Engineering

Ph.D. School on Information Engineering
Curriculum: *Bioengineering* - Cycle: XXX

Simultaneous PET/MRI for Connectivity Mapping: Quantitative Methods in Clinical Setting

---

Headmaster of the School: Prof. Andrea NEVIANI
Supervisor: Prof. Alessandra BERTOLDO

PhD. Candidate: Eng. Erica SILVESTRI

2018

University of Padova

Abstract

Ph.D. School on Information Engineering

Simultaneous PET/MRI for Connectivity Mapping: Quantitative Methods in Clinical Setting

by Eng. Erica SILVESTRI

In recent years, the study of brain connectivity has received growing interest from neuroscience field, from a point of view both of analysis of pathological condition and of a healthy brain. Hybrid PET/MRI scanners are promising tools to study this complex phenomenon. This thesis presents a general framework for the acquisition and analysis of simultaneous multimodal PET/MRI imaging data to study brain connectivity in a clinical setting. Several aspects are faced ranging from the planning of an acquisition protocol consistent with clinical constraint to the off-line PET image reconstruction, from the selection and implementation of methods for quantifying the acquired data to the development of methodologies to combine the complementary informations obtained with the two modalities. The developed analysis framework was applied to two different studies, a first conducted on patients affected by Parkinson's Disease and dementia, and a second one on high grade gliomas, as proof of concept evaluation that the pipeline can be extended in clinical settings.

Università degli Studi di Padova

Sommario

Scuola di Dottorato in Ingegneria dell'Informazione

Acquisizioni simultanee PET/MR per lo studio della connettività: metodi quantitativi in ambito clinico

di Ing. Erica SILVESTRI

Lo studio della connettività cerebrale ha recentemente ricevuto un crescente interesse da parte delle neuroscienze, sia da un punto di vista di analisi della condizione sana che patologica. Gli scanner ibridi PET/MRI sono strumenti potenzialmente molto utili per studiare questo complesso fenomeno. In questo lavoro di tesi è stato messo a punto un quadro generale per l'acquisizione e l'analisi di dati simultanei PET/MRI, al fine di poter studiare in modalità multimodale la connettività cerebrale in un ambiente sperimentale di tipo clinico. Diversi aspetti sono stati affrontati a partire dalla pianificazione di un protocollo di acquisizione coerente con il vincolo clinico alla ricostruzione dell'immagine PET, dalla selezione e implementazione di metodi per la quantificazione dei dati acquisiti allo sviluppo di metodologie per combinare le informazioni complementari ottenute attraverso le due modalità. Il quadro di analisi sviluppato è stato applicato a due diversi studi, un primo condotto su pazienti affetti da malattia di Parkinson e demenza, ed un secondo su gliomi di alto grado.

Contents

Chapter 1

Introduction

1.1 Background

In the recent decades, the study of the brain connectivity has attracted the functional brain imaging neuroscience community, so that a quick research on Pubmed reports almost 15000 articles on it since 1975, when the work of Legendy (Legéndy, 1975) was published. This appealing term refers to the fact that neurons and neural populations do not function as islands onto themselves. Rather, they interact with other such elements through their afferent and efferent synaptic connections in an orchestrated manner so as to enable different sensorimotor and cognitive tasks to be performed (B. Horwitz, Duara, and Rappoport, 1984) as well as resting state fluctuations (Barry Horwitz, 2003), according to the concepts of segregated and integrated brain functioning (Friston, 2011). The connectivity studies typically performed in clinical settings can be classified in two main fields: structural and functional connectivity.

Structural studies start from the observation that in order for an interaction to occur, the presence of a physical substrate, i.e. physical connections between neuronal population or wider brain regions carried by axons is necessary. From a whole-brain perspective, structural connectivity (SC) analysis is concerned with describing and quantifying the complex network of links made by the white matter bundle within the brain (Lang et al., 2012) and is commonly investigated using diffusion tensor imaging (DTI) magnetic resonance approaches. In particular, DTI exploits the diffusive properties of water molecules to estimate the location, orientation of the brain's white matter tracts. Although well established mathematical models that describe how diffusion processes are linked to white matter bundle are available in literature (Hoy and A. L. Alexander, 2015) (i.e. diffusion tensor model (Basser, 1995), the constrained deconvolution tractography (Tournier, Calamante, and Connelly, 2007) or micro-structural models (H. Zhang et al., 2012;

Novikov, Kiselev, and Jespersen, 2018)), each of them require that the acquired DTI images have specific characteristics in terms of signal to noise ratio (SNR), voxel size, number and magnitude of applied gradient field that need to be fulfilled and take into account when a connectivity study is designed in order to match the hypothesis of the model itself (H. Zhang et al., 2012; D. C. Alexander and Barker, 2005; Tournier, Mori, and Leemans, 2011). Functional connectivity (FC), on the other hand, is defined as the temporal coincidence of spatially distant neuro-physiological events (Friston, 1994; Friston, 2011), and was firstly observed by Friston and colleagues in a study conducted on positron emission tomography data (Friston et al., 1993). In this context, therefore, two brain regions, neural populations or single neurons are considered to have a functional connection if there is a statistical relationship between any measures of their activities. In some ways FC represents the intuitive notion that when two things happened together these two should be related each other (B. Biswal, 2015). Based on the spatial and temporal resolution that one wants to achieve in describing that link, different techniques are available. Those techniques range from microelectrode array for cellular-resolution electrophysiology, to electro- and magnetoencefalography for near whole-brain high temporal resolution measurement of the electrophysiological neuronal activity, to blood-oxygen-level dependent (BOLD, Ogawa et al., 1990) functional magnetic resonance imaging (MRI) for whole-brain high spatial resolution measurement (B. Biswal et al., 1995), and allow researchers to study brain networks during task dependent states or resting states. Electro- and magneto-physiological signals represent a direct measure of the neuronal or regional activity, while, the BOLD contrast imaging is based on changes in blood flow, volume, and oxygen consumption indirectly associated with neuronal activity (Glover, 2011). Although these two approaches convey rather complementary functional information, the latter is the most employed in studying functional connectivity (almost six times more used, according to Pubmed), probably due to the high accessibility of MR scanner in clinical settings, to the supposed-to-be greater ease of use and to the extensive presence of user-friendly analysis toolbox. As for diffusion imaging, when one is involved in the planning a BOLD-based functional connectivity study it is of fundamental importance to take into account some constraints such as the voxel size, the sampling frequency, the temporal signal to noise ratio (Renvall, Nangini, and Hari, 2014). Indeed, as quantifying FC relies basically in computing a correlation, each single source

of noise in data, such as motion, breathing or other artefactual high time-variant noise, could potentially lead to biased estimates.
Despite the limitations due to the quality of the data acquired in the clinical environment, in the last few year, the clinical study of connectivity, was it structural or functional, proved to be a captivating and useful tool to describe and characterize the pathological brain functioning. In particular, several studies have shown how alteration in connectivity are suggestive of neurologic or psychological disorders (Azeez and B. B. Biswal, 2017). Depending on the underlying pathology, different type of misconnections has been observed, in particular, the link between two regions or resting state networks could be increased, as in case of partial functional reorganization or iperconnectivity, or, on the opposite, decreased or completely disrupted, as for the disconnectivity phenoma revealed by studies conduced on patients with schizophrenia (Coyle et al., 2016). Indeed, disturbances in brain regions physical interconnection or joint activity have been reported for a number of pathological states (Fox, 2010), including Alzheimer's disease (Grothe and Teipel, 2016; K. Wang et al., 2007), multiple sclerosis (M. Rocca et al., 2012; M. A. Rocca, De Meo, and Filippi, 2016; Schoonheim et al., 2015; Tona et al., 2014), depression (Greicius et al., 2007; Sheline et al., 2010; Wise et al., 2017; X. Zhu et al., 2017), schizophenia (Yuan Zhou et al., 2008; Singh et al., 2015; Sheffield and Barch, 2016), epilepsy (Chiang and Haneef, 2014) and spatial neglect following stroke (B. J. He et al., 2007).
Beside functional and structural connectivity, it is possible to study the interaction between different regions, through the underpinning physiological processes that are linked to the observed neuronal activity, such as glucose metabolism or blood flow, and to the transmission of information, such as the release of specific neurotransmitters or presence of specific receptor systems. From a clinical perspective, also measures of ongoing pathophysiological processes, e.g. the deposition of βamyloid in Alzheimer's disease or Parkinson's disease, play an important role in the description of altered connectivity. For this purpose, positron emission tomography (PET) with its high biological specificity and selectivity in following functional dynamic processes in the brain, is the modality of choice for molecular imaging (Pichler et al., 2008). In fact, depending on the employed radiotracer it allows to derive a large amount of physiological and pathophysiological parameters such as cerebral blood flow, glucose metabolism, neuroreceptor binding, tissue inflammation, protein synthesis, tau and βamiloid burden, etc. When planning this type of study, after selecting the appropriate tracer, in order

to relate the radioactivity measured with PET to the underlying processes two steps are required. First of all, PET coincidence measures need to be reconstructed into a dynamic or static image accordingly to the subsequent analysis protocol. Then it is necessary to describe the dynamic behaviour of the tracer in the tissues by means of mathematical models that need to be estimated and validated.

A multimodal approach to the study of pathological connectivity has several advantages because of the opportunity of relating the functional alteration to the pathological processes that occurs in the affected tissues, and potentially to overcome the gap in understanding the neurobiological mechanism through which pathology impact connectivity. The clinical literature of recent years shows how some groups have worked in this direction, using separately acquired PET and MRI data. For example, similar altered spatial pattern of connectivity, metabolism and amiloid load were found in Alzheimer's disease (Grothe and Teipel, 2016; Mattsson et al., 2014; Elman et al., 2016; Pasquini et al., 2017; Taylor, Kambeitz-Ilankovic, Gesierich, Simon-Vermot, Franzmeier, Caballero, et al., 2010), or dopaminergic PET imaging and BOLD fMRI were employed to understand striatal dopamine modulation of functional connectivity networks in Parkinson's disease (Baik et al., 2014; Lebedev et al., 2014).

On top of these first interesting results, hybrid PET/MRI scanners are the promising tools to deal with multimodal studies aimed at delving the complex phenomenon of brain connectivity, as they allowed acquiring concurrently structural and functional informations as well as estimates of physiological and pathophysiological underlying processes (Aiello, Cavaliere, and M. Salvatore, 2016; Cecchin et al., 2017). Indeed, those scanners allow to perform multimodal imaging combining the PET high specificity for physiological processes with several MR based measures.

Both PET and MRI techniques suffer from the high intra-individual variability in estimates, which is related to the observed cerebral function and cognitive processing as well as to the technique itself (Tyler et al., 1988; Maquet et al., 1990; B. Chen et al., 2015). For example, glycaemia pre-scan levels, body temperature, sleep status, and haematic changes are known to significantly alter the glucose consumption rate and thus to bias ^{18}F-FDG metabolism estimates. While, BOLD contrast could be altered by several factor such as age, spurious signal variabilities associated with vascular, haemodynamic and respiratory characteristic. For these reasons, concurrent measurements of PET and MRI data have the potential of an increased sensitivity due to the

minimization of the physiological variability and minimizing differences of potential confounds affecting of each technique (Cecchin et al., 2017).
In the last few years, a number of concurrent PET/MRI studies have focused on linking brain metabolism to functional connectivity and brain activity in healthy subjects (Cecchin et al., 2017; Wehrl et al., 2013; Savio et al., 2017; Thompson et al., 2016; V. Riedl et al., 2014; Aiello, E. Salvatore, et al., 2015; Valentin Riedl et al., 2016), while only one study, to our knowledge, has attempted to extend this type of analysis to pathological conditions (Tahmasian et al., 2016). And no study was conducted to relate physiological and pathophysiological processes other than metabolism with connectivity, although this is a potentially very interesting field of application particularly for the clinic.

1.2 Aim

The aim of the work of thesis was to develop a general framework for the acquisition and analysis of simultaneous PET/MRI data to study brain connectivity in a clinical experimental setting. Several aspects have to be faced during this optimization process ranging from the planning of an acquisition protocol consistent with clinical constraint to the off-line PET image reconstruction, from the selection and implementation of methods for quantifying the acquired data to the development of methodologies for combining the multimodal informations obtained with the two modalities. Moreover, the developed analysis framework was applied to two different clinical studies in order to verify its suitability for the study and characterization of pathological alterations of connectivity.

1.3 Outline of the Thesis

In the following list is reported a summary of the topics covered by each chapter.

- **Chapter 2: Hybrid PET-MRI scanner**
  A brief introduction to simultaneous PET/MRI acquisitions is given. An overview of the overall structure of the scanners, the technological solutions implemented over the years, and the currently commercially available scanner is provided.

- **Chapter 3: Framework for Simultaneous PET/MRI Study of Brain Connectivity**
  Here is detailed the process that led us to define a suitable framework for the integrated study of connectivity. The chapter is focused on four main points: the planning of a pipeline for off-line reconstruction of PET images, the optimisation of the dynamic PET reconstruction sampling grid for image derived input function (IDIF) extraction, the development of a method to obtain a proxy of the cerebral blood flow from the first samples of the PET time activity curve, and, finally, the set-up of the MR acquisition protocol, including the tuning of sequences, required for structural and functional connectivity study.

- **Chapter 4: Multimodal Approaches to Connectivity Analysis in Parkinson's Disease**
  In this chapter the results obtained by applying the pipeline described in Chapter 3 to a small cohort of patients with Parkinson's Disease are reported and discussed. A method for integrating MR and PET feature is also presented.

- **Chapter 5: Connectivity Mapping in Brain Tumour: A Case Study**
  The chapter provides a second example of the feasibility of the introduced framework, which is here applied to a brain tumour case study.

- **Chapter 6: Conclusions**
  Performance evaluation, according to the preliminary results reported in Chapter 4 and Chapter 5, as well as limitation of the proposed pipeline of analysis are discussed.

Chapter 2

Hybrid PET-MRI Scanner

The idea of combining PET and MRI scanner in a single acquisition system, capable of simultaneously acquiring both datasets, was suggested in the early-mid 1990s (B. E. Hammer, 1991; Bruce E. Hammer, Christensen, and Heil, 1994). The integration was motivated by the complementary nature of the information that can be obtained by these two imaging techniques(Catana, 2017). Indeed, on one hand, PET allows imaging of a wide range of physiological, pathological and biological processes with an high sensitivity but low spatial resolution, while, on the other, MRI provides soft tissue high spatial resolution anatomical images and functional images with good spatial resolution. Albeit the two technique are mostly complementary, when comparing and combining their results it is necessary consider the mismatch in terms of biological specificity and quantitativeness between them. In fact, MR-derived features are generally not quantitative and exhibit a biological specificity which is several orders of magnitude smaller than that of positron emission tomography imaging (Catana, 2017).
As due to the physical characteristics of the two imaging systems, several challenges has to be faced during the development of hybrid scanners and some unsolved problems are still present, a licit question one can rise is "Is it really necessary acquiring functional PET and MR data simultaneously?" The answer to this question is yes, the effort required is absolutely worthwhile. Indeed, as suggested in (Pichler et al., 2008; Cecchin et al., 2017), the need of temporal matching between the two acquisition is justified by a number of biological considerations such as the high inter- and intra-subject results variability. Moreover, concurrent acquisition are compulsory for a wide class of studies, i.e. the analysis of the effect of drug on receptor occupancy on blood flow proposed by (Sander et al., 2013; Vidal et al., 2017), or the assessment of the the relationship between specific receptor systems response and changes in functional connectivity as reported by (Atzil et al., 2017).
Prototype of MRI-compatible PET scanner for simultaneous imaging of small

animals started to appear in the mid 2000s (Raylman, Majewski, et al., 2006; Schlyer et al., 2007), while only after a period of 15 years devices for human simultaneous acquisitions became available. In contrast to the process of integration between PET and CT, in order to be able to combine the two systems, it was necessary to address a number of technological problems related to the interference that the two systems have on each other, as the goal has been a full integration with limited degrading of the optimum performance of both PET and MRI system (Pichler et al., 2008; Gaspar Delso and Ziegler, 2009; Vandenberghe and Marsden, 2015; Catana, 2017).

2.1 Challenges of PET/MRI system

The main challenge in combining PET and MRI was to develop PET detectors MR compatible, as standard detectors could not be placed in the isocentre of an MRI scanner since their scintillation elements are highly susceptible to magnetic field (Harald H. Quick, 2014; Vandenberghe and Marsden, 2015). However, other phenomena related to mutual interference might also take place, as the project of the integration of the two systems required that the two were installed concentrically with PET scanner housed within the MR one, as depicted in Figure 2.1. Because of this configuration, indeed, the

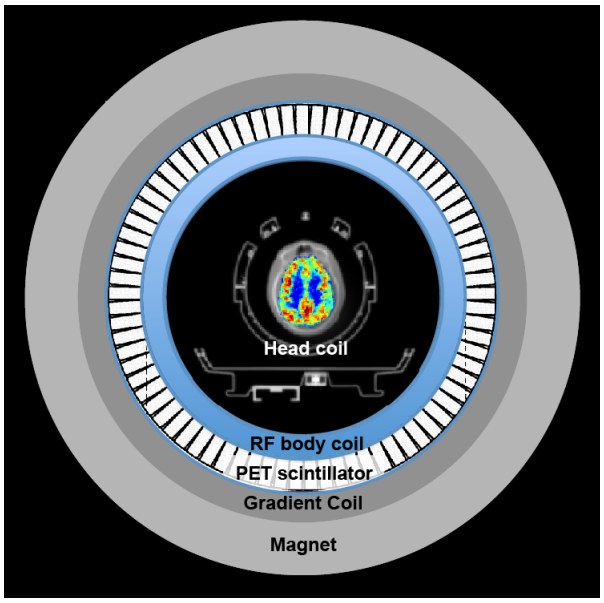

Figure 2.1: Schematic representation of hybrid PET-MR scanner.

MR static field (B_0) for hydrogen spin alignment of the sample, the radio-frequency (RF) and the spatial encoding gradients employed to generate and measure the MR signal are expected to substantially alter the PET signal (Pichler et al., 2008). In particular, B_0 tends to perturb the path of electrons within the detectors resulting in a loss of the gain, while, the rapid switching of MR gradient and radio-frequency fields could induce eddy current loops in conductive components that interfere with signal and can lead to heating and mechanical vibrations, and, finally, RF generated by the transmit coil interferes with any electronics arranged within the magnet bore and this can cause a drop in PET count rate (Vandenberghe and Marsden, 2015). In addition, as the body coils are placed inside the PET field of view, an additional element that absorbs gamma radiation lies between the source and the detectors and contributes to PET signal attenuation.

Conversely, from the MR point of view, the presence of PET detectors inside the gradient coil and magnet could prevent the MRI scanner from working properly. Indeed, MR scanners are built to achieve very uniform B_0 strength, so that the protons resonate at virtually the same frequency, but, when materials such as the scintillators, are placed in the magnet, the local magnetic field strength locally changes. This causes the protons to spin at altered frequencies, resulting in severe geometrical distortions and susceptibility artefacts. Moreover, PET electronics and power cables could interfere with radio frequency detection inducing degradation of the MR images (Muzic and DiFilippo, 2015).

Over the years, several strategies were carried out to overcome the previously mentioned set of problems. First of all, MR-compatible materials has been used both for scintillators and PET electronics and shielding. MR compatibility depends on the materials' magnetic susceptibility, i.e. the degree to which the material is magnetized when placed in a magnetic field. Materials having high magnetic susceptibility must be avoided in the PET detectors and integrated electronics. The most widely used PET scintillators, that do not contain gadolinium, have a magnetic susceptibility similar to that of human tissue and have been demonstrated to have negligible effects on MR. Even in this case some degree of field distortion is inevitable and needs to be compensated by shimming. Measurement of the static magnetic field and the linear field gradient in a commercial simultaneous PET/MR system compared to its base MR-only system demonstrated that the inhomogeneity caused by the PET detectors in integrated PET/MR is negligible (Muzic and DiFilippo, 2015).

In the meanwhile, PET detectors that are insensitive to magnetic fields were developed. The photomultiplier tubes (PMT) commonly used in PET scanners, have been replaced by avalanche photodiodes (APD), the first photon detectors that were found to work even inside ultra–high-field magnets (Vandenberghe and Marsden, 2015). Besides, APDs were very compact compared with PMTs, which was advantageous considering the limited space inside the gantry of an MR scanner. More recently, Geiger mode APDs (also called solid-state photomultipliers, silicon photomultipliers (SiPMs) or multiphoton pixel counters) have emerged as promising candidates for replacing APDs as the photon detector of choice for simultaneous PET/MR imaging, as they have shown to have better timing properties (Vandenberghe and Marsden, 2015).
Finally, in order to reduce the impact on PET detectors sensitivity, maintaining a high MR sensitivity, MRI radio-frequency coils were redesigned and built using minimally attenuating materials.

2.2 PET/MRI Scanners for Human Simultaneous Acquisitions

Currently, if we consider clinical acquisition systems that allow simultaneous imaging, only two hybrid PET/MRI scanners approved by Food and Drug Administration (FDA) are commercially available: the Siemens Biograph mMR (Siemens Healthcare Sector, Erlangen, Germany) and the General Electric (GE Healthcare, Waukesha WI, USA) Signa PET/MR (Ladefoged et al., 2017). Siemens was the first to introduce a fully integrated whole-body PET/MR scanner, in 2010, when the first Biograph mMR was installed at the Technical University of Munich (Muzic and DiFilippo, 2015). This hybrid system comprises a 3.0T whole-body MR system with a length of 199 cm (magnet length 163 cm) that hosts a fully integrated PET detector in its magnet isocentre providing a 60cm diameter patient bore. It is based on the Verio 3.0T MR platform which was modified to house the PET detectors, electronics and cooling system. Maximum gradient strength is 45 mT/m in all three axes and maximum slew rate is 200 T/m/s. The field of view (FOV) of the MR system is specified to 50x50x45 cm^3 . The PET detectors that exploit the APD technology are positioned between the radiofrequency coil and the gradient set. A total of 56 LSO-APD detector blocks, each consisting of 8x8

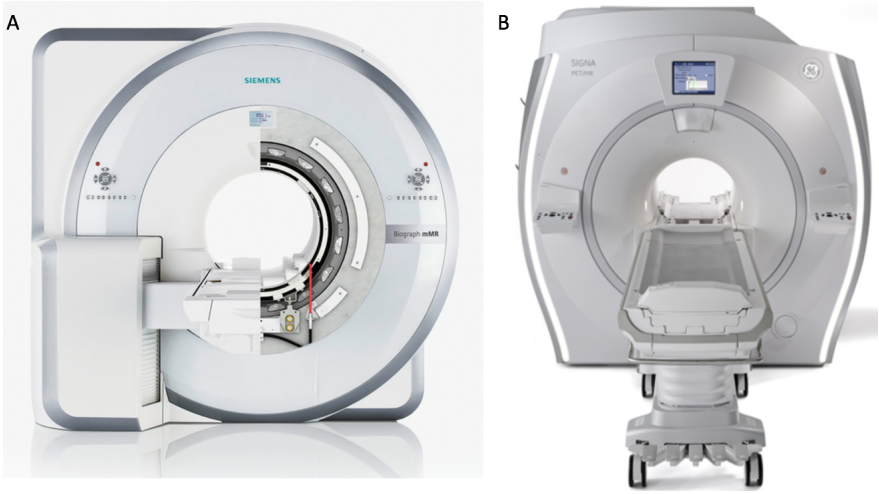

Figure 2.2: Commercially available integrated PET/MR imaging scanners for human use: Siemens Biograph mMR (panel A, www.healthcare.siemens.it/magnetic-resonance-imaging/mr-pet-scanner/biograph-mmr); General Electric Signa PET/MR (panel B, www.gehealthcare.com/en/products/categories/magnetic_resonance_imaging/3-0t/signa_pet-mr)

array of crystal elements with a block area of 32x32mm^2 coupled to an array of 3x3 APDs, are aligned circumferentially to form one PET detector block ring. Eight detector block rings form the full PET detector unit, spanning a field of view of 25.8 cm in z-direction, and a transaxial field of view of 59.4cm. The timing resolution is 2.93 ns (so the system does not allow time-of-flight (TOF) acquisition), the spatial resolution is 4.3 mm full width at half maximum (FWHM) at 1 cm offset from the centre of the field of view, and the scanner sensitivity is 15.0 kcps/MBq. The patient bed and coils are modified to reduce the attenuation of 511 keV photons (G. Delso, Furst, et al., 2011). The system permits list mode acquisition of PET data in 3-dimensional mode (Vandenberghe and Marsden, 2015; Catana, 2017).

General Electric introduced the first whole-body SiPM-based integrated PET-MR imaging scanner, Signa PET/MR, in 2013. The MR component of the Signa PET/MR scanner consists of a 60cm bore 3.0T permanent magnet, gradient coils (44 mT/m amplitude and 200 T/m/s slew rate), and transmit/receive body coils similar to the original GE 3.0T Discovery 750w MR system on which it is based. The PET components are placed between the radiofrequency shield of the body coil and the gradient coils, with a total detector thickness (including electronics and cooling) of less then 5cm. The PET gantry is made up of 28 modules consisting of 20 detector blocks made up of a 4x9 array of 4.0x5.3x25mm^3 lutetium-based scintillator, the readout is done

with a 1x3 arrays of analogue SiPMs. The timing resolution is less than 400ps (which allows time-of-flight (TOF) acquisition), the spatial resolution is 4.4 mm FWHM at 1cm offset from the centre of the field of view, and the scanner sensitivity is 23.3 kcps/MBq (Vandenberghe and Marsden, 2015; Catana, 2017).

The major difference between the two hybrid scanners is the TOF capability, which is only present in GE SIGNA PET/MR system. TOF PET refers to the detection of positron annihilation protons with an extremely high temporal accuracy that can be used to estimate the annihilation point between the two detectors that recorded the event by looking at the difference in arrival times between the two protons (Bailey et al., 2005). Indeed, provided that the the difference in arrival time (Δt) measurement is sufficiently accurate, knowing Δt and the speed at which the photons travel from the annihilation point to the detectors (i.e. the speed of light, c), one can obtain a good estimate of the event's position (that is the distance from the origin of the scanner, Δx) via the relation: $\Delta x = c\Delta t/2$ (Vandenberghe, Mikhaylova, et al., 2016). For this reason a good temporal accuracy could potentially lead to less blurred images (Bailey et al., 2005). Thus, the main advantage of including TOF information is that the PET data signal-to-noise ratio improves if compared with non-TOF acquisitions, at least from a theoretical perspective. However recent studies reported limited improvements in image qualities (Catana, 2017), that are probably due to the TOF performance of current generation PET/MRI scanners, if compared with PET/CT acquisition systems.

2.3 Attenuation Correction in Hybrid PET/MRI Scanner

Beside material and technical developments that made it possible to reliably insert PET detectors into an MR environment, one of the major challenge that has been faced in order to use the PET/MRI equipment was to develop robust methodologies for attenuation correction (AC). This is still an open issue (Ladefoged et al., 2017).

To provide a valid quantification of tracer activity, PET data need to be attenuation corrected before performing image reconstruction. Indeed, the annihilation protons are absorbed by scanner hardware components (i.e. scanner bed, positioning aids, RF coils, body coils, etc.) as well as by patients tissues interposed between the emitting source and the PET detectors, and this

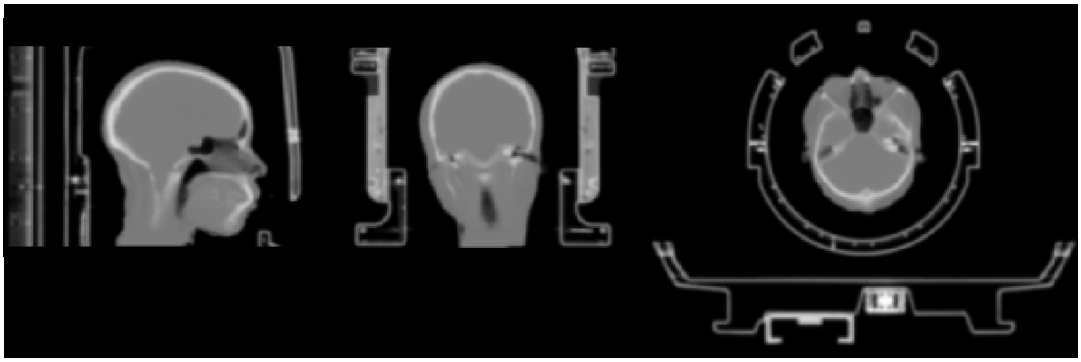

Figure 2.3: Example of complete attenuation map (μmap) for attenuation correction in hybrid PET/MRI imaging system (sagittal, coronal and transversal view). The μmap includes the CT-based hardware attenuation map of RF head-neck coil and the scanner table, clearly visible in the transversal view, and the spatial pattern of bone, soft tissues and air of the patient's head and neck.

Figure 2.4: 3D render of a complete μmap. The μmap includes the CT-based hardware attenuation map of RF head-neck coil and the scanner table (yellow scale), and the spatial pattern of bone, soft tissues and air of the patient's head and neck (grey scale).

reduces the number of detected true annihilation events and consequently leads to systematic quantification error and biased quantification (Daniel H. Paulus and Harald H. Quick, 2016). In particular, photon attenuation can result in as high as 90% signal reduction in some regions (Keereman, Mollet, et al., 2013). For this reasons, performing attenuation correction is fundamental in quantitative imaging. To do so, as will be discuss later in this chapter a proper map of the attenuation properties of tissues and environment, the so-called μmap, is compulsory for quantitative studies. An example of a complete attenuation map is depicted in Figure 2.3 and in Figure 2.4. The reconstruction of PET images is based on the fact that the acquired data in the form of sinograms represent the number of coincidence events detected by photomultipliers and that this number is proportional to the amount of

tracer content assessed along single projection of detection or line of response (LOR). However,several physical phenomena affect the coincidence detection and should be taken into account before and during performing the image reconstruction, i.e. detector efficiencies variation, presence of random coincidences, scattered coincidences, photon attenuation, dead time and activity decay (Bailey et al., 2005; Henkin et al., 2006; Federico E. Turkheimer, Veronese, and Dunn, 2014). In particular, detection efficiency of detector pair varies from pair to pair because of non-uniformities in individual detectors efficiencies, geometrical variations and detector electronics. Random and scatter coincidence are background events that degrade the quality of the resulting images (i.e poor contrast), and refer respectively to detection by a pair of detector of two unrelated photons from two separate positron annihilation location and to detection of photons. And finally, dead time refers to the time interval between the instant in which the photon interacts with the detector and the instant in which, through the system electronics, the position of the event is counted. During this time, the detection system is unable to process a second event, which will be lost (Henkin et al., 2006; Saha, 2010). Among these phenomena, the one that requires a PET-MRI ad-hoc correction methods development is the attenuation, because for the remaining methodologies already developed in the PET field can be borrowed.
Photon attenuation is due to the interaction of gamma radiation with the matter at atomic level. The primary interaction mechanism at energy around 511 keV is by a Compton interaction, which results in loss of energy and change of direction of the photon. From a physical perspective the attenuation is a function of the photon energy and the electron density of the material traversed by the photon to reach the detector. Mathematically, the magnitude of photon transmission through an attenuating object can be expressed by the following exponential equation:

$$\Phi = \Phi_0 \exp\left[-\int_S \mu(x,y)\mathrm{d}r \right] \tag{2.1}$$

where Φ and Φ_0 are the incident and transmitted photon fluencies and $\mathrm{d}r$ is the differential of the thickness of the tissues crosses by the photon beam along the path S. The parameter μ is the linear attenuation coefficient and represents a measure of the probability that a photon will be attenuated while passing through a unit length of the medium (Saha, 2010; Berker and Y. Li, 2016). In the case of positron emission tomography, as the system records two anti-parallel photons that traverse the total tissue thickness, the equation 2.1

can be reduced to:

$$C = C_0 \quad e^{-\mu S} \tag{2.2}$$

where C and C_0 are respectively the probability of counting both anti-parallel photon by detectors and the probability of the annihilation event. Therefore, the problem of correcting for photon attenuation in the body is that of determining the probability map of attenuation of all sources lying along a particular LOR (Zaidi and Hasegawa, 2003).

Therefore, while correcting PET data for attenuation, the main challenge relies in finding reliable attenuation correction factors that compensate for photon detection loss. These factors are typically computed as the inverse of the attenuation map. The attenuation map should contain information about the spatial distribution of the linear attenuation coefficient and accurately delineate the contours of the patient's anatomy that is included in PET camera field of view (T. C. Lee et al., 2016). Since the advent of combined PET/CT scanner in 2001, the AC problem had been considered solved as computed tomography images inherently represent a three-dimensional spatial distribution of tissue density and hence can provide an accurate patient's specific μmap. Before applying the CT-based correction factor to the PET data, the only additional step that should be performed is converting Hounsfield unit (HU) of CT into the linear attenuation coefficient at the photon energy radionuclide, i.e. at 511 keV. This conversion commonly consist in a scaling process that involves an experimentally measured and linearly or bi-linearly approximated transform, that is optimized for human tissues and depends on the acquired CT peak voltage (Kinahan et al., 1998; Zaidi, Montandon, and Alavi, 2007). Although the CT-AC method suffers from a number of limitation, such as metal-induced or beam-hardening artefacts, it is considered the clinical gold standard approach to AC (Y. Chen and An, 2017), and the ground truth also for the development magnetic resonance based AC (MR-AC) methods (Ladefoged et al., 2017).

When dealing with PET/MRI equipment, the attenuation map is obtained as the sum of a μmap of the fixed system component with a patient's μmap. Indeed, as proven in several studies, even for optimized coil designs with least attenuation effect, the attenuation correction must not be omitted, as the design of completely PET-transparent RF coil is not yet possible (Eldib et al., 2016). Concerning the rigid hardware components, as their peculiar absorption characteristics are stationary, the related μmap is commonly generated, memorized and made available within the image reconstruction PET/MRI software by the vendor (Eldib et al., 2016). The μmap is typically computed

from the CT scan of the equipment (i.e. RF coils and scanner's table) by converting the HU values to linear attenuation coefficient at 511 keV (Daniel H. Paulus and Harald H. Quick, 2016) as described in (Carney et al., 2006). To note that, as the equipment is made of plastic and electronics that show attenuation higher than human tissues, for this conversion instead of employing the previously mentioned brain linear or bilinear transform, it is necessary to adapt it to this kind of materials (D. H. Paulus, Tellmann, and H. H. Quick, 2013).

Whereas, considering the high variability observed among the human head morphology, for each patient it is fundamental to determine a specific photon attenuation map that delineates the single subject specific anatomical pattern of absorption. Although in conventional PET/CT scanner the human μmap is computed from a patient's CT scan, CT image is not generally available in integrated PET/MRI studies. Hence, the μmap should be obtained from suitable MR data (Y. Chen and An, 2017). Several MR-based methods had been proposed in the last few years to address this problem, but it still remains one of the most debated step in PET/MRI image reconstruction (Y. Chen and An, 2017; Ladefoged et al., 2017). Inferring the photon absorption characteristics from MR images is particularly complicated because of the different physical principles that underlie the signal generation in the two modalities. Specifically, the MR signal depends on proton density and tissue relaxation times and it does not reflect electron density, which, on the other hand, is relevant for attenuation correction (Lundman et al., 2017). Hence, there is no direct correspondence between the MR signal and gamma radiation absorption at 511 keV. In particular, this is the case of bone tissue and air, whose AC values are at the lower and upper bound of the attenuation factor distribution. Those tissues are fundamental for calculating μmap but very complex to describe with standard MR sequences. Indeed, the cortical bone $T2^*$, i.e. the spin-spin relaxation in presence of field inhomogeneity, is so fast the tissue signal dephases before any conventional MR sequence collect data. However, if the sequence echo time is short enough, the bone signal has not completely dephased and thus detectable.

In the last ten years, several approaches have been proposed in literature to solve the MR-based attenuation correction problem. These can be categorized in two main groups: template/atlas-based and segmentation-based methods (Y. Chen and An, 2017).

The template/atlas-based methods rely on an atlas of predefined paired structural MR and CT images and on an algorithm that create a pseudo-CT image

starting from the patient's MR image. Those methods commonly derive a computational relationship between a group of observed CT and MR image pair using population data, which can be generalized for subsequent deployment in absence of CT image. Depending on how the pseudo-CT is computed, the atlas-based methods could subdivided into three subgroups: patch-based, voxel-based and machine learning-based approaches. The first two approaches are aimed at achieve a good alignment between the single subject structural image and the atlas MR, that was previously matched to the population CT, the pseudo-CT is then typically obtained by an averaging of all the atlas CT (Burgos et al., 2014; Catana et al., 2010). The machine learning-based approaches employ the atlas paired MR and CT images to derive a mathematical relationship between the two images using a set of features such as signal intensity, geometrical metrics, or heterogeneity extracted from the structural MR image and recombined to determine the pseudo-CT map. Although the high computational cost due to the learning step, this third methods class represents one of the most investigated and intriguing MR-AC technique in the last few year. Several machine learning methods including support vector machine, gaussian process regression, random forest have been proposed (Y. Chen and An, 2017; Shi et al., 2017; Mehranian, Arabi, and Zaidi, 2016), however the most promising seems to be convolutional network-based techniques such as those proposed by Gong and colleagues (Gong et al., 2017) and by Han and colleagues (Han, 2017).
The segmentation-based methods are direct MR imaging-based methods that derive the μmap exclusively from MR images, usually by segmenting the structural T1-weighted (T1w) images or images acquired with expressly dedicated sequences into multiple tissue classes. To build the subject specific pseudo-CT, each class is uniquely assigned to a constant mean linear attenuation coefficient according to literature values (Wagenknecht et al., 2013), an analogous to colour-by-numbers. This way a piecewise constant AC factor along the LOR is employed during the AC step (Y. Chen and An, 2017). Beside T1w images, the images that are commonly employed for this purpose are collected using the following sequences: two-point Dixon-Water-Fat (Dixon), (Martinez-Moller et al., 2009; Wollenweber et al., 2013), the ultrashort echo time (UTE) (Catana et al., 2010) and the 3-dimensional radial zero echo time (ZTE) (G. Delso, F. Wiesinger, et al., 2015; Sekine et al., 2016; Florian Wiesinger et al., 2016). The ability to identify different regions and the number of different classes (tissue content) largely depends on the MRI sequences used. Concerning Dixon images, a three tissue segmentation is

usually performed (i.e. air, fat and water) to compute the photon absorption map as bone, especially cortical bone with high density, seems to be undetectable on these images. On the opposite, UTE and ZTE sequences are more sensitive to high density tissues and thus allow for the imaging of the bone (Y. Chen and An, 2017; Keereman, Fierens, et al., 2010). This lead to more robust tissue segmentation and accurate pseudo-CT map. In particular, the dual-echo UTE is employed as it gives information of both bone and soft tissues; the first echo, the shortest one, is mainly used to imaging the bone, while the second, to collect data from all the other tissues. Images from the two echoes are then combined to produce a map that represents bone, soft tissues, fat and air (Muzic and DiFilippo, 2015). Relative to ultrashort echo-time (UTE), zero echo time (ZTE) imaging offers higher SNR and reduced image blurring for short-T2 imaging (G. Delso, F. Wiesinger, et al., 2015). However, as the sequence is inherently 3D, ZTE imaging is time consuming (Florian Wiesinger et al., 2016; Sekine et al., 2016). Images obtained with this technique are proton density weighted images. The pseudo-CT is computed by normalizing and segmenting the image according to specific predetermined signal intensity threshold (Sekine et al., 2016).

Atlas-based methods have shown to be little sensitive to image noise and artefact and thus highly accurate and robust, but concurrently time consuming and unable to account for subject's abnormal anatomy and/or unusual tissue density that significantly differ from the population atlas. In particular the last point is a critical aspect for machine learning approaches. On the opposite, segmentation based approaches are fast and can account for patient's variability better than atlas-based methods, however, as will be shown and discussed in the next chapter, they are influenced by image noise and artefacts such as the one produced by metal dental implants (Y. Chen and An, 2017) or by high magnetic field inhomogeneity (G. Delso, Carl, et al., 2014).

Concerning the two commercially available PET/MRI scanner, the attenuation correction step is realized in two different ways. The AC in GE Signa PET/MRI system is based on an atlas of MRI/CT pairs used to derive the approximate size and location of bones and air cavities, as reported in (Wollenweber et al., 2013). Two AC-methods are available in the Biograph mMR system, both based on segmentation of the MR image into tissue classes. The first, as described in (Martinez-Moller et al., 2009), exploits Dixon images, while the second makes use of UTE images and is implemented as proposed by Catana and colleagues (Catana et al., 2010).

A recent study (Ladefoged et al., 2017) compared the performances of 11

different clinically feasible AC methods that employed either atlas-based or segmentation-based approaches. What was found was that globally literature methods outperformed the vendor methods, in particular, the atlas-based method proposed by (Izquierdo-Garcia et al., 2014) was one of the best performing methods, as it minimized the number of outliers, standard deviation, and average global and local errors. The study concluded that the challenge of improving the accuracy of MR-based attenuation correction in adult brains with normal anatomy has been solved to an acceptable degree, with errors smaller than the quantification reproducibility in PET imaging (i.e. 5%). But it should be taken into account that the most part of clinical studies is performed on pathological tissues and thus robustness and reproducibility need to be assessed also in this case before considering the AC problem in PET/MRI being solved.

Finally, to obtain a complete μmap to be exploited for AC, it is necessary to consider another difference between the PET and MR imaging modalities. Indeed, as the field of view (FOV) of the PET camera is larger than the MRI scanner field of view, the MRI-derived attenuation map is typically incomplete, and that could potentially have an impact on the reconstructed data and bias the tracer kinetic quantification. The truncation effect becomes more evident if specific body regions, such as the torso, are scanned, because for example the arms of the patients in most cases exceed the field of view of the MRI camera and contrary to PET/CT standard acquisitions are posed beside the patient's body. Although outside the MR FOV they contribute to gamma rays attenuation anyway (Harald H. Quick, 2014). The same could be said for the lower part of the neck while acquiring the patient's brain. To overcome this problem, on the Biograph mMR scanner, a maximum likelihood activity and attenuation (MLAA) estimation algorithm was implemented (Nuyts et al., 2013; Berker and Y. Li, 2016). This allows to recover the missing part of the attenuation map from the PET emission data (Heußer et al., 2017; Catana, 2017).

Chapter 3

Framework for Simultaneous PET/MRI Study of Brain Connectivity

To perform analyses of brain connectivity with an hybrid PET/MRI scanner, it was necessary to define an optimal acquisition protocol for both MR and PET, as well as an ad hoc PET image reconstruction and analysis pipeline. The optimization process was carried out in order to obtain highly sensitive images for both modalities, remaining within a predominantly clinical environment such as the one in the Nuclear Medicine Department of Padova Hospital. Indeed, when my PhD work started, the Siemens Biograph mMR scanner at the Nuclear Medicine Department was mainly devoted to clinical studies, that did not required advanced MR imaging protocols and did not have specific technical requirements on the reconstructed PET data images, as only static analyses were performed.
Concerning PET, the goal of this framework was to obtain data suitable for a quantitative analysis which was not limited to a single static image description of the observed phenomena, but, conversely, that could enable us to fully model the kinetics of the tracer within the tissues, providing a quantification of the underpinning physiological and biological processes. For this reason, the image reconstruction pipeline had to be modified so that it could include a state-of-art attenuation correction step, and it could allow different sampling time grid (or time binning) of the dynamics, which turned to be particularly useful for identifying and quantifying specific characteristics of the PET signal.
The interest in describing the brain connectivity both in terms of statistical dependencies among regions activities (i.e. functional connectivity) and in terms of presence of anatomical links between pairs of brain regions, led to

the necessity of optimizing respectively functional magnetic resonance imaging (fMRI) blood oxygen-level dependent (BOLD) and diffusion tensor imaging (DTI) sequences. Particularly, to achieve the scanner best performance, it was indispensable to employ the recently introduced multi-band EPI parallel imaging techniques.
In what follows, a detailed description of the optimization process and obtained framework is reported.

3.1 Dynamic PET Data Reconstruction and Analysis

One of the main goal of this work was to quantify physiological and physiopathological processes, such as metabolism and blood flow, by means of mathematical kinetic modelling of PET signal (R. N. Gunn, S. R. Gunn, and Cunningham, 2001). To this aim, while scanning, the raw count data were collected in 3D list mode and images were reconstructed according to the type of analysis and features that would be extracted. Even if the experimental setting did not allow acquisition of arterial sampling, when the entire PET dynamic was available, the compartmental modelling with image derived input function was used for the kinetic analysis. This method has been preferred for two reasons: first, the radiotracers employed in our studies did not have reference regions, hence, compartmental modelling with reference region was not a viable approach to describe our kinetic; and second, from our data it was possible to extract a reliable image derived input function (IDIF), as the major vessels of the neck were included in the PET images thanks to the wide field of view of the PET camera in the PET/MRI system. As for every signal, the ability in describing the IDIF shape is tightly related to the PET signal sampling (Oppenheim, Willsky, and Nawab, 1997), therefore the PET signal reconstruction time grid has been selected so that it was suitable both for extracting the IDIF and for fitting the model. This choice was based not only on the possibilities offered by the modelling technique, but also on the used tracer, i.e. ^{18}F-Flutemetamol for the study reported in Chapter 4 and ^{18}F-Fluorodeoxyglucose (^{18}F-FDG) for the proof-of-concept study reported in Chapter 5.
This section describes three distinct problems that have to be addressed to obtain reliable quantification of PET data, and the proposed solution. In particular, first it is delineated a pipeline for off-line PET list mode preprocessing

and reconstruction, then is investigated how to define an PET time binning (i.e. time framing) which could be reasonable for extracting the IDIF, and finally a method for estimate a proxy of the cerebral blood flow from the dynamic PET data is introduced.

3.1.1 Off-line Preprocessing and Reconstruction Pipeline

PET data preprocessing and reconstruction was performed outside the scanner (off-line) using the Siemens e7-tool for Biograph mMR (version VB20P) software, which is a stand-alone version of the software pre-installed on the PET Reconstruction Server (PRS) of the Biograph mMR system. The use of this software offers more degrees of freedom in defining the processing pipeline than the PRS reconstruction, as it consists of a collection of command line scripts, one for each step. Therefore, it enabled us to choose the step of the process to be performed and which attenuation map to be employed, and to avoid the time-consuming PET reconstruction process being done on-line, with obvious positive implications on clinical trials. For these reasons, the goal was to delineate a fully automated pipeline that performs off-line preprocessing and reconstruction of the PET data acquired using the Biograph mMR scanner, making use of a state-of-art attenuation correction algorithm.
The e7-tool reconstruction pipeline consists in three main step: histogramming of list mode file, calculation of the extended μmap (via MLAA, as discussed in the previous chapter), and finally image reconstruction including data preprocessing and post-processing smoothing. In the first step, the list mode file is sorted in multiple emission sinograms, one for each time frame of the reconstructed dynamic PET, or one in the case of static PET image. In the second, if necessary, the maximum likelihood activity and attenuation estimation algorithm is employed to extend the MR-derived human attenuation map to the PET camera FOV. In the third, each single emission sinogram undergoes a preprocessing that includes attenuation correction, scatter and random correction, normalization, dead time correction and decay correction. Finally, the reconstruction algorithm is applied to corrected sinograms to obtain the dynamic PET data.
While organizing the reconstruction pipeline, we mainly focused on attenuation correction, since as discussed in the previous chapter is still one of the open issues in PET/MRI reconstruction. Neither the default parameters nor the algorithms used in the sinograms preprocessing and reconstruction have

been modified, except for parameters related to the attenuation correction and potentially to the time binning.

Attenuation correction: Since attenuation maps obtained from vendor Dixon and UTE sequences were known to be less accurate than μmap computed from other MR sequences, it has been decided to derive the single patient attenuation map from the structural T1-weighted MPRAGE image using the method proposed by (Izquierdo-Garcia et al., 2014), which, at the time, was one of the best performing method according to comparison study performed by Ladefoged an colleagues (Ladefoged et al., 2017). In particular, two are the main reasons that have been considered during the choice of this method. First, it has been shown that this is one of the two best performing in terms of average and standard deviation error in the cerebellum region, which is a brain region of utmost interest for PET studies as it is often used as reference for normalization purposes like in the first application of this framework reported in Chapter 4. Second, it was the only one that at the time had been performed and evaluated on brain tumours, which is the case of the second framework utilization and evaluation described in this work of thesis.
This method implement a template-based approach. It first corrects for bias field inhomogeneities and normalizes the T1w image using the normalization tool (Sled, Zijdenbos, and Evans, 1998) included in the FreeSurfer Software Suite (https://surfer.nmr.mgh.harvard.edu). Then, it employs the Statistical Parametric Mapping (SPM, http://www.fil.ion.ucl.ac.uk/spm/) version 8 (SPM8) to extract patient specific tissue probability maps from the individual's intensity normalized T1w MPRAGE image. These probability maps are subsequently exploited to robustly register the subject's T1w image to a template of CT co-aligned probability maps of 15 healthy adults. The averaged corresponding CT template is then back-warped to patient space, converted to linear attenuation coefficient at 511 keV, and blurred with a 4mm Gaussian filter (Izquierdo-Garcia et al., 2014). In the proposed pipeline, the attenuation map thus obtained is then merged with the attenuation map of the head-neck coil and scanner bed, and employed in the attenuation correction step of the preprocessing. To note that, as the MR-derived μmap is already spatially smoothed, the regularization operation within the attenuation correction step in off-line pipeline is not performed. This step is in fact intended for the use of attenuation maps obtained with vendor sequences, for which generally is not carried out a spatial smoothing. An example of the

patient's UTE- and MPRAGE-derived photon attenuation μmap is shown in the first row of Figure 3.1.

Extended μmap: The FOV truncation potentially bias the tracer kinetic quantification and typically it is necessary to recover the attenuation map of the truncated part both in body and head studies. Nevertheless, we avoided inserting it into our reconstruction pipeline because of the wide field of view of the MR structural images, which comprised all the patient's neck and shoulders tissues included in the PET images and that contributed to the signal attenuation.

The proposed pipeline was written in Matlab (The MathWorks, Inc.). The script is essentially a wrapper of the μmap computation algorithm call and of each single step e7-tool functions system calls. It runs on two different operating systems (OS) as the e7-tool is only compiled for Windows OS but the Izquierdo and colleagues methods requires the usage of FreeSurfer software that is specifically implemented for Linux OS. It works as follows: it receives as input the raw PET data and the MPRAGE image of the patients exported from the scanner and provides as output the required dynamic PET data according to the selected time grid and voxel size. In particular, the pipeline consists of the subsequent steps:

1. the PET raw data (list mode and normalization file) are organized according to e7-tool requirement
2. the attenuation map is computed using the method proposed by (Izquierdo-Garcia et al., 2014)
3. the complete μmap is calculated using the vendor provided acquisition system μmap and the subject specific attenuation map
4. the list mode is time binned (histogramming step)
5. the sinogram is preprocessed employing the custom human μmap and the daily acquired normalization files, and the PET image reconstructed exploiting the iterative 3D ordinary Poisson ordered subset expectation maximization (OP-OSEM) algorithm (Popescu, Matej, and Lewitt, 2004). Image matrix size 256x256x127, voxel size 2.8x2.8x2 mm^3.
6. no additional spatial smoothing is performed to avoid increasing the partial volume effect .

To note that a considerable number algorithm are available for reconstruction, which differ mainly on the hypothesis of reconstruction model that represents the relationship between the measured PET sinogram and the actual image (i.e. the actual position of observed annihilation events). The existing methodologies can be divided essentially into two types: analytical algorithms where the model is deterministic and can be inverted to find the image, and iterative algorithms where the model is stochastic (i.e. it includes a statistical description of the distribution of the signal noise, typically a Poisson or log-normal distribution) and cannot be analytically inverted, and the image needs to be estimated with iterative approaches (Bailey et al., 2005; Henkin et al., 2006).
Since the selection of the optimal reconstruction algorithm and the fine tuning of its parameters was beyond the scope of this work of thesis, it was decided to employ the e7-tool implementation of the iterative algorithm 3D OP-OSEM using the software default and commonly used parameters (i.e. 3 iterations and 21 subsets). OSEM (Hudson and Larkin, 1994) is indeed the most widely used methodology in the literature (Henkin et al., 2006). Moreover, it models the relationship between the detected annihilation events and the image in a realistic and complete way (Henkin et al., 2006; Zaidi, 2006), and has proved to be particularly robust to poor count statistic (i.e. low dose injection or regions with limited tracer uptake) and not affected by steak artefacts (Van Velden et al., 2008). Although aware of the presence of different optimization approaches for the estimators used for the OSEM model (Reilhac et al., 2008; Qi and Leahy, 2006; Rapisarda et al., 2010), as an agreement on which of these is the best has not yet been reached, in order to obtain results comparable to the literature, the 3D OP-OSEM implementation was chosen to remain consistent with what is done by the scanner PET Reconstruction Server.

Off-line and on-line SSR PET Reconstruction Experimental Comparison

In order to verify that the reconstruction performed with the proposed pipeline was consistent with the scanner PRS reconstruction and to quantify the impact of the use of the MPRAGE-derived μmap on our data, the static images obtained with different attenuation maps and with different reconstruction systems for a single oncological patient imaged with ^{18}F-FDG were compared. The available data for that comparison were: the 70min ^{18}F-FDG PET list mode acquisition (administered dose 261 MBq), the normalization files, the 3D T1-weigthed MPRAGE (TR/TE 2400/3.2 ms, voxel dimension

of 1x1x1mm^3, FOV 256 mm, 160 slices) and the 3D T2-weighted Fluid Attenuated Inversion Recovery (FLAIR) (TR/TE 5000/395 ms, voxel dimension of 1x1x1mm3, FOV 250 mm, 160 slices). As e7-tool requires input in list mode form, it was not possible to extend the analysis to other datasets collected in the Nuclear Medicine Department of Padova Hospital because they not acquired in this specific format.
The e7-tool reconstruction was performed with default parameters, the selected voxel size was the same of the scanner reconstruction (matrix size 344x344x127) and a post-processing smoothing with a 2mm FWHM kernel was applied to be in line with on-line reconstruction.
To highlight the differences between the reconstruction results, we also computed the percentage difference between the achieved static images and analysed those differences both at whole brain level and at the level of single tissue (i.e. as average of differences in white matter, grey matter and cerebrospinal fluid), including the tumour tissue. At voxel level the percentage differences were computed as follow:

$$Scanner_{UTE} - e7_{UTE} = \frac{Scanner_{UTE} - e7_{UTE}}{Scanner_{UTE}} * 100$$

$$Scanner_{UTE} - e7_{BOSTON} = \frac{Scanner_{UTE} - e7_{BOSTON}}{Scanner_{UTE}} * 100$$

$$e7_{UTE} - e7_{BOSTON} = \frac{e7_{UTE} - e7_{BOSTON}}{e7_{UTE}} * 100$$

where $Scanner_{UTE}$, $e7_{UTE}$, $e7_{BOSTON}$ are respectively the static reconstruction obtained on-line using the UTE-derived μmap, the e7-tool static reconstruction obtained using the UTE-derived μmap, and the e7-tool static reconstruction obtained using the MPRAGE-derived μmap.
In order to carry out these analyses, the patient's FLAIR image was employed by an expert nuclear physician to delineate the tumour tissue and the MPRAGE was automatically skull-stripped and segmented in white matter, grey matter and cerebrospinal fluid using the Advanced Normalization Tool (ANTs) software (Avants, Tustison, Song, et al., 2011; Avants, Tustison, Stauffer, et al., 2014). Both segmentation were then moved into the PET space using the affine transform estimated by the scanner. Finally, for each tissue of interest the mean and standard deviation of the percentage change were computed.
The employed μmaps and the resulted static images are reported in Figure

3.1. The MPRAGE-derived μmap was only utilized in the off-line reconstruction, because it was not possible to import that map into the scanner. As can be seen, there is a significant difference between the two μmaps, that is more and more evident in the frontal and paranasal sinus area and results in geometrical distortion in the static images (highlighted in the images with red circles). This pattern of differences in the μmaps should be attributed to the type of MR sequence that was exploited to compute the maps. Indeed, UTE-derived maps suffers from the geometric distortion and signal loss that are characteristics of echo-planar images and that are tightly to the MR image readout and to static magnetic field inhomogeneity induced by magnetic susceptibility variations (Haacke et al., 1999).
The maps of the percentage differences between the three reconstruction are displayed in Figure 3.2, and the tissue mean percentage differences are reported in Table 3.1. From the maps in Figure 3.2, it could be observed that there was no significant spatial pattern of differences between the $Scanner_{UTE}$ and the $e7_{UTE}$ reconstruction, conversely, a spatial pattern of differences were found when the different μmaps were used and those differences were mainly confined in the UTE geometric distorted area (depicted in yellow and light blue shades in the figure).

As reported in Table 3.1, percentage differences were negligible both at whole brain level and at tissue level when we compared the $Scanner_{UTE}$ and the $e7_{UTE}$ reconstruction, but not negligible differences were found when we compared the results obtained with the two different μmap. As expected, the higher differences were found in the grey matter and the CSF.
To conclude, the consistency between e7-tool proposed pipeline and PRS reconstruction has been verified. This means that the proposed pipeline for off-line PET image reconstruction is sufficiently robust. In addition the differences in white and grey matter between the static images reconstructed

Tissue	Scanner$_{UTE}$ - e7$_{UTE}$	Scanner$_{UTE}$ - e7$_{BOSTON}$	e7$_{UTE}$ - e7$_{BOSTON}$
WB	-1.59±2.88	-9.85±29.16	-7.76±21.27
GM	-1.45±1.02	-8.91±9.73	-7.32±8.43
WM	-1.44±0.73	-7.18±7.45	-5.64±6.68
CSF	-1.75±3.41	-8.44±34.18	-5.95±24.67
Tumour	-1.43±0.34	-4.33±3.02	-2.86±2.97

Table 3.1: Summary of the comparison of results obtained with the three test AC methods: $Scanner_{UTE}$, e7$_{UTE}$ and e7$_{BOSTON}$. For each couple the mean and standard deviation of the percentage difference is reported.

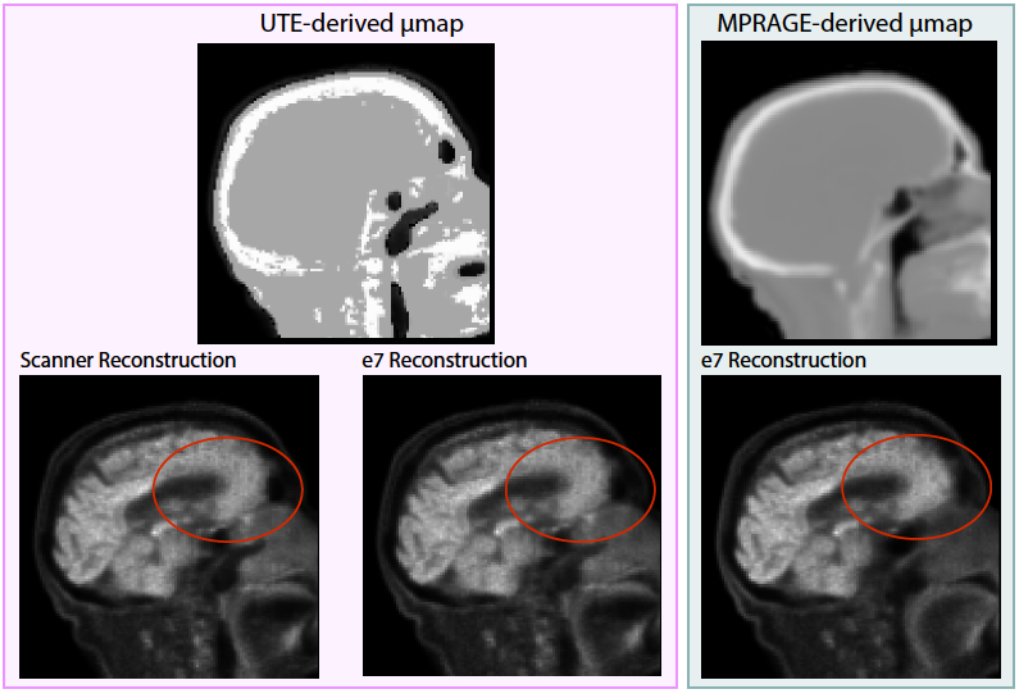

Figure 3.1: Attenuation correction maps and corresponding ^{18}F-FDG static reconstruction. Top row: left hand side, UTE-derived attenuation map (μmap); right hand side, MPRAGE-derived attenuation map, computed using the algorithm proposed in (Izquierdo-Garcia et al., 2014). Bottom row: left panel, scanner (left) and e7-tool (right) UTE-derived μmap based reconstruction of ^{18}F-FDG static PET; right panel, e7-tool (right) MPRAGE-derived μmap based reconstruction of ^{18}F-FDG static PET. The red ellipse highlights the areas in the frontal pole near the frontal and paranasal sinus where the impact of the different μmap is more evident.

using the two μmaps were in line with the findings of the study reported in (Ladefoged et al., 2017). At the time, no data were available in literature for a results comparison within the tumour tissue. Indeed, although it has been shown that μmaps obtained with the Izquierdo and colleagues method are very robust also in the presence of a tumour, particularly near the cranium, it has not yet been evaluated how the presence of tumour tissue can act in terms of attenuation of the PET signal. Further analyses are certainly necessary to evaluate how a μmap devoid of the contribution in tumour tissue attenuation can impact on attenuation correction step, although the reported results tumour region seems to be the less affected region.

In light of this results, the following considerations can be made: first, it is fundamental that within the same study the reconstruction of the PET images is carried out using the same processing pipeline, as differences in processing could potentially bias the results. Second, as the differences in reconstruction have shown a clear spatial pattern, which was in agreement with the pattern

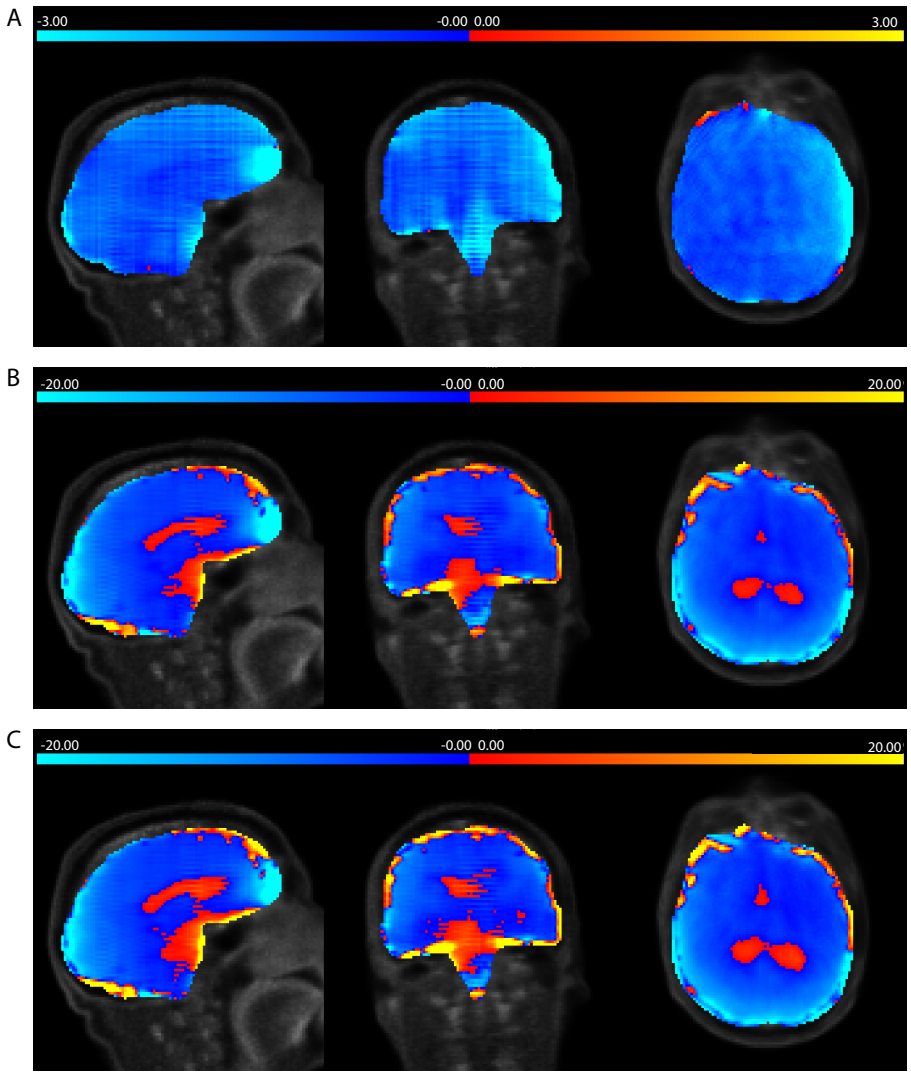

Figure 3.2: Maps of percentage difference between the ^{18}F-FDG static reconstruction. The panels exhibit the $Scanner_{UTE} - e7_{UTE}$ percentage difference (A), the $Scanner_{UTE} - e7_{BOSTON}$ percentage difference (B), and the $e7_{UTE} - e7_{BOSTON}$ percentage difference (C). To note that the colour scales of the second two panels cover a wider range of values.

observed by Ladefoged and colleagues (Ladefoged et al., 2017), when a comparison with literature is performed, it is necessary to take into account that some differences especially if located in frontal regions may be partially explained by the type of reconstruction carried out.

3.1.2 Optimal PET Time Binning for Image Derived Input Function

One of the problems that had to be faced during the development of the framework for the acquisition and analysis of simultaneous PET/MRI data

was how to sample the PET signal so that it was suitable for using in a compartment modelling. Indeed, to employ this mathematical approach to dynamic PET data, it is necessary to know precisely how the concentration of the tracer varies dynamically within the arteries, as this is the input signal (arterial input function, AIF) to the model, and to have reliable time activity curves (i.e. signals with good signal to noise ratio) (R. N. Gunn, S. R. Gunn, and Cunningham, 2001).

Typically in research studies, the AIF is obtained by means of an invasive arterial sampling, which is considered the gold standard technique (Zaidi, 2006), however in the PET/MRI clinical setting of the Nuclear Medicine Department of Padova Hospital a MR-compatible device capable of acquiring this type of data is not available. For this reason and due to the fact that the PET/MRI system allows to have a larger field of view, it was decided to use an image derived input function (IDIF) as input for the compartmental modelling (K. Chen et al., 1998; Mourik et al., 2009). Indeed, large arterial blood pools (i.e. common carotids) are included in FOV. Moreover, according to Zanotti-Fregonara and colleagues (Zanotti-Fregonara et al., 2011) signal extracted from the neck large vessel are subjected to less partial volume effect than signal obtained from other small brain vessels such as the internal carotid siphons.

As the image derived input function is extracted from the reconstructed dynamic PET data, the ability to discriminate and characterize the IDIF is obviously dependent on the time binning employed during the reconstruction (X. Li and K. Chen, 2000).

To evaluate what was the appropriate time binning for the IDIF extraction several time grids were tested. The choice of the time grids to be tested was performed according to the frame-sampling intervals proposed by Haggstrom and colleagues in their simulation study (Haggstrom et al., 2015) and by Raylman and colleagues (Raylman, Caraher, and Hutchins, 1993). The performances of a subset of these two sampling schemes were assessed. In addition the selection of the time grid was performed having as reference the arterial sampling grid commonly used in literature for that specific analysed tracer. Finally, it has been selected the time framing that allowed to better identify the IDIF time to peak and peak amplitude, that are the two most important parameters for the fit of the arterial input to the model. We mainly focused on the temporal description of the signal rather than the spatial one since in PET/MRI scanners large vessels could be localized using the time-of-flight (TOF) MR angiography as suggested by Fung and Carson (Fung

and Richard E. Carson, 2013) and subsequently developed by Sari and colleagues (Sari et al., 2017). TOF angiography is an MRI techniques that allows to visualize the vessels, without the need to administer contrast agent, and is based on the principle of flow-related enhancement of spins (Haacke et al., 1999). To note that if the TOF angiography is not available, as in the study reported in the Chapter 4, a more dense signal sampling becomes also useful for the spatial location of those vessels. This increased disentangle ability was quantified by means of contrast to noise ratio (CNR), which is computed as follows

$$CNR = \frac{m_{CC} - m_{BG}}{\sigma_{BG}} \tag{3.1}$$

where m_{CC}, m_{BG} and σ_{BG} are respectively the average of the counts in the common carotids and in the background, and the standard deviation of the background's counts, computed at the time frame corresponding to the specific reconstruction IDIF peak. This approach was borrowed from previously PET activation studies, where to be detected the stimulated activity signal needs to overcome the background noise variance (Richard E. Carson, Daube-Witherspoon, and Herscovitch, 1998).

An example of the image derived input function extracted from the same pool of voxels and reconstructed with four different time grids, is reported in Figure 3.3. From the image, it is clear that the last sampling (i.e. the one with the more dense sampling) allowed a better description of tracer dynamics within the vessels with respect to the others.

For each of the two tracers used in the two proof-of-concept studies reported in this work, the obtained results as well as the selected time binning are reported and discussed in the corresponding chapter.

It is useful to highlight at this point how this type of binning selection is suboptimal mainly for two reasons. The first is that it is not possible to directly validate the choice, because no arterial sample is available. As reported in the two following chapters, an attempt to justify the performed choice was made by evaluating the reproducibility of the IDIF curves obtained for the entire dataset, or alternatively by checking whether the estimates of the parameters obtained form the compartment modelling were or not in line with the literature results, as it is known from studies conducted by Cheng and colleagues (Cheng and Yetik, 2011) and by Haggstrom and colleagues (Haggstrom et al., 2015) that blood input function error propagates to the estimate of the model kinetic parameters and significantly alter those estimates. The second potential limitation is that as the time binning has a non negligible impact on the signal noise distribution due to the reduced frame count content,

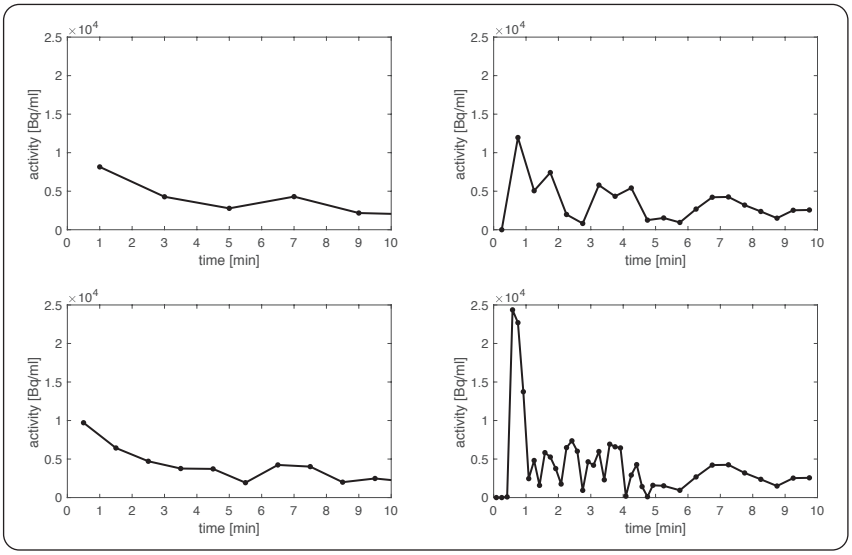

Figure 3.3: Example of image derived input function. The four panels display the same 10-minutes PET dynamic sampled with different time framing: top-left, 2-minutes sampling step ; bottom-left, 1-minutes sampling step; top-right, .5-minutes sampling step; bottom-right, framing intervals of 30x10s and 10x30s.

this could possibly interfere with the reconstruction step as it employs an estimation maximization approach that is tightly linked with the hypotheses of noise distribution (Barrett, Wilson, and Tsui, 1994). Thus, further studies designed with a proper factorial analysis could be performed with the aim of quantifying the interaction effect between the time binning and the reconstruction parameters, and potentially confirm that the 3D OP-OSEM reconstruction algorithm and its main parameters are sufficient to robustly solve the reconstruction inverse problem and converge to a global minimum of the cost function.

3.1.3 Proxy of Cerebral Blood Flow from Dynamic PET Data

In the last few years several studies have investigated the relationship between the cerebral blood flow (CBF) and the connectivity both in healthy subjects (Qiu et al., 2017; Liang et al., 2013) and in pathological condition such as schizophrenia (J. Zhu et al., 2017), mild traumatic injury (Sours et al., 2015), Alzheimer's disease (Sierra-Marcos, 2017) and dementia (Lou et al., 2016). Concerning functional connectivity, in healthy subjects a tight relationship has been found between the pattern of CBF and the topology of resting state networks (RSNs) like default mode network and other executive

control network (Liang et al., 2013). On the other hand, from a clinical perspective, alterations in CBF have been linked to resting state network disruption, in particular, areas with reduced perfusion appear to have a decreased functional connectivity with the rest of the brain (Lou et al., 2016). Despite these early studies the association between hypoperfusion, functional network alteration and cognition is still unclear. However, understanding the CBF changes in the context of changes in the network connectivity may provide further insights into the pathophysiology and may extend the understanding of the mechanism of the disease. For these reasons, part of this work of thesis was focused on providing a proxy of the cerebral blood flow from dynamic PET data.

The compartmental modelling describes the kinetic of the radiotracer displacement within the tissues and according to the specificity of the tracer how it is metabolised or it binds to specific ligands. An example of the structure of a compartmental model is depicted in Figure 3.4. The rate at which the tracer from plasma or blood compartment crosses the blood-brain barrier (BBB) to enter the first brain compartment, namely the influx rate constant (K_1,($ml/cm^3/min$)), is tightly related to CBF and can be used as a proxy of it. Indeed, in a capillary model, this rate constant for blood-brain barrier transport is related to perfusion according to the following equation:

$$K_1 = FE \tag{3.2}$$

where E is the unidirectional extraction fraction from blood into brain during the tracer's first pass through the capillary bed, and F denotes the blood flow (Natalie Nelissen et al., 2008). Using the Renkin-Crone model (Renkin, 1959; Crone, 1963), the unidirectional extraction fraction can be expressed as:

$$E = 1 - e^{-\frac{PS}{F}} \tag{3.3}$$

where P is the blood brain barrier permeability (cm/min) and S is the the capillary surface area per gram of tissue (cm^2/gr). For highly permeable tracers, the product PS is much greater than the cerebral blood flow F, so the exponential term is small, and the unidirectional extraction fraction is close to 1. In this case, the influx rate constant is approximately equal to flow (Richard E Carson, 2003). From the previous observation, it is clear that depends on the brain blood barrier permeability and thus is strictly dependent on the dynamic PET study tracer.

In the present work the employed tracer was the ^{18}F-Flutemetamol, which is

a tracer that binds to the aggregated Aβ peptides in neuritic amyloid plaques and is generally exploited in clinical studies for the diagnosis of Alzheimer's disease (AD) and other types of dementia. ^{18}F-Flutemetamol is an analogue of ^{11}C-Pittsburgh Compound B (^{11}C-PiB), with which it has been shown to have a good agreement both in terms of static and dynamics analyses of the PET signal (N. Nelissen et al., 2009; Hatashita et al., 2014; Mountz et al., 2015). In particular, as reported by Heurling and colleagues (Heurling et al., 2015) and by Chen and colleagues (Y. J. Chen et al., 2015) compartmental modelling estimates of the K_1 obtained with the two tracers are highly correlated.
Recently, a number of studies has been performed in order to prove that the early PET dynamic of ^{11}C-PiB and its fluorinate derives could be used as a robust proxy of cerebral blood flow. In particular, in a early study Bloomquist and colleagues reported that changes in the influx rate constant of ^{11}C-PiB closely followed changes in CBF, caused by alteration of Pa_{CO2} on studies performed in rhesus monkeys (Blomquist et al., 2008). Subsequently, several studies investigated in humans the relationship between the early frames standard uptake value (SUV) or the regional relative radioligand delivery of ^{11}C-PiB and the regional cerebral glucose metabolism, which is considered a surrogate of CBF (Meyer et al., 2011; Farid et al., 2015; Forsberg et al., 2012). More recently, Chen and colleagues (Y. J. Chen et al., 2015) quantitatively investigated whether or not the influx rate constant could be a robust surrogate index of the CBF through a full quantitative evaluation of ^{15}O-water and ^{11}C-PiB delivery parameters (i.e. K_1 and R_1) performed on a cohort of AD and MCI patients as well as healthy volunteers. What was found is a significant correlation between the parameters in analysis that is independent on the pathological condition, in agreement with the studied performed on BBB permeability conducted by Gjedde and colleagues (Gjedde et al., 2013), where no significant differences were found in ermeability between healty controld and AD patients. All these evidences support the use of ^{11}C-PiB K_1 and R_1 as reliable proxy of cerebral blood flow. In addition, studies on the relationship between the early frames SUV and the regional cerebral metabolism have also been conducted using fluorinate analogues of ^{11}C-PiB with similar results (Hsiao et al., 2012; Elena Rodriguez-Vieitez et al., 2017). For these reasons it was decided to employ the K_1 estimated through the compartmental modelling of the ^{18}F-Flutemetamol as a possible proxy of CBF.
Despite the compartmental model that best describes the ^{18}F-Flutemetamol tracer dynamics, i.e. the two reversible compartments model (2TC), has been known for several years (N. Nelissen et al., 2009; Heurling et al., 2015), it was

not possible to implement it on the dataset acquired at the Nuclear Medicine Department of the Padova Hospital. Indeed, due to the long time the radiotracer takes to reach the steady state (90 min, (Heurling et al., 2015), a full list mode acquisition of the after tracer injection entire dynamic was incompatible with the clinical timing. Hence, the data collection was divided in two distinct 20min lasting time windows: a first during the fast evolution of the PET signal immediately preceding and after the tracer intravenous injection, and a second acquired during the system steady state.
For this reason, to estimate the influx ratio constant, what was done was evaluating the feasibility of the use of a simplified compartmental model for robustly describing the first few minutes of the *early-phase* dynamic. In this framework it was hypothesised that, within the first minutes after the injection, it was possible to simplify the 2TC compartment model with a model with only one irreversible compartment (1TC), assuming in this way that exchanges with the second compartment and the venous efflux have not yet had place, or if it is so, that their effect on the dynamics is negligible. The reliability of this hypothesis was tested on a ^{11}C-PiB dataset, as will be discuss later in this chapter. The structure of the two models is depicted in Figure 3.4.

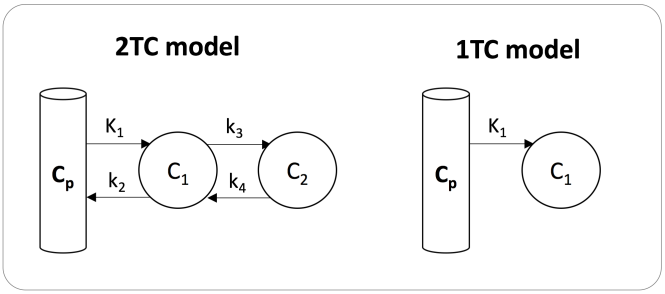

Figure 3.4: Compartmental model structures: on the left side the complete two reversible compartments model (2TC), on the right side the simplified one irreversible compartment model (1TC). C_P, arterial plasma tracer concentration; C_1, first compartment tracer concentration; C_2, second compartment tracer concentration; K_1 ($ml/cm^3/min$) and k_2 ($1/min$), tracer transport from plasma to first compartment and back, respectively; k_3 ($1/min$) and k_4 ($1/min$), tracer transport from first to second compartment and back, respectively.

As the PET signal was particularly noisy, mainly due to the low dosage employed, it was decided to implement 1TC model with two different measurement equations that would allow us to include or not a parametrization of the fraction of blood volume in the model itself. In equations 3.4 and in 3.5 the equation of the model that includes the blood volume fraction parameter, and the equation of the model that does not include it, are respectively

reported.

$$\begin{cases} \frac{dC_1(t)}{dt} = K_1 C_P(t) & C_1(0) = 0 \\ C_T(t) = C_b(t)V_b + C_1(t)(1 - V_b) \end{cases} \tag{3.4}$$

$$\begin{cases} \frac{dC_1(t)}{dt} = K_1 C_P(t) & C_1(0) = 0 \\ C_T(t) = C_1(t) \end{cases} \tag{3.5}$$

$C_1(t)$, is the tracer's concentration at time t in the compartment 1, $C_P(t)$ is the tracer's concentration in the arterial plasma, $C_T(t)$ is the total tracer concentration in the tissue, K_1 ($ml/cm^3/min$) is the influx rate constant and V_b is the fraction of blood volume. For each patient, the model was fitted at ROI level within a time window ranging from 0 minutes to the time at which the average grey matter time activity curve reaches the maximum (less than 3 minutes after the tracer injection, in agreement with what has been suggested in (E. Rodriguez-Vieitez et al., 2016)), using a linear least square approach without weighting the data.
The model that best fits the data was selected between the models described by equations 3.4 and 3.5 according to the Akaike information criterion (Akaike, 1974).
As for technical reasons the experimental setting did not allow us to collect arterial blood samples, the image derived input function was employed as arterial input for the model. The individual arterial input function was derived directly from the PET images of each subject by manually drawing a region of interest (ROI) in the left and right internal carotids. Since the model hypothesis is that the arterial input is not affected by noise, the extracted dynamic has been fitted using the tree-exponential model as proposed by (Feng, Huang, and X. Wang, 1993). The time to peak and peak amplitude were fixed in order to reduce the number of model's parameters that would have been estimated. An example of IDIF samples and fit is represented in Figure 3.5.

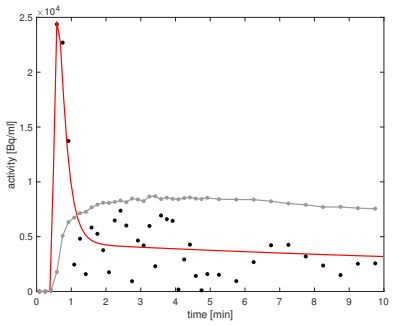

Figure 3.5: Example of image derived input function and tissue time activity obtained for a single patient. Black dots, image derived samples; red line, IDIF 3-exp model prediction; grey line, cortical grey matter average time activity curve.

Almost all tracers used in brain imaging produce variable amounts of radiometabolites, and this is also the case of ^{18}F-Flutemetamol, as reported in (N. Nelissen et al., 2009; Gjedde et al., 2013; Heurling et al., 2015). It is well-known that failure to correct for metabolites in the plasma curve might lead to 'quantitative' results that have no meaning (Lammertsma, 2002). One important limitation of IDIF is that it cannot distinguish the parent compound from its radioactive metabolites and the plasma radioactivity to that of whole blood (Zanotti-Fregonara et al., 2011). For this reason, the arterial sampling is required for determining the percentage of radioactive parent compound and metabolites. Once the percentage of metabolites is quantified, it is possible to correct the IDIF for this confound. Nevertheless, since the ^{18}F-Flutemetamol is a derivative of ^{11}C-PiB, whose metabolites behaviour is well described by Price and colleagues (Price et al., 2005) and by Gjedde an colleagues (Gjedde et al., 2013), and the time window where the model was fitted is confined within the first few minutes (less than 3 minutes), we assumed that the presence of metabolites could be considered negligible. This choice is mainly supported by the reports of Edison and colleagues (Edison, D. J. Brooks, et al., 2009) where the calibrated arterial input functions generated for the whole blood activity concentration, the total plasma activity concentration and the parent ^{11}C-PiB plasma activity concentration were compared. From the plot depicted in that work it is clear that within the first 3 minutes the impact of the metabolites on the parent plasma fraction is nearly undetectable. Moreover, we assumed that $C_b(t)$ was equal to $C_P(t)$, i.e. the tracer uptake by the red-blood cells is negligible. So the fitted IDIF was employed as noise-free input of the 1TC model instead of the unavailable metabolites-corrected plasma input function.

Albeit ^{18}F-Flutemetamol full dynamics were not available for this study, we

tested the reliability and aptness of our choices on a dataset of healthy controls imaged using ^{11}C-PiB. The dataset is properly described in (Mikhno et al., 2008). In brief, it consist in 12 healthy controls (age 71.5 $\pm$ 8.4, 6 female). PET emission data were collected for 85min after intravenous injection of 426 MBq ($\pm$ 151) of ^{11}C-PiB and the dynamic data were reconstructed into 18 frames of increasing duration (3x20s, 3x1min, 3x2min, 2x5min, and 7x10min). In addition, arterial blood samples were acquired in order to assess the concentration the radioligand over time and the fraction of unchanged radioligand in plasma (the Plasma Parent fraction or PPf) were measured with high-performance liquid chromatography (HPLC). Radiometabolite correction of AIF was performed as suggested in (Tonietto, Rizzo, Veronese, Fujita, et al., 2016).

We have first evaluated whether the proposed model reduction gave comparable results with respect to the full compartmental model and next quantify the effect of the hypothesis of metabolites negligibility within the first 3 minutes emission dynamic. The well known 2TC-4k (2-tissue 4-parameter) model (Price et al., 2005), which has the same structure of the model depicted in left-hand side of Figure 3.4 was employed to fit the data. Our hypothesis was that limiting the time interval where the model was fitted it was reliable to use a simplified compartmental model. To quantify how this assumption impact on the model estimates, for each patients we estimate at ROI level the kinetic parameters using both the complete and simplified models. The comparison was performed using the results obtained with the full dynamic (i.e. 0-85min) as reference. Beside the full dynamic three different fitting interval were evaluated: 0-15min, 0-5min and 0-3min. To fit the data of the last two time windows the compartmental model was reduced to the 1TC-2k (1-tissue 2-parameter) model as it was found that the data were not able to support the full model and the estimator became insensitive to the presence of the two additional fluxes included in the 2TC-4k model. Radiometabolite corrected AIF was exploited as input function and curve fitting was performed using a weighted non-linear least-square estimator. Weights were chosen optimally as:

$$w(t_i) = \frac{\Delta t_i}{C_{ROI}(t_i)} \tag{3.6}$$

where t_i is the time instant, Δt_i is the length of the scanning interval and $C_{ROI}(t_i)$ is the ROI average time activity at time t_i (as suggested in (E. Carson, Cobelli, and Finkelstein, 1983)).

In order to assess the impact of metabolites on K_1, concerning the 0-3min time window, we also estimate the 1TC-2k model parameters using as input

function the uncorrected arterial curve.
Four regions of interest were considered: the bilateral cingulate cortex, the hippocampi, the bilateral prefrontal cortex and bilateral parahippocampal gyri. Results are reported in terms of parameters percentage differences, computed as follows:

$$\Delta\% = \frac{p_{Mod} - p_{Ref}}{p_{Ref}} * 100 \tag{3.7}$$

where p_{Mod} and p_{Ref} stand respectively for estimates of the single model parameter obtained using the specific time interval and model in analysis and the 2TC-4k model on the full dynamic. In Table 3.2 are presented the results achieved for a single subject that was considered representative of the entire dataset. From the table it is evident that when the 0-15min interval was considered, the 2TC-4k model starts to show some difficulties in following the ROI activity curves, in particular, the fit of k_4 is not supported by the data for the majority of the ROIs. Indeed, although the model prediction is good and the residues accomplish the hypothesis of the noise distribution, the estimates of k_4 hit the lower bound (i.e. zero). The 1TC-2k model is adequate for the fit of the ROI time activity curves restricted to the interval 0-5min, although at the cost of a decrease in estimates precision. Indeed, a modest increase of the estimates coefficient of variation (CV) in this case is observed. In particular, the obtained estimates are reliable in terms of CV and comparable with the results of full dynamic, with changes in K_1 lower than 10%. If the fitting time windows is further reduced, i.e. within the 0-3min interval, the 1TC-2k model is not supported by the data. In this case the model estimator becomes insensible to the presence of the k_2 parameter. Hence, the 1TC-1k (1-tissue 1-parameter) seems to be the most proper model to describe the ^{11}C-PiB activity curves within the interval 0-3min. Moreover, K_1 estimates percentage difference are lower than 10%, that is obtained results are comparable with what is assessed using the entire dynamic.
Regarding the use of uncorrected for metabolites arterial input function, as expected, no significant differences were found. Parameter estimates and CVs are comparable with estimates and CVs gathered with corrected AIF (with $\Delta\%$ lower than 12%).
To summarise, the model structure (i.e. 1TC-1k) and the metabolites negligibility within the 0-3min observation window proved to be reliable for the ^{11}C-PiB tracer with estimates that are comparable with the results assessed using the full dynamic.

ROI	Par	Fitting time interval								
		0-85min	**0-15**min		**0-5**min		**0-3**min		**0-3**min†	
		Estim	Estim	Δ%	Estim	Δ%	Estim	Δ%	Estim	Δ%
cin	K_1	0.160 (5)	0.169 (15)	5	0.164 (23)	2	0.149 (26)	7	0.143 (26)	10
	V_b	0.079 (15)	0.074 (32)	7	0.076 (39)	4	0.079 (54)	0	0.081 (52)	2
	k_2	0.144 (7)	0.166 (39)	15	0.146 (71)	2	— (–)		— (–)	–
	k_3	0.011 (26)	0.021 (175)	95						
	k_4	0.019 (27)	— (–)	–						
hip	K_1	0.119 (4)	0.130 (34)	10	0.131 (20)	10	0.113 (20)	5	0.109 (20)	9
	V_b	0.074 (12)	0.067 (36)	9	0.066 (31)	11	0.073 (34)	2	0.074 (33)	0
	k_2	0.102 (8)	0.152 (212)	49	0.136 (64)	33	— (–)		— (–)	–
	k_3	0.009 (38)	0.088 (1001)	906						
	k_4	0.021 (36)	0.134 (985)	527						
pfc	K_1	0.129 (4)	0.136 (11)	5	0.137 (17)	6	0.117 (16)	9	0.113 (16)	12
	V_b	0.063 (12)	0.059 (24)	7	0.058 (31)	8	0.065 (32)	3	0.066 (30)	5
	k_2	0.137 (5)	0.158 (30)	16	0.158 (47)	15	— (–)		— (–)	–
	k_3	0.005 (32)	0.017 (169)	224						
	k_4	0.013 (45)	— (–)	–						
pip	K_1	0.127 (4)	0.132 (13)	4	0.126 (20)	0	0.117 (24)	8	0.112 (24)	11
	V_b	0.066 (13)	0.063 (26)	5	0.066 (31)	1	0.068 (45)	3	0.070 (43)	6
	k_2	0.104 (7)	0.119 (45)	15	0.094 (90)	9	— (–)		— (–)	–
	k_3	0.009 (35)	0.021 (234)	121						
	k_4	0.026 (29)	— (–)	–						

Table 3.2: Summary of the ^{11}C-PiB compartmental modelling results obtained in a representative subject fitting the dynamic PET signal at ROI level on different time interval. Four ROIs were considered, namely **cin**, **hip**, **pfc**, **pip** that refer respectively to bilateral cingulate cortex, hippocampi, bilateral prefrontal cortex and bilateral parahippocampal gyri. **Par** are the model parameters that has been estimated for each ROI. The 2TC (4k) model was applied to fit the data of the **0-85**min and **0-15**min interval, and the 1TC (2k) model to fit the remaining intervals. The metabolites corrected arterial input function (AIF) was used as model input for the first four intervals. † marks the interval where uncorrected AIF is exploited. Estim refers to model parameter estimates with coefficient of variance in parentheses. Δ% is the percentage difference between the parameter estimates obtained respectively fitting the entire curve and the curve restricted to the considered interval. — (–) is reported when data does not support the model and the estimator becomes insensitive to the parameter.

Concerning the use of the early PET dynamic to compute a proxy of cerebral blood flow (i.e. K_1), although it was not possible to validate the obtained results because at the time no CBF data and no fully acquired ^{18}F-Flutemetamol dynamic were accessible, a comparison with the results reported in literature was performed to support our findings.

3.2 MR Acquisition Protocol

As the aim of our studies was to analyse the patients' functional and structural connectivity, our MR acquisition protocol at least included a T1-weighted image (isovoxel 1x1x1 mm^3), a T2-weighted image (isovoxel 1x1x1 mm^3), a 15min resting state BOLD-fMRI and a diffusion tensor imaging acquisition.
To take advantage of the full capability of the Biograph mMR scanner the simultaneous multi-slice (SMS) EPI, also known as multi-band (MB) EPI (K. Setsompop et al., 2012), acquisition technique was employed for both fMRI and DTI imaging. This technique, allowing the simultaneous acquisition of multiple slices yielding an equivalent reduction of measurement time and a consequent relaxation of the constraint for tuning the sequences (Feinberg and Kawin Setsompop, 2013).
The fMRI and DTI SMS-EPI pulse sequences that we included in the acquisition protocol were provided by University of Minnesota's Center for Magnetic Resonance Research (CMRR) through a master research agreement (MRA) with Siemens and then a Core Competence Partnership (C2P) agreement with CMRR.
After obtaining the pulse sequences, for each of them it was necessary performing a parameters fine-tuning in order to make the acquired images compatible with our research goals. More specifically, we focused on having a good voxel size and whole brain coverage. In the next two paragraphs we will briefly describe the process that was carried out to set the sequences up.

3.2.1 BOLD Functional Magnetic Resonance Imaging

Accordingly to the constraints of the Biograph mMR scanner and 12-channel head-neck coil, we performed the tuning of the fMRI MB EPI following the recommendation of the Human Connectome Project (HCP) as reported by Smith and colleagues (S. M. Smith, Beckmann, et al., 2013).
The use of the multi-band allowed us to obtain functional images with an isotropic voxel size of the order of 3x3x3mm^3 and a good temporal resolution, with repetition time (TR) substantially bellow 2s (lower than 1.5s), maintaining a near whole brain coverage and a good and spatially homogeneous temporal signal to noise ratio (tSNR) (Wald and Polimeni, 2015). The echo-time (TE) was set as close to 30ms as possible in order to match the typical T2* of most of the brain (Wald and Polimeni, 2015) to minimize the signal

dropout due to field inhomogeneity. In particular, signal dropout and geometric distortion are especially induced near orbitofrontal and inferior temporal regions of the brain, namely where sinuses and other air-tissue interfaces cause large susceptibility gradients (P Jezzard and Balaban, 1995; Ciris and Todd Constable, 2015). To avoid decreasing in image SNR, no in-plain acceleration was performed (i.e. GeneRalized Autocalibrating Partial Parallel Acquisition (GRAPPA, Griswold et al., 2002) equals to 0). These choices provided a good overall balance in which both spatial and temporal resolution were significantly improved if compared with the conventional single band fMRI data.
Since the duration of the functional acquisition was set to 15min (which is in a general the fMRI run duration required in order to provide a reliable and reproducible FC estimation according to the findings reported by Anderson and colleagues (Anderson et al., 2011) and thereafter confirmed by Birn and co-workers (Birn et al., 2013) and by Gonzalez-Castillo and collaborators (Gonzalez-Castillo et al., 2014)), the multi-band did not reduce the acquisition time, but increased the statistical power of the functional connectivity analysis by increasing the number of samples of the BOLD activity signal thanks to a reduced TR.
In addition, as the EPI acquisition is prone to geometric distortion which become more important when no in-plain acceleration is applied, beside the fMRI BOLD images, two spin echo EPI images with reverse phase encoding directions were acquired. These two spin echo images had the same geometrical, echo spacing, and phase encoding direction parameters as the BOLD-fMRI images (according to what is suggested in (Glasser et al., 2013)), and were exploited to perform the readout distortion correction of the functional images (Peter Jezzard, 2012). Moreover, as suggested in (Glasser et al., 2013), the single band reference was saved and subsequently used as template for the realignment fMRI preprocessing step and for an accurate registration of the EPI to the T2-weighted anatomical scan.

3.2.2 Diffusion Tensor Imaging

DTI is the technique of choice for the studies of in-vivo brain tractography and derived structural connectivity. The diffusion tensor is still the most commonly used model to relate the diffusion-weighted MRI signal to the underlying water diffusion process in biological tissues, however it is now

widely acknowledged to be inadequate for this purpose and that it's limitations have important implications for application such as diffusion-based tractography (Farquharson et al., 2016). Indeed, the tensor framework assumes a single straight fibre orientation within each imaging voxel, and is hence inadequate for the purpose of describing diffusion data within voxels containing complex fibre configurations or multiple fibre populations (crossing-fibres). The impact of crossing fibres has important implications for the application of tractography, as the DTI model provides incorrect fibre orientation estimates, this result in the delineation of false negative or false positive delineation of white matter pathways. The high angular resolution diffusion-weighted imaging (HARDI) (Hirsch et al., 2003; D. C. Alexander and Barker, 2005; Tournier, Calamante, Gadian, et al., 2004) was developed specifically to overcome these limitations and to provide more robust fibre orientation estimates for diffusion tractography application. Thus, the diffusion sequence we included in our protocol was an HARDI acquisition. The HARDI acquisition is essentially identical in nature to the standard DTI acquisition, and differs only in that a larger number of unique diffusion-weighting gradient directions are used (typically greater than 60). For this reason, the tuning of the diffusion MB pulse sequence focused mainly on increasing the number of diffusion-weighting gradient directions (>90), maintaining the acquisition time compatible with the clinical constraint, i.e. lower than 20min. A number of factors contribute to an accurate mapping of the white matter fibres, in particular the voxel size, the accuracy of the EPI readout distortion correction, the b_{value} and the ability to disentangle the different tissues. Concerning the voxel size, as we were principally interested in the cortico-cortical connectivity, it has been decided to favour a better spatial resolution (about 2x2x2mm^3) and a good SNR, rather than whole brain coverage (with cerebellum partially excluded from the field of view). To perform an optimal distortion correction we used a double phase encoding acquisition. Unfortunately, the drawback of this approach was that the acquisition time duplicated, as for each diffusion-weighting gradient direction two volumes were acquired with anti-parallel phase encoding directions. It is generally acknowledged that higher b-values (i.e. b = 3000 s/mm^2) lead to a better estimation of fibre orientation (Farquharson et al., 2016), however while setting the pulse sequences b-values we dealt with the limited performance of the Biograph mMR gradients. Therefore, the selected b-values were a trade-off between the image SNR (which is tightly related to the multi-band factor) and the scanner capability. An example of diffusion orientation distribution function

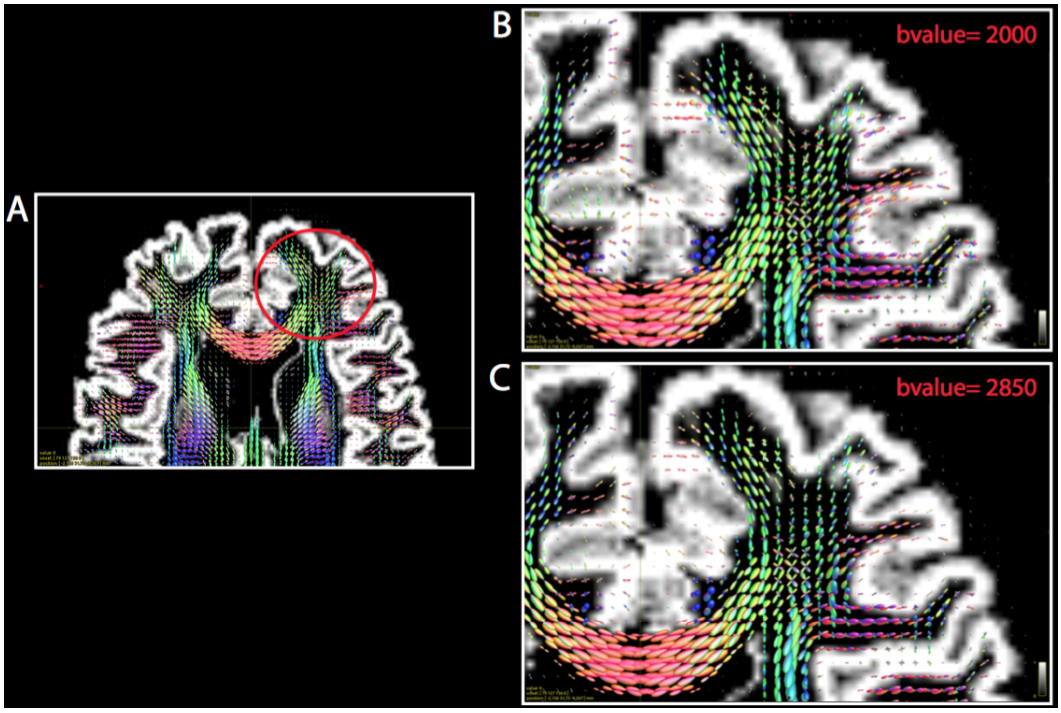

Figure 3.6: Example of fibre orientation distribution (FOD) estimates obtained from a two-shell HARDI acquisition with the higher b-values set to 2000s/mm^2 (B), and to 2850s/mm^2 (C), using the multi-shell spherical deconvolution method described in (Jeurissen et al., 2014). The panel A represents the anatomical region (red circle) from which the B and C images are extracted. This region is rich of crossing-fibres and allows us to appreciate the different ability of the two acquisition to disentangle this type of fibres. A narrow FOD results in a greater ability in distinguish the white matter fibre passing through the voxel.

obtained with different b-values is reported in Figure 3.6 To disentangle multiple tissues and to reduce partial volume effect, a multi-shell HARDI was employed. A two shell experimental setup was employed, whose b-values were selected as in (H. Zhang et al., 2012). Finally, as also distributions of the diffusion-weighting gradient directions affect the white matter fibre tracking, according to (Caruyer et al., 2013), we choose a uniform distribution of the directions.

To summarize, the diffusion acquisition included in the protocol consist in a two-shell HARDI acquisition with more than 90 diffusion-weighting gradient directions and b-values selected according to (H. Zhang et al., 2012) and to (Caruyer et al., 2013). These choices provided an adequate overall balance between spatial resolution and diffusion directions, if compared with the conventional single band diffusion data acquisition, and allowed both tractography and micro-structural (for example using the neurite orientation dispersion and density imaging (NODDI) model proposed by (H. Zhang et al., 2012)) analyses with same experimental protocol.

Chapter 4

Multimodal Approaches to Connectivity Analysis in Parkinson's Disease

4.1 Introduction

In this chapter a first application of the proposed framework is described and critically discussed. To evaluate the its effectiveness in clinical settings, the pipeline was used to study with a multimodal approach the brain connectivity of patients affected by Parkinson's disease.
Diagnosis of Parkinson's disease (PD) relies on the presence of specific motor symptoms such as bradykinesia, resting tremor, and rigidity (Biundo, Weis, and Antonini, 2016). Besides these symptoms, a significant number of patients with PD also develop either mild cognitive impairment or frank dementia (Edison, Rowe, et al., 2008). The reported prevalence of dementia in PD rises with disease duration and averages at around 40%. Compared with healthy age-matched controls, PD is associated with a six-fold higher risk of developing dementia and this is characterized by impairment of short-term recall, attention, visuospatial and executive functions such as decision making (Janvin et al., 2006; David J. Brooks, 2009).
Multiple pathological processes have been linked to dementia in PD: degeneration of basal forebrain cholinergic nuclei, frontal-subcortical circuit deafferentation due to degeneration of brainstem dopaminergic neurons, diffuse cortical Lewy bodies associated with α-synuclein, and Alzheimer-like lesions with β-amiloid (Aβ) plaques (Gomperts et al., 2013). Among these processes, the presence of Aβ is one most studied in the recent year (Hepp et al., 2016), as it seems to be related to the severity of the cognitive pathology (David J. Brooks, 2009; Edison, Rowe, et al., 2008) and to be a prognostic negative factor (Hepp et al., 2016; Petrou et al., 2012). The Aβ load studies were carried

out both from PET imaging perspective using Aβ highly sensitive tracers, such as ^{11}C-Pittsburgh Compound-B (^{11}C-PIB) (David J. Brooks, 2009; Edison, Rowe, et al., 2008; Gomperts et al., 2013), and from histopathological perspective (Hepp et al., 2016).

Besides these studies, other studies were carried out with the aim to understand and describe how brain networks, that underpin the deteriorated cognitive functions, are altered by pathology. In particular, resting state functional connectivity has proven to be an useful technique to investigate this type of changes (Biundo, Weis, and Antonini, 2016; Peraza et al., 2015; Elman et al., 2016; Gratwicke, Jahanshahi, and Foltynie, 2015). Since the presence of high amyloid load in Alzheimer's disease (AD) has been related to alterations in functional and structural connectivity (Yongxia Zhou, Yu, and Duong, 2015), and the dementia associated with Parkinson disease when amyloid Aβ is present has similar characteristics to AD, in this study was evaluated whether there were a relationship between amyloid burden and brain connectivity changes. Moreover, as , according to (Rodell et al., 2017), amyloid deposition seems to be related to a dendritic spine pathology with consequent inhibition of brain energy metabolism and reduction of blood flow by neurovascular coupling, a comparison between the pattern of blood flow between Aβ positive and negative patients were performed. Finally, it was also tested whether these changes in CBF could be significantly related to changes in brain connectivity, as those two phenomena are tightly linked (Qiu et al., 2017; Liang et al., 2013; Lou et al., 2016), in particular for BOLD-based connectivity.

Simultaneous PET/MRI acquisitions were employed to acquire time matched amyloid load, brain perfusion, and brain connectivity. A multimodal integration was performed to study the relationship among them. Amyloid load and brain perfusion were assessed using the recent ^{18}F-Flutemetamol tracer, one of the three currently Food and Drug Administration (FDA)-approved ^{18}F-labelled amyloid PET imaging agents. While, brain connectivity was estimate both as resting state functional connectivity and structural connectivity.

4.2 Materials and Methods

4.2.1 Dataset

This study involved twelve patients (8 men and 4 women; mean age 67.25y, range [57-77y]) affected by Parkinson's disease with different degree of cognitive decline, recruited at the Parkinson and Movement Disorders Unit, IRCCS (Istituto di Ricovero e Cura a Carattere Scientifico) San Camillo Hospital, Venice, Italy. Patients with suspect of AD-like dementia with concurrent Aβ deposition were enrolled for the present simultaneous PET/MRI study. The protocol for the experiments obtained the approval of the ethical committee of the University Hospital of Padova and all of the subjects had given written informed consent before the scans. All PD patients were diagnosed according to the UK brain Bank criteria (Gelb, Oliver, and Gilman, 1999). The possibility of diagnosis of Lewy Body Disease (LBD) was excluded according to international consensus criteria (McKeith et al., 2005). Cognitive assessment (including Montreal Cognitive Assessment (MoCA) and Mini Mental State Examination (MMSE) tests (Biundo, Weis, Bostantjopoulou, et al., 2016), and other selective tests for specific cognitive domains) was administered and used to quantify the cognitive impairment. The group characteristics are reported in Table 4.1.

Groups	**Age**	**Disease Duration**	**Cognitive State**	**MMSE$_c$**	**MoCA$_c$**
$A\beta$-POS	70 ± 7y	6.7 ± 4.0y	PDD	20.2 ± 4.6	14 ± 2
$A\beta$-NEG	$67 \pm 8y$	12.7 ± 6.7y	MCI/PDD	24.3 ± 1.8	21 ± 4

Table 4.1: Demographic informations.

Patients were separated by an expert nuclear physician (Prof. D.C.) in two groups according to the cortical amyloid load assessed using the static ^{18}F-Flutemetamol PET patient's image. The distinction was performed following the FDA recommendation for this specific tracer. Hence patients were marked as amyloid positive (Aβ-POS) when their images exhibited an altered pattern of tracer uptake in which white and grey matter boundaries were difficult to disentangle, whereas patients were reported as amyloid negative (Aβ-NEG) when in their images the white-grey matter intensity ratio was preserved.

Two patients were discarded because they were not able to complete the PET/MRI scan and two were discarded due to excessive head movement during the acquisition, which made the majority of the images unusable.

4.2.2 PET/MRI Brain Imaging Acquisition Protocol

Simultaneous PET/MRI scans were acquired at the Nuclear Medicine Unit, Department of Medicine – University Hospital of Padova, on a Siemens Biograph mMR (Siemens Medical Solutions USA, Inc.) equipped with a commercial PET transparent 16-channels head-neck coil (4-channels neck).
For reasons related to the organization of the Nuclear Medicine Unit and patient comfort, it was not possible to acquire the entire PET dynamics for 110 consecutive minutes, as suggested in literature (Heurling et al., 2015) for a full dynamic analysis, so, after the tracer injection, each patients underwent two subsequent session of simultaneous multimodal acquisition, as shown in Figure 4.1. Each session lasted 20 minutes; the first session, to which we will refer in the future as *early phase*, was acquired immediately before the radiopharmaceutical administration, while the second, *late phase*, started 90 minutes later. Between the two sessions the patients were free to leave the scanner and were repositioned into it before the start of the second session.
The MR brain imaging protocol included the following sequences:

- Ultra-short Time Echo (UTE), TR/TE1/TE2 11.9/0.07/2.46 ms, voxel dimension of 1.6x1.6x1.6 mm^3, FOV 300 mm, 192 slices
- 3D T1 (T1w) Magnetization-Prepared Rapid Gradient-Echo (MPRAGE) TR/TE 2400/ 3.2 ms, voxel dimension of 1x1x1mm^3, FOV 256 mm, 160 slices
- 3D T2-weighted, TR/TE 3200/536ms, voxel dimension of 1x1x1mm^3, FOV 256 mm, 160 slices
- Resting state functional MRI (fMRI) Echo-planar Imaging (EPI), two-fold acceleration with GRAPPA (Griswold et al., 2002), SMS (CMRR, R014) 2, TR/TE 1100/30 ms, FA 63° (set by Ernst Criteria), voxel dimension of 3x3x3mm^3, FOV 204 mm, 40 slices, anterior-posterior (AP) phase encoding direction, 800 dynamic scan

- two fMRI geometrically matched spin echo (SE) EPI, two-fold acceleration with GRAPPA, SMS 1, AP and posterior-anterior (PA) phase encoding direction
- 3D T1 Magnetization-Prepared Rapid Gradient-Echo (MPRAGE) TR/TE 2400/ 3.2 ms, voxel dimension of 1x1x1mm^3, FOV 256 mm, 160 slices
- two Diffusion Tensor Imaging (DTI), SMS (CMRR, R014) 2, TR/TE 4600/90 ms, voxel dimension of 2.3x2.3x2mm^3, FOV 220 mm, 64 slices, 1 shell at b-value of 1000 (60 directions), AP and PA encoding direction respectively

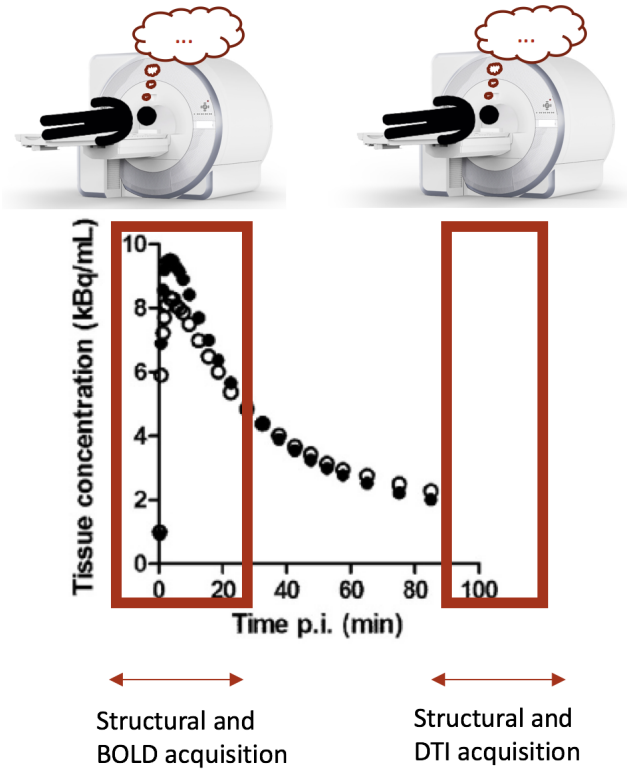

Figure 4.1: Time-line of the acquisition protocol: the two red boxes delineate respectively the *early* and *late phase*

More specifically, the first five sequences were acquired during the *early phase*, while the remaining sequences in the second session (*late phase*).
Concerning the PET protocol, an average dose of 180 MBq (range: 165–196 MBq, according to the body mass index and glycaemia) of ^{18}F-Flutemetamol (a 3'-fluoro-analogue of ^{11}C-Pittsburgh Compound B (^{11}C-PiB) developed by GE Healthcare) was administered to each patient by an intravenous bolus

injection. As no MR-compatible injection pump was available, the radiotracer was manually intravenously administered. The injection and subsequent saline flush lasted about 40 seconds. To reduce the variability caused by this method of administration, the same nuclear physician (Prof. D.C.) has always carried out injection. PET ^{18}F-Flutemetamol emission data from both *early* and *late phase* were acquired in list-mode format. No arterial blood sample was collected because the facility that houses the PET/MRI scanner does not have an MR-compatible arterial sampling system.

4.2.3 PET Data Analysis

PET Images Reconstruction

PET images were offline reconstructed using the e7-tool for Biograph mMR, as described in Chapter 3. Firstly acquired sinogram was corrected for scatter, dead time and attenuation due to head and radio-frequency coil, then decay and normalization correction was performed and finally the 3D ordinary Poisson ordered subset expectation maximization (OP-OSEM) algorithm with 3 iterations and 21 subset was applied to the corrected sinogram. It should be noted that, at the time of the analysis, the algorithm for computing the attenuation map from the T1 MPRAGE (Izquierdo-Garcia et al., 2014) had not yet been integrated into the reconstruction pipeline, therefore the attenuation correction was performed using the μmap calculated from the UTE sequence.

PET Time Binning for Image Derived Input Function

As the interest was in modelling the rising of the PET time activity and quantify the simplified compartmental model introduced in the previous chapter, the *early phase* tracer dynamic was reconstructed for the first 10 minutes.
Four different framing time grid were tested to evaluate which was the most accurate to extract the image derived input function. In particular, the PET *early phase* dynamic was reconstructed using the following grid: 5x2min (*TG1*); 10x1min (*TG2*); 20x30s (*TG3*); 30x10s plus 10x30s (*TG4*). The best timing grid was selected as the grid that allowed to better identifying the characteristic features of the image derived input function (namely lower time to peak and higher peak amplitude), and that led to consistent time to peak among the patients. Consistency among patients was evaluated only in terms of time

to peak as due to the different amount of injected tracer dose a less uniformity in peak amplitude was expected. Moreover, since in this study MR angiographic data were not available and hence it was necessary to manually drawn the pool of arterial voxels to be used to compute the IDIF, for each time grid the ease of segregate the common carotids from the background in PET images was evaluated by means of the contrast to noise ratio.
Once the common carotids ROIs were defined, for each patient the IDIF was computed as the average of the time activity curves of the selected voxels. No partial volume correction (PVC) was performed, as it was hypothesised that these vessels were large enough to make negligible the partial volume effect, such as in left ventricle or ascending aorta (Zanotti-Fregonara et al., 2011).
An example of the same time activity curve of the left carotid reconstructed with the four time framing is reported in Figure 4.2.

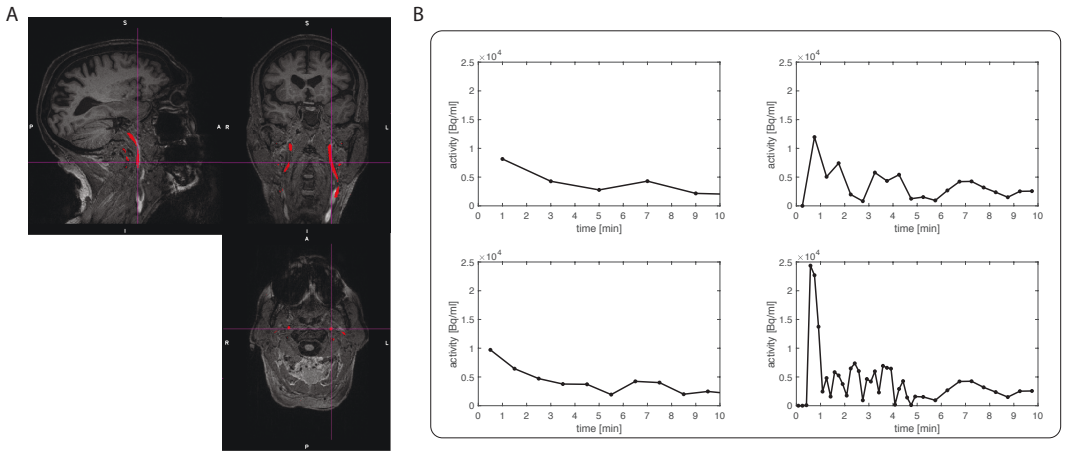

Figure 4.2: on the panel A, in grey scale scale the patient's MPRAGE, in red the over-imposed map of the vessels, in purple marker that points to the pool of voxels inside the internal carotid from which the IDIF were extracted. On panel B, the extracted time activity curve reconstructed using four different time grid: top-left, 2-minutes sampling step (*TG1*) ; bottom-left, 1-minutes sampling step (*TG2*); top-right, .5-minutes sampling step (*TG3*); bottom-right, framing intervals of 30x10s and 10x30s (*TG4*).

Neck vessels are visible in different MR-structural images other than TOF, such as the T1w MPRAGE, however it has been decided to not exploit these images to identify the vessel because those are elastic structures housed in a critical area for movement and, consequently, even a small displacement

between PET and MR images would have potentially compromised the segmentation once mapped in PET space. An example of the mismatch between T1w image and PET volume corresponding to the IDIF peak is shown in Figure 4.3.

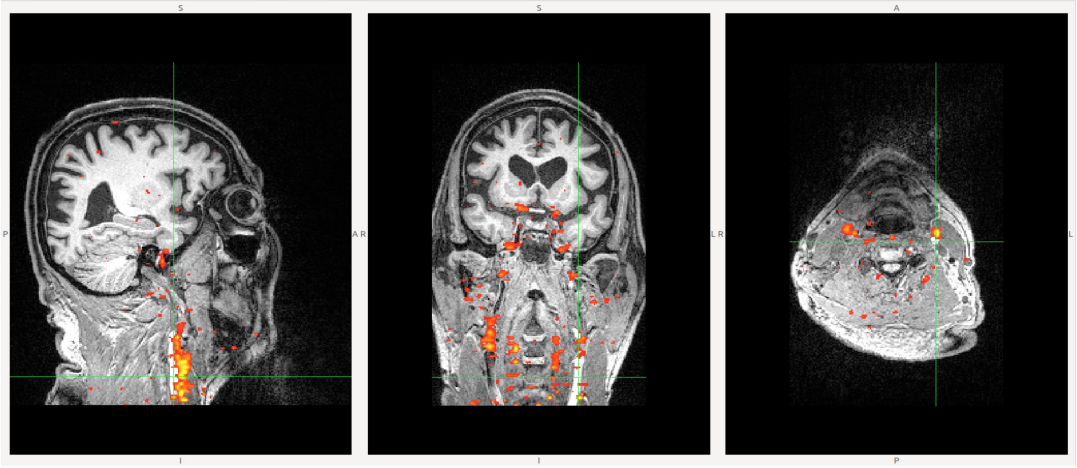

Figure 4.3: Example of spatial mismatch between T1w image and PET in Aβ-NEG patient. Structural T1w image in grey scale, PET volume corresponding to the IDIF over-imposed in red-yellow scale and rescaled to highlight the vessels information content. Green cross points to the centre line of the left common carotid in T1w image.

From the figure it is clear that although the two images were acquired simultaneously, if the patient has moved slightly during the time interval between the volume corresponding to the arterial signal peak and the T1w image acquisition, this can cause a wide mismatch in terms of neck vessels.

PET Reconstructed Images Preprocessing

In order to relate the results of PET analyses to those obtained from the analysis performed on the MRI signal, we chose to work at region of interest (ROI) level rather than at voxel level, since functional connectivity is usually analysed at ROI level. Being mainly concerned with the integration of information coming from the two techniques from a functional networks point of view, we decided to employ the functional atlas proposed by Gordon et al. (E. M. Gordon et al., 2016) for the cortical grey matter and the MICCAI2012 atlas (publicly available from the 2012 MICCAI Multi-Atlas Labelling Challenge) for the deep grey matter nuclei. Both atlases work at subject level, therefore the *early phase* T1w MPRAGE has been parcelled for each patient, as will be described in the MR devoted session of this chapter, and then the obtained parcellation was mapped respectively in the *early-* and *late-phase* PET

single subject space. This preprocessing step was carried out using the Advanced Normalization Tool (ANTs) software (Avants, Tustison, Song, et al., 2011; Avants, Tustison, Stauffer, et al., 2014). To register the parcellation to the *early phase* PET space it was enough to apply the affine transformation estimated by the scanner. While for the *late phase* space registration we additionally computed a non-linear transform to map the *early phase* T1w MPRAGE to the *late phase* T1 MPRAGE and concatenated the obtained diffeomorphic deformation field with the scanner affine transform before mapping the parcellation.
Exploiting the EPI (resting state and DTI) acquisitions, it was possible to verify that there were no large movements of the patients head during the scan, if related to the PET scanner spatial resolution (i.e. 4.3 mm, as reported in (Catana, 2017)), and, moreover, as previously mentioned, patients with great head displacement were discarded due to poor MR image quality. Hence, it was decided not to perform any motion correction step either on *early* or on *late phase* data. Conversely, as we will discuss in the next paragraphs, the MRI data is more sensitive to movement and therefore correction for movement on that data has proved to be crucial.
Finally, the grey matter parcelling moved into PET space was used to extract the mean time activity curve of each ROI.

Early Phase PET Signal Quantification: estimate of the CBF proxy

The *early phase* PET dynamic has been quantified at ROI level using the method described in the Chapter 3. The simplified one irreversible compartment (1TC) was employed. Albeit we were working at the regional level, being aware of that the signal we were dealing with would be particularly noisy, mainly due to the low dosage employed, we have decided to implement 1TC model with two different measurement equations. This approach allowed us to include or not in the model a parametrization of the fraction of blood volume, which is known to be one of the most difficult parameters to estimate in case of noisy data, as its estimate relies on the first few frames of the PET dynamic that typically have low signal to noise ratio due to the reduced number of counts.
For each patient, the two models described by equation 3.4 and 3.5 were fitted at ROI level within a time window ranging from 0 minutes to the time at which the average grey matter time activity curve reaches the maximum (less than 3 minutes after the tracer injection, this interval is in line with findings of Rodriguez-Vieitez and colleagues (Elena Rodriguez-Vieitez et al., 2017) and

with findings reported in Chapter 3), using a linear least square approach without weighting the data.
The model that best fits the data was selected according to the Akaike information criterion (Akaike, 1974). The influx rate constant (K_1,$(ml/cm^3/min)$) obtained with the winner model were then used as a proxy of the CBF, as discussed in Chapter 3.
The IDIF extracted with the best time framing reconstruction was employed as model input function. Since the model hypothesis is that the arterial input is not affected by noise, the extracted dynamic has been fitted using the tree-exponential model as proposed by (Feng, Huang, and X. Wang, 1993). The time to peak and peak amplitude were fixed in order to reduce the number of model's parameters that would have been estimated. As mentioned in the Chapter 3, one severe limitation of IDIF when applied to tracers such as the ^{18}F-Flutemetamol is that it cannot distinguish the parent compound from its radioactive metabolites and the plasma radioactivity to that of whole blood (Zanotti-Fregonara et al., 2011). Therefore the percentage of tracer metabolites needs to be quantified to correct the IDIF for this confound. Nevertheless, since the ^{18}F-Flutemetamol is a derivative of ^{11}C-PiB, whose metabolites behaviour is well described in (Price et al., 2005) and in (Edison, D. J. Brooks, et al., 2009), and the time window where the model was fitted is confined within the first few minutes (less than 3 minutes), we assumed that the presence of metabolites could be considered negligible. This hypothesis is supported by the plot of the calibrated arterial input functions generated for the whole blood activity concentration, the total plasma activity concentration, and the parent ^{11}C-PiB plasma activity concentration reported in the work of Edison and colleagues (Edison, D. J. Brooks, et al., 2009). Moreover, we assumed that $C_b(t)$ was equal to $C_P(t)$, i.e. the tracer uptake by the red-blood cells is negligible. So the fitted IDIF was employed as noise-free input of the 1TC model instead of the unavailable metabolites-corrected plasma input function.

βAmyloid Load Assessment

The Standard Uptake Volume Ratio (SUVR) was employed to quantify the βAmyloid load, as the cortical uptake increase occurs in proportion to fibrillary βAmyloid levels. SUVR is a semi-quantitative measure of tracer uptake normalized to the mean uptake in a reference region, and it is computed as the ratio between the integrated activity of the voxel over a given period and the integrated activity of the reference region over the same given period. For

the ^{18}F-Flutemetamol radiotracer the reference region is commonly accepted to be the grey matter of the cerebellum (Leinonen et al., 2014), as it supposed to be an area devoid of β-amyloid deposits till the late stages of the pathology both in AD and AD-like patients.
The time window where signal integration is appropriate is between 90 and 110 minutes after injection (N. Nelissen et al., 2009), as in that interval the tracer has already reach the steady state.
The SUVR was computed for each patient at voxel level and then for each functional parcellation ROI of each patient the mean Standard Uptake Volume Ratio was extracted.
Moreover, all SUVR images were rated as normal (amyloid negative) or altered (amyloid positive) with respect to ^{18}F-Flutemetamol grey matter uptake pattern, by an expert nuclear physician (Prof. D.C.).

4.2.4 MRI Data Analysis

Structural Images Preprocessing and Parcellation

Each patient's *early-phase* MPRAGE was processed using a combination of the following software: Advanced Normalization Tools software (ANTs, Avants, Tustison, Song, et al., 2011), FMRIB Software Library (FSL, S. M. Smith, Jenkinson, et al., 2004), FreeSurfer Software Suite (http://surfer.nmr.mgh.harvard.edu), Caret (Van Essen et al., 2001) and Connectome Workbench (Marcus et al., 2011). The structural image was initially corrected for bias field using the N4 algorithm (Tustison et al., 2010) which minimizes the field inhomogeneity effects, and then the bias field corrected images were automatically parcelled using two different atlases: the Gordon atlas (E. M. Gordon et al., 2016) and the MICCAI2012 atlas. The choice of these two atlases arises from a compromise between good segmentation of the subcortical nuclei, provided by the MICCAI2012 atlas, and a refined functional segmentation for the study of the resting state networks, provided by the Gordon atlas.
In order to apply the Gordon segmentation, as reported in (E. M. Gordon et al., 2016), firstly the anatomical surfaces were generated from each subject's bias-field corrected MPRAGE using FreeSurfer's default *recon-all* processing pipe-line (excluding the N3 bias field correction). This pipeline included brain extraction, segmentation, generation of white matter and pial surfaces, inflation of the surfaces to a sphere, and surface shape-based spherical registration of the subject's "native" surface to the *fsaverage* surface (Fischl, Sereno, and Dale, 1999; Ségonne, Dale, et al., 2004; Ségonne, Pacheco, and Fischl,

2007). The fsaverage-registered left and right hemisphere surfaces were resampled to a resolution of 164000 vertices, and the Gordon atlas mesh was registered to the patient's resampled mesh, using the Freesurfer_to_fs_LR Caret script. Finally, each subject's surface was downsampled to a 32 492 vertex surface and the relative surface-based 333-ROIs parcellation back-projected into the volumetric MPRAGE reference system.

In order to obtain the MICCAI2012 atlas parcellation, the bias field corrected structural image was segmented into white matter (WM), cerebrospinal fluid (CSF), ventricles, and 120 cortical and 16 deep grey matter (GM) regions, using the multi-atlas segmentation algorithm with joint label fusion as implemented in ANTs (Wang and Yushkevich, 2013). Briefly, 35 manually segmented T1w images and associated manually labelled volumes (data publicly available from the 2012 MICCAI Multi-Atlas Labelling Challenge) were non-linearly registered to the T1w image of each patient. This produced 35 independent segmentation for each T1w image, which were then combined using the joint label fusion technique (Wang, Das, et al., 2011), obtaining a high quality anatomical parcellation of the entire brain.

The single subject Gordon parcellation and subcortical MICCAI2012 segmentation were then incorporated in an unique individual volumetric parcellation. More precisely, the Gordon parcellation included 333 ROIs, that can be grouped according to the following well known main resting state networks (RSN): Visual (VIS), Retrosplenial-Temporal (RSTN), Sensory-Motor hand (SMH), Sensory-Motor mouth (SMM), Auditory (AUD), Cingulo-Opercularis (CON), Ventral Attention (VAN), Salience (SAL), Cingulo-Parietal (CPN), Dorsal Attention (DAN), Fronto-Parietal (FPN), Default Mode Network (DMN). For this analysis, the selected subcortical regions were the left and right accumbens, caudate and pallidum nuclei, the left and right thalami and the cerebellum grey matter separated in left and right hemisphere.

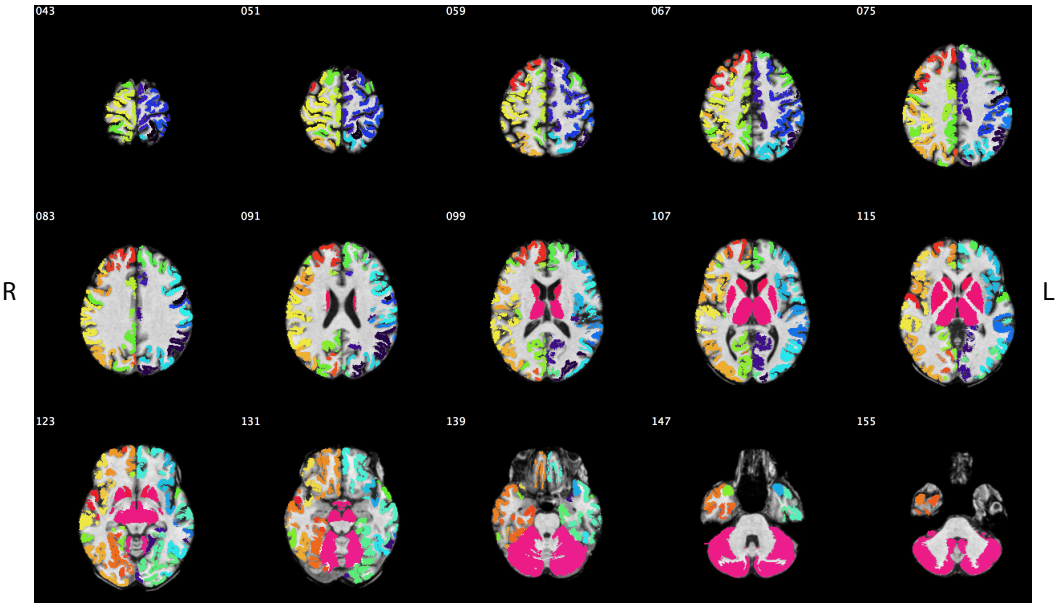

Figure 4.4: Final brain parcellation, each colour represents a single region of interest. The pink-scale parcels are the deep grey matter ROIs derived from the MICCAI2012 parcellation, the other colour-coded regions are the Gordon cortical regions.

Resting State Functional Connectivity

Functional connectivity (FC) is defined as statistical dependencies among remote neurophysiological events and it is usually inferred on the basis of correlations among measurements of neuronal activity (Friston, 1994; Friston, 2011). In recent years, there has been growing interest in the study of functional connectivity on patients that are not performing any specific task, i.e. in resting state functional connectivity. In particular, many studies have linked differences in FC with cognition and diagnosis (M. H. Lee, Smyser, and Shimony, 2013), like in the case of Parkinson disease. Several methods are available for estimating FC from fMRI images, and one of the most popular one is the atlas-based correlation analysis, mainly because the atlas parcellation can be used as a common framework for cross-modality and cross-subject quantitative analysis.

As we were interested in a multimodal approach to the study of the connectivity in PD patients with cognitive impairment, the atlas-based functional connectivity analysis was implemented. More specifically, this method requires the selection of a parcellation atlas, which should be consistent with

the subsequent analysis. Considering that this study was predominantly focused on the connectivity analysis of networks involved in cognitive functions, a parcellation that include both the Gordon atlas and the MICCAI2012 deep grey matter regions seemed to be a good choice.

Resting State fMRI Data Preprocessing The resting state acquisition of each patient was preprocessed in the individual space using the ANTs software. Since in the last five years several works highlighted how the presence of head motion has a severe impact on the study of functional connectivity in resting state (Power, Barnes, et al., 2012; Dijk, Sabuncu, and Buckner, 2012; Power, Schlaggar, and Petersen, 2015; Zeng et al., 2014; Joshua S. Siegel, Anish Mitra, et al., 2016) and we also experienced this issue in a study conduced on a large dataset of Multiple Sclerosis patients, particular attention has been paid to removing the variance introduced by head displacement during the acquisition.
Functional images were corrected for readout distortion, using the two SE images and the FSL's TOPUP algorithm (J. L. R. Andersson, Skare, and Ashburner, 2003). Data were then corrected for head motion with ANTs' *antsMotionCorr*; a 12-degree of freedom affine transformation was estimated to realign each volume to the single-band acquired volume. Moreover, ANTs' *antsMotionCorrStats* algorithm was employed to compute patient's head framewise displacement (FD, Power, Barnes, et al., 2012) from the estimated motion parameters.
The volumetric parcellation was required for the following FC analysis, so it was mapped from MPRAGE to fMRI space. The functional images were spatially normalized to the single subject *early-phase* MPRAGE in a two-step process: first, the single-band reference volume was registered to the T2w image using an affine transform and an additional diffeomorphic deformation field limited to the anterior-posterior direction; secondly, the T2w image was rigidly registered to the T1w. The estimated displacement fields and affine matrices were combined into a single concatenated transformation, which mapped fMRI space into the MPRAGE reference system; the inverse of this transformation was then used to move the MPRAGE parcellation to the fMRI space with a single interpolation step.
One of the primary sources of artefacts in FC is due to correlation of fMRI signals from non-neuronal physiological activity, such as residual motion, breathing and hearth beating. To remove remaining source of noise, we regressed out from each voxel of the motion-corrected image a set of signal of

no interest, which consisted in time courses of WM, CSF, 6 rigid-body motion parameters (describing rotations and translations along the three principal axes), and their derivatives (Jo, Gotts, et al., 2013; Power, A. Mitra, et al., 2014). The motion parameter were extracted applying the Cholesky decomposition to the affine transformation matrices estimated during the motion correction step. As in the Component Based Noise Correction Method (CompCorr, Behzadi et al., 2007), the WM and CSF signals were computed as the five top principal components of the voxels signals respectively within the WM and lateral ventricles masks, that were derived from the single subject parcellation. To note that the masks were eroded to prevent respectively inclusion of grey matter or white matter via partial-volume effect as reported in (Jo, Saad, et al., 2010). Finally, after regression, images were high-pass filtered (cut-off frequency 1/128 Hz).

FC matrices computation The time course of each ROI of the volumetric parcellation (moved into the fMRI space) was extracted by means of principal component analysis (PCA), which was here employed for additional de-noising purpose. The ROI time course was thus calculated as the average of the set of principal component that explained the 90 % of the variance of the time courses of all the voxels inside the region, the idea behind this choice was that at most the 10 % of the variance could be associated with non-interest phenomena.
Before computing FC matrices as cross-correlation between each pair of post-processed time courses, an high-motion data censoring was performed (Power, A. Mitra, et al., 2014; Joshua S. Siegel, Power, et al., 2014). Time points related with fMRI volumes highly corrupted by motion were identified using the frame-wise displacement as proxy of patient's head motion and the corresponding samples removed from the time course itself. The FD threshold was set to 0.4, a trade-off between what was suggested by (Power, A. Mitra, et al., 2014) and the type of population we were studying. FC matrices were then z-Fisher transformed to allow following statistical comparisons.

Graph Theory An advantage of the atlas-based approach is that it gives the opportunity to interpret the matrix of functional connectivity as a matrix of adjacencies and to associate this matrix with a graph. In this way, the observed system can be interpreted as a network. The application of graph theory aims at ascribing nodes to various regions of interest, and generating

links or arcs between them. This approach makes it possible to explore functional connectivity networks using tools that characterize typical properties of networks, for example the study of efficiency and modularity.
A complex network can be represented mathematically by edges and nodes (Rubinov and Sporns, 2010). Mathematically, nodes represent different parts of a system, and the relationship between two nodes is represented by an edge. Applying these mathematical concepts to the brain, nodes represent different areas of the brain (the parcellation ROIs), while edges represent the connectivity between these nodes. In functional connectivity models, edge weighting indicates the magnitude of a correlation between brain areas.
Weak and non-significant links may represent spurious connections. These links tend to obscure the topology of strong and significant connections and as a result are often discarded, by applying an absolute, a proportional weight, or a sparsity threshold. We implemented a sparsity thresholding, whose threshold was set at 0.8. This decision is a trade off between a sparse network (low threshold) and a highly linked one (high threshold).
In this study graph measures that both described the centrality of each node within the network, such as node degree, node strength and betweenness centrality, and characterized the functional segregation, such as clustering coefficient and local efficiency has been used.
The degree (Deg) is one of the most common measures of centrality, and is defined as the number of links connected to that node, which in practice is also equal to the number of neighbours of the node itself.

$$Deg(i) = \sum_{\substack{j \in N \\ j \neq i}} \delta(i,j) \qquad \delta(i,j) = \begin{cases} 1 & W(i,j) \neq 0 \\ 0 & W(i,j) = 0 \end{cases}$$

where N is the set of the network nodes and W is the functional connectivity matrix. The degree has a straightforward neurobiological interpretation: nodes with a high degree are interacting, functionally, with many other nodes in the network, various study related a decrease of node degree to cognitive decline as observed in Alzheimer's patients.
The node strength (Str) is defined as the sum of the weight of links connected to that node:

$$Str(i) = \sum_{\substack{j \in N \\ j \neq i}} W(i,j)$$

The betweenness centrality (BC) is defined as the fraction of all shortest paths in the network that pass through a given node:

$$BC(i) = \frac{1}{(n-1)(n-2)} \sum_{\substack{h,j \in N, \\ h \neq j, h \neq i, i \neq j}}^{N} \frac{\rho_{hj}(i)}{\rho_{hj}}$$

where n is the number of nodes, ρ_{ij} is the number of shortest paths between h and j, and $\rho_{ij}(i)$ is the number of shortest paths between h and j that pass through i. Bridging nodes that connect disparate parts of the network often have a high betweenness centrality.
Locally, the fraction of triangles around an individual node is known as the clustering coefficient CC and is equivalent to the fraction of the node's neighbours that are also neighbours of each other:

$$CC(i) = \frac{2t_i}{k_i(k_i - 1)}$$

where k_i is the number of node neighbours, and t_i is the number of triangles around the node, that is computed as:

$$t_i = \frac{1}{2} \sum_{j,h \in N} (W(i,j)W(i,h)W(j,h))^{1/3}$$

To compute these graph measures from the FC matrices the Brain Connectivity Toolbox (Rubinov and Sporns, 2010) was employed.

Structural Connectivity

Structural connectivity describes anatomical connections linking a set of brain regions. These connections generally refer to white matter projections linking cortical and subcortical regions. Axons that share a similar destination tend to form larger bundles, called white matter tracts. The major tracts can be delineated by DTI with 2–3 mm image resolution using so-called tractography or fibre-tracking algorithms. They operate based on the voxel- wise information provided by DTI to infer connections between adjacent voxels that may belong to the same tract, thereby reconstructing the white matter architecture (tractogram) in 3D (Tournier, Mori, and Leemans, 2011).
The tractogram could be then converted into a connectome (or structural connectivity (SC)) matrix, based on a brain parcellation scheme, such as the parcellation previously described.

Diffusion MR Data Processing Diffusion MR data processing was performed using the MRtrix3 software (http://www.mrtrix.org).
Patient head motion during acquisition is a major challenge for diffusion imaging data, as well as for functional data, since it severely affect the quantification of diffusion parameters and the resulting structural connectivity matrix (Tournier, Mori, and Leemans, 2011).
For each patient, a manual data checking was performed in order to identify and discard motion-corrupted volumes, a step that works like the data censoring in fMRI. Patients with less than 60 volumes retained after this step were removed from subsequent analysis. In total, two subjects were discarded for this reason.
Data preprocessing was then executed using the *dwidenoise* and *dwipreproc* scripts. The *dwidenoise* was applied both to blip up and down DTI acquisition (i.e. DTI images acquired with respectively AP and PA readout). It improves the SNR of the diffusion data reducing the effect of thermal noise, and exploits data redundancy in the PCA domain using the prior knowledge that the eigenspectrum of random covariance matrices is described by the universal Marchenko Pastur distribution (Veraart et al., 2016). This *dwipreproc* script then executes the actual preprocessing of diffusion image data and includes eddy current-induced distortion correction, motion correction (i.e. realignment of volumes), and susceptibility-induced distortion correction (using the two acquired encoding directions of each gradient direction and the FSL's TOPUP tool) (J. L. R. Andersson, Skare, and Ashburner, 2003; J. L. Andersson and Sotiropoulos, 2016; S. M. Smith, Jenkinson, et al., 2004).
The single-shell constrained spherical deconvolution as reported in (Tournier, Calamante, Gadian, et al., 2004; Tournier, Calamante, and Connelly, 2007) and implemented in the MRTrix3 software was used to compute the fibre orientation density function (FOD). From the estimated FOD the 5-millions-streamlines tractogram was computed using the probabilistic fibre-tracking algorithm implemented by default in MRTrix3 with the option *anatomically-constrained tractography* (ACT, R. E. Smith et al., 2012) turned on and the minimum-length constrain set at 4 mm. In short, the algorithm identifies suitable position from which to initiate the streamline (the seed point), propagates the track along the estimated fibre orientation, and terminates the track when appropriate termination criteria are met. ACT causes streamlines only to terminate precisely at the grey matter - white matter interface, within sub-cortical grey matter, or at the inferior edge of the image. Whereas minimum-length criterion essentially acts as a noise filter, removing short

spurious tracks for which the support is poor given the diffusion image data. Moreover, in order to improve the quantitative nature of whole-brain streamlines reconstructions the spherical-deconvolution informed filtering of tractograms (SIFT, R. E. Smith et al., 2013) was applied to the obtained tractogram. This approach carries out a track pruning based on the FOD, which in our case resulted in a 2.5-million-streamlines tractogram.

Structural connectivity matrix The volumetric parcellation that included Gordon and MICCAI2012 ROIs was employed to convert the tractogram to structural connectivity (connectome, (Catani et al., 2013)) matrix. Since, from a structural point of view, the main interest of the study was to identify possible retrograde degeneration associated with amyloid deposition, the connectivity metric that was employed was the streamline count. What was expected was a decrease of the number of streamlines due to an increase of amyloid load.

Graph Theory A complex-network graph was associated with the structural connectivity matrix as in (Bassett et al., 2008) and in (L. Wang et al., 2009). The nodes of the graph were the parcellation ROIs, and the edge weights in this case represented number of detected streamlines between the nodes. Since the SC matrix for construction is sparse, no threshold has been applied. We then computed the same metrics previously calculated for the FC matrix; namely node degree, node strength, betweenness centrality, clustering coefficient and local efficiency.

4.2.5 Statistical Analysis and Multimodal Integration

After establishing the effectiveness and reliability of the results assessed using the proposed framework, despite the severe limitation represented by the size of the dataset, an attempt of statistical analysis was performed to evaluate whether there were or not a significant relationship between connectivity and the biological processes estimate from PET data. The comparisons were performed between the two groups of Aβ positive and negative patients, that were classified according to the SUVR-based medical report.
First of all, we separately tested the two group for significant differences in K_1, SUVR, functional connectivity and structural connectivity. Then we checked for significant relationship both between alteration in connectivity and in the proxy of CBF, and between changes in connectivity and in amyloid load.

As suggested in (Bassett et al., 2008) and in (Y. He et al., 2009), changes in connectivity were quantified as differences in graph theory metrics separately computed from the average connectivity matrices of Aβ-NEG and Aβ-POS groups. Variation in K_1, SUVR were computed as ROI-wise differences between the groups average maps of the two parameters.
Concerning the PET results, for each single ROI the K_1 group average was computed for both Aβ-POS and Aβ-NEG groups. To evaluate whether there were a significant difference between the two groups at whole brain level, the group mean K_1 of all the ROIs were compared in median and dispersion respectively with the Wilcoxon rank sum and Ansari-Bradley tests. The two tests were implemented in a permutation test framework with 20.000 permutations. In addition, at ROI level, differences in K_1 between amyloid positive and negative patients were determined with Wilcoxon rank sum test. As in the previous analysis, a permutation test was implemented, but, considering the very limited number of samples for each group, it was possible to perform an exact permutation test. The same comparisons were also carried out for SUVR values.
Regarding the connectivity analysis, we inspected the mean functional connectivity matrices of the Aβ-POS and Aβ-NEG groups both in terms of FC weight distribution and in terms of matrix structure. To assess differences in median and dispersion of the two functional connectivity distributions, the Wilcoxon rank sum and Ansari-Bradley statistics were implemented within a permutation test framework (20.000 iterations). In addition, the Krzanowski test (Krzanowski, 1993) was employed to investigate differences in mean FC matrices structure. Since we hypothesised that differences between the groups could be restricted to single specific resting state networks, we further compared the structure of the sub-matrix and the distribution of intrinsic and extrinsic connections for each single RSN as in (Brier et al., 2012). Intrinsic and extrinsic connections index respectively the set of links between all the nodes of a specific network, and set of the links of all the nodes of that specific network with the rest of nodes. More specifically, they represent two different characteristics of the resting state network, the first shows how the RSN is self-connected, i.e. how the associated function is segregated (Friston, 1994), and second how the RSN is related with all the other brain regions.
Furthermore, to summarize the connectivity characteristics the node degree,

node strength, betweenness centrality, clustering coefficient and local efficiency were computed from the two groups mean FC matrices and the Wilcoxon rank sum test was employed to test whether there were significant differences between the groups both at whole brain level and at RSN level.
Similarly, the two groups structural connectivity matrices and the related graph measure were compared.
To obtain an integrated description of connectivity, both from a PET and MRI point of view, we tested whether there was a relationship between changes in functional and structural connectivity graph theory metrics and the increase of amyloid load in Aβ positive patients, by means of a correlation analysis (Pearson's correlation). A permutation test was performed both at whole brain network and at single RSN level, with 100.000 permutations. Moreover, as several studies conducted on AD patients reported that local alteration of cerebral blood flow seems to be related with the extent of cognitive impairment (Kisler et al., 2017), we evaluated whether FC and SC graph metrics correlated with the decrease of the proxy of CBF (i.e. K_1) in the amyloid positive group. Evaluation was performed with a permutation test (100.000 permutations) both at whole brain network and at single RSN level, the employed statistic was the Pearson's correlation too. In all tests significance value was set at 0.05 and the false discovery rate (FDR, (Benjamini and Hochberg, 1995)) was employed to correct for multiple comparison. The choice of non parametric tests was justified by the limited number of patients or by the non-gaussianity of the considered feature distribution (assessed by means of Kolmogorov–Smirnov test).
All analyses were performed using in-house developed MATLAB (The Mathworks Inc., Natick, USA) implementations of the cited tests, as well as PET data and connectivity analyses.

4.3 Results

Analysis results will be reported following the Material and Methods section order. We firstly show and discuss the results obtained the proposed framework both for PET time framing reconstruction and *early phase* PET data quantification. Later the ^{18}F-Flutemetamol static PET data are described, then the connectivity analysis results will be reported and finally we will describe the results of the multimodal analysis of connectivity.
Based on the clinical assessment, 3 patients resulted in having a positive β

amyloid load pattern ($A\beta$-POS group) and 5 a negative pattern ($A\beta$-NEG group).

4.3.1 PET Data Reconstruction and Analysis Results

Time Binning for IDIF Results

An example of the IDIF signal obtained for a single Aβ-NEG patient reconstructing the PET list-mode using the four proposed time grids is reported in Figure 4.2. From the image it is clear that the first two sampling grid (i.e. *TG1* and *TG2*) are not capable to capture the typical IDIF signal shape and that the obtained shape is far to be compatible with the commonly employed model to fit these type of data, such as the ones proposed by Feng et al. (Feng, Huang, and X. Wang, 1993) or by Tonietto and colleagues (Tonietto, Rizzo, Veronese, and Bertoldo, 2015). Concerning the two remaining time framing the one that led to the most consistent results within the dataset in terms of peak time was the *TG4* (i.e. the one with the lower frame length). For this framing we obtained a time to peak that was on average of 37.5s (range 25s $\div$ 45s) in the dataset. These results in terms of variability are compatible with manual injection and with the speed of the injection, which last at most 40s. Since the administration duration was so short, it was not possible to compare the obtained curves with literature results. Indeed, it is well known that this duration heavily impact on the IDIF or AIF shape, in particular regarding the peak amplitude and dispersion (Tonietto, Rizzo, Veronese, and Bertoldo, 2015).
The selected time binning was also the framing that gave better results in CNR. An example of the four PET volumes corresponding to the IDIF peak obtained in a single Aβ-NEG patient exploiting the four binning grids is shown in Figure 4.5, in addition, common carotids and background ROIs are depicted. ROIs were segmented in four consecutive slides paying attention to restrict the selection to slices where no PET reconstruction boundary effect was evident. A summary of the IDIF features obtained for this patients as well as CNR are reported in Table 4.2. As expected the peak amplitude definitely increase with the decrease of the frame length, the same pattern was observed for all the patients of the dataset.

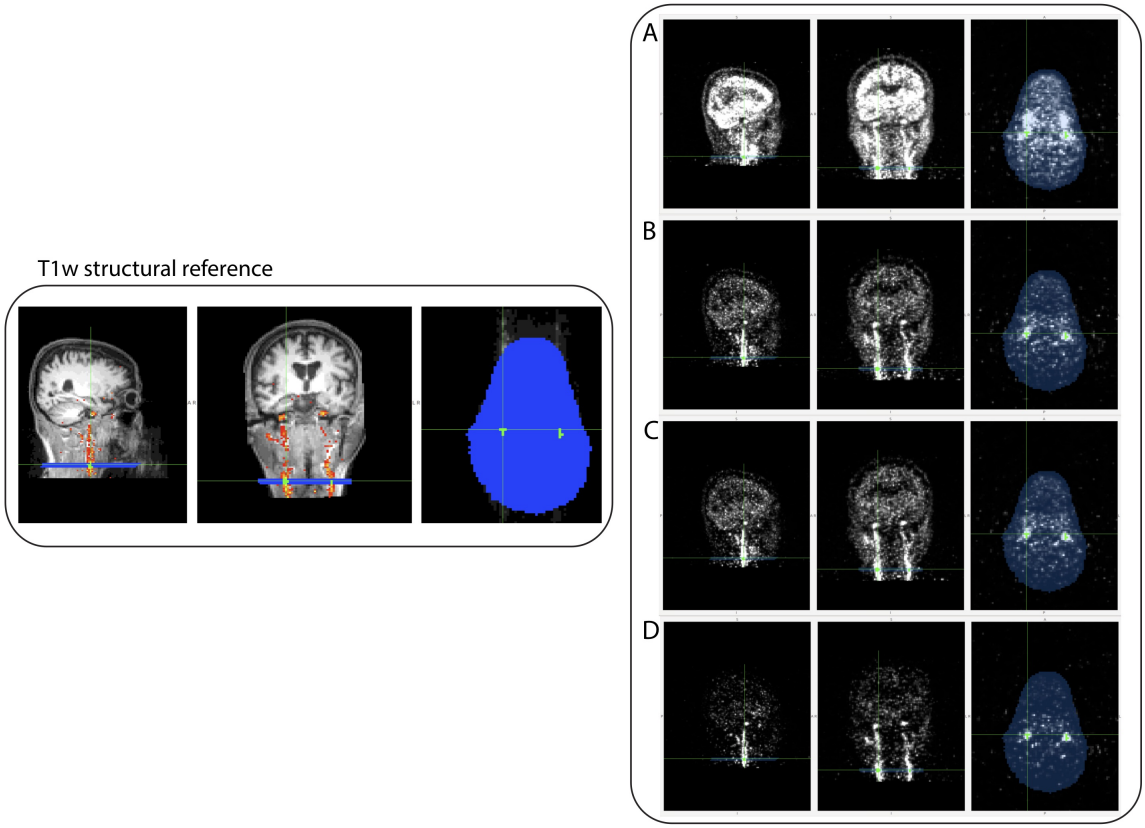

Figure 4.5: Contrast to noise ratio obtained for an Aβ-NEG patient reconstructing the PET data using the four time grid. On the left panel: the patient's MPRAGE (grey scale) with over-imposed the PET volume corresponding to the IDIF peak (red-yellow scale). In green and blue are respectively represented the two masks of the common carotids ROIs (CC) and the background ROI (BG). On the right panel: from A to D are depicted the PET volumes corresponding to the IDIF peak reconstructed using respectively the time grids *TG1*,*TG2*,*TG3*,*TG4*, normalized to one third of each peak amplitude intensity. In transparency are shown the CC and BG masks.

	CNR	ΔCNR	t_{peak}	A_{peak}
TG1	7.57	-	60	7.96
TG2	13.47	77.99%	30	9.84
TG3	13.80	82.42%	45	12.30
TG4	16.71	120.89%	35	24.80

Table 4.2: Contrast to noise ratio and IDIF characteristics obtained for one of the Aβ-NEG patients using the four proposed time grid *TG1*,*TG2*,*TG3*,*TG4*. CNR: contrast to noise ratio; ΔCNR: percentage difference between the *TG1* and the time grid in analysis; t_{peak}: time to IDIF peak (s); A_{peak}: IDIF peak amplitude (kBq/ml).

Early Phase PET Signal Quantification Results

The model that best described the *early phase* PET data was the one represented by equation 3.5, indeed in the 100% of the regions of interest of all patients it has been found to be the model for which the AIC reaches its minimum. Although the estimates were performed at ROI level the fact that the winner model was the model with the lower number of parameters (i.e. 1 parameter) could be due to poor signal to noise ratio of the extracted time activity, that is probably related to the low radiotracer dose employed during the study, and to the limited number of samples included in the time window on which the model were fitted.

The maps of the average ROI-wise influx rate constant obtained for Aβ-POS and Aβ-NEG groups are reported respectively in Figure 4.6(a) and Figure 4.6(b). The mean K_1 values in the grey matter are 0.31$\pm$0.05 $ml/g/min$ in Aβ positive group and 0.36$\pm$0.06 $ml/g/min$ in Aβ negative group. These results are in line with findings on ^{18}F-Flutemetamol reported literature both for healthy controls and for AD patients, though they tend to be on average higher than estimates achieved by Heurling and colleagues by fitting the ^{18}F-Flutemetamol dynamics using the 2TC model, namely 0.25$\pm$0.03 in HC 0.23$\pm$0.03 in AD patients (Heurling et al., 2015). From a purely qualitative perspective it can be said that the observed pattern of K_1 is compatible with a cerebral blood flow pattern in both groups. Indeed, the two maps assume higher values bilaterally in visual cortices, motor areas, posterior cingulate cortices and in subcortical nuclei (in agreement with CBF maps reported in (N. Zhang, M. L. Gordon, and Goldberg, 2017) and in (J. J. Chen, Rosas, and Salat, 2011) and obtained using the MR arterial spin labelling (ASL, (Haacke et al., 1999; Alsop et al., 2015)) technique. While lower values of K_1 can be distinguished in watershed areas (i.e. border zone regions supplied by the major cerebral arteries), this pattern is in line with major arterial district described by Tatu and colleagues (Tatu et al., 1999). Undoubtedly to quantitatively support those finding in spatial patterns, it could be very convenient a comparison with CBF maps simultaneously obtained for the same patient possibly using other techniques such as ASL or dynamic contrast enhanced (DCE) MR, nevertheless, due to time constrains, in this study it was not possible to add other sequence to the MR protocol.

The whole brain influx rate constant between the two groups was significantly different both in median and in dispersion (p-value lower than 10^{-6} in both cases), conversely no significant difference was found at ROI level. The absence of detected regional differences could be ascribed to the limited

cardinality of the groups.

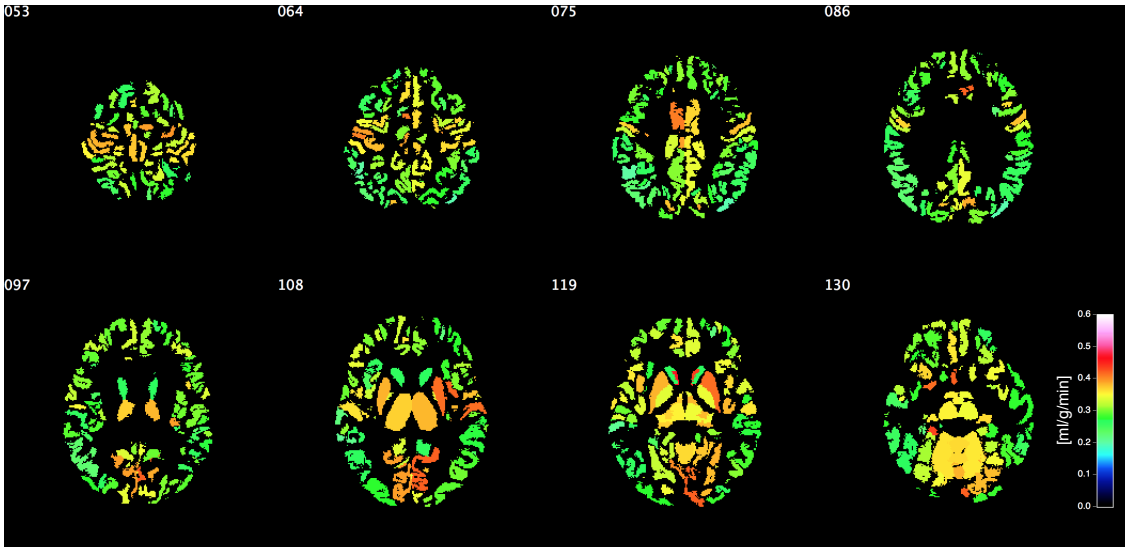

(a) Aβ positive group

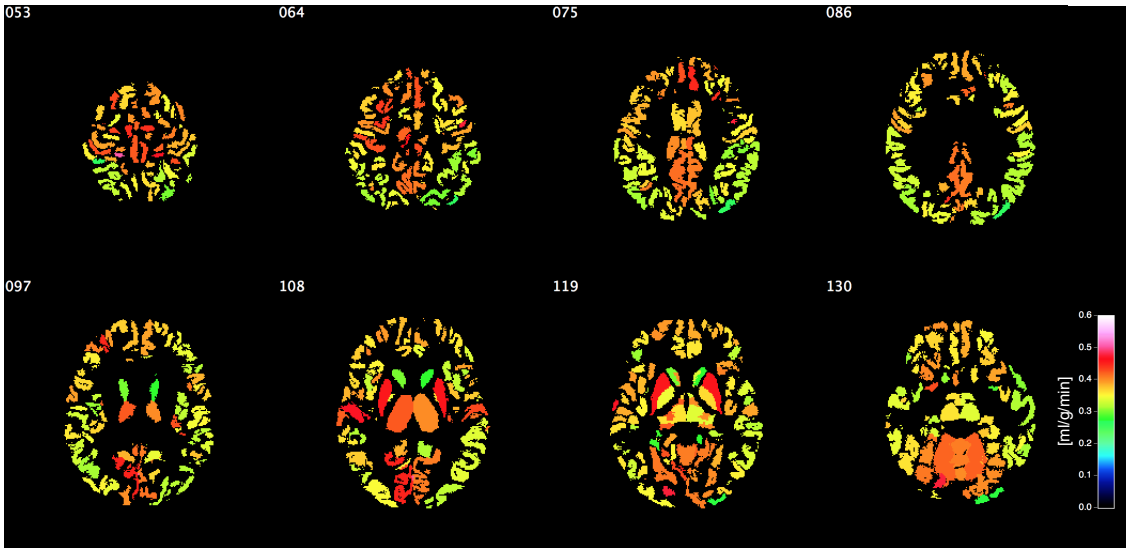

(b) Aβ negative group

Figure 4.6: Maps of average ROI-wise influx rate constant estimates (K_1)

βAmyloid Load PET Assessment Results

The maps of the average ROI-wise SUVR in the $A\beta$ positive and negative groups are shown respectively in Figure 4.7(a) and Figure 4.7(b). The derived global cortical SUVR values (1.64$\pm$0.26 g/ml in $A\beta$ positive group and 1.28$\pm$0.17 g/ml in $A\beta$ negative group) are in line with the SUVR values reported by (Mountz et al., 2015) for AD patients, where a positivity threshold was posed at 1.66 g/ml and with the results obtained by (Hatashita et al.,

2014), (N. Nelissen et al., 2009), and (Lowe et al., 2017).
The whole brain SUVR between the two groups was significantly different both in median and in dispersion (p-value $< 10^{-6}$ and p-value 0.025), and significant differences were also found at ROI level in all regions, when no multiple comparison correction was performed. Contrary to the influx rate constant results, the SUVR values had a low within-group variance, and probably this allowed to observe significant differences even in presence of a limited number of patients.

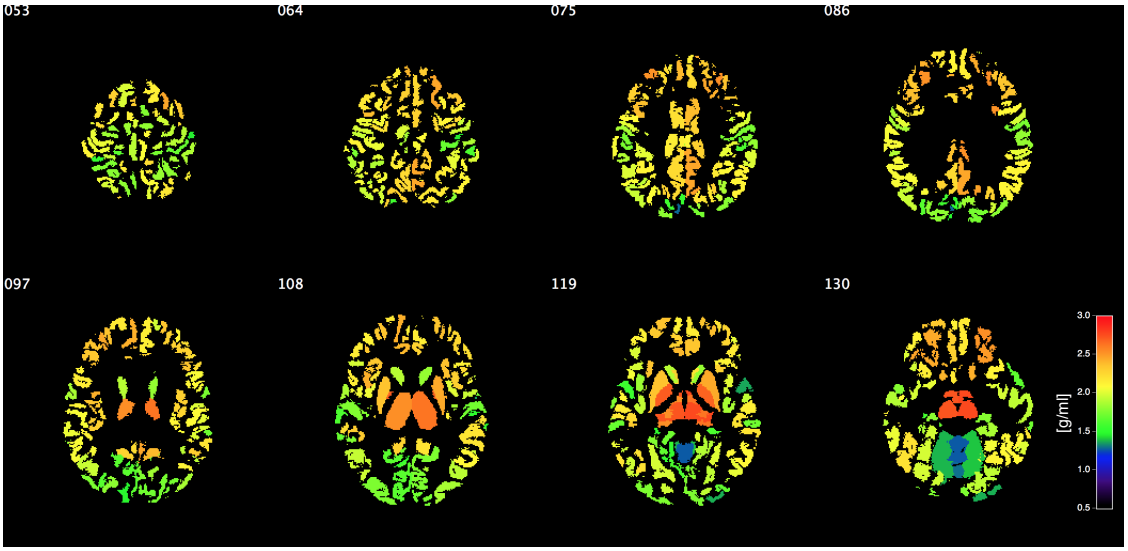

(a) Aβ positive group

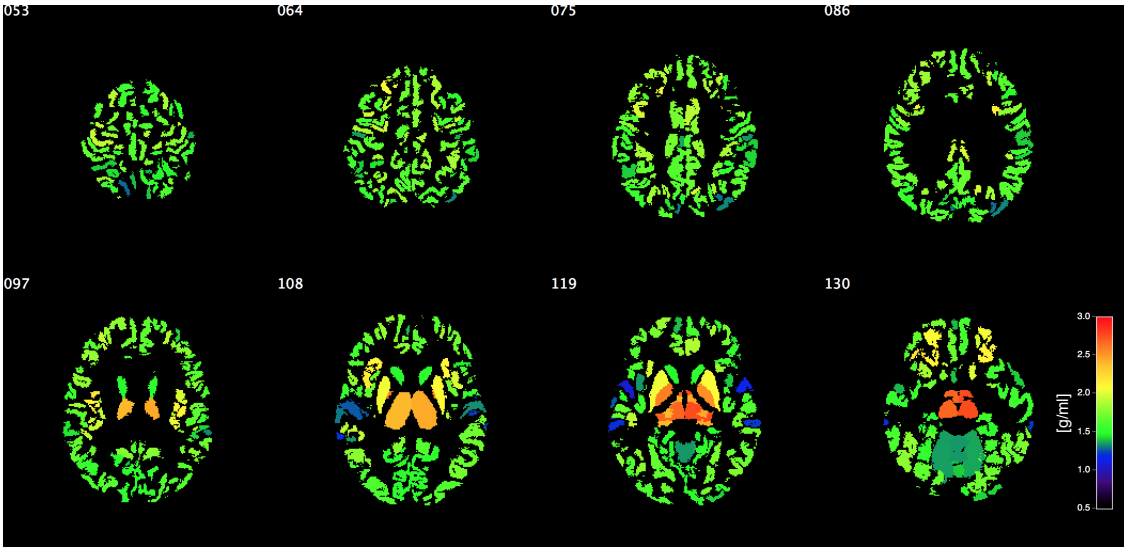

(b) Aβ negative group

Figure 4.7: Maps of average ROI-wise standard uptake value ratio

The regional relative changes in K_1 and SUVR between the two groups

are depicted in the map in Figure 4.8(a) and in Figure 4.8(b). K_1 relative changes ranged from -0.52 to 0.02 $ml/g/min$, with mean variation of -0.15 $ml/g/min$ and standard deviation amounting to 0.13 $ml/g/min$. Whereas SUVR relative changes ranged from -0.08 to 0.71 $ml/g/min$, with mean variation of 0.28 $ml/g/min$ and standard deviation amounting to 0.16 $ml/g/min$. Observing the map in Figure 4.8(a), no specific spatial pattern can be noticed. Conversely, SUVR relative changes have a well-defined spatial pattern that, considering the areas of high amyloid load increase, resembles the pattern of the resting state default mode network.

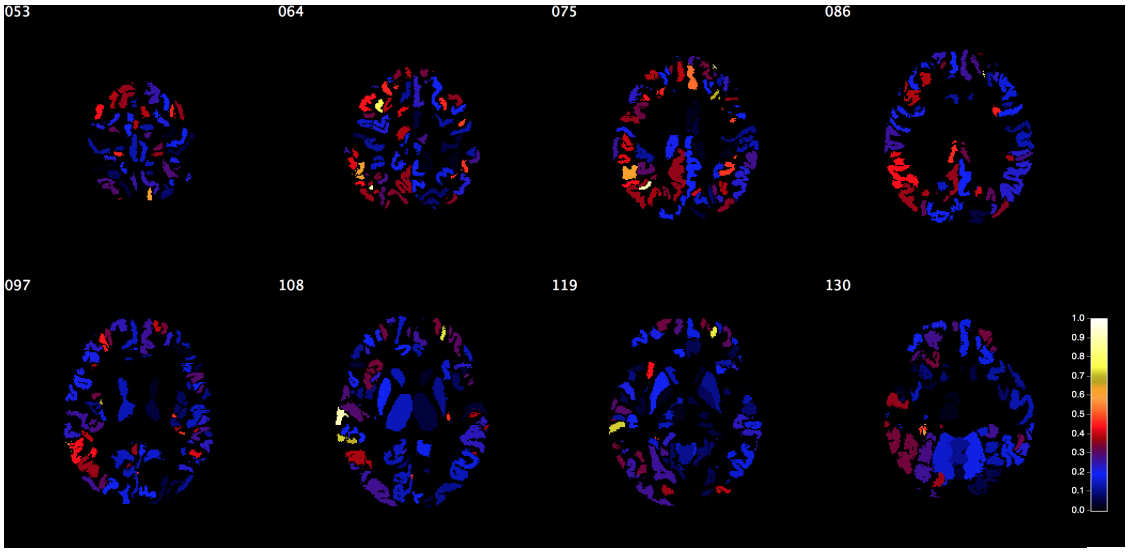

(a) Influx rate constant (K_1)

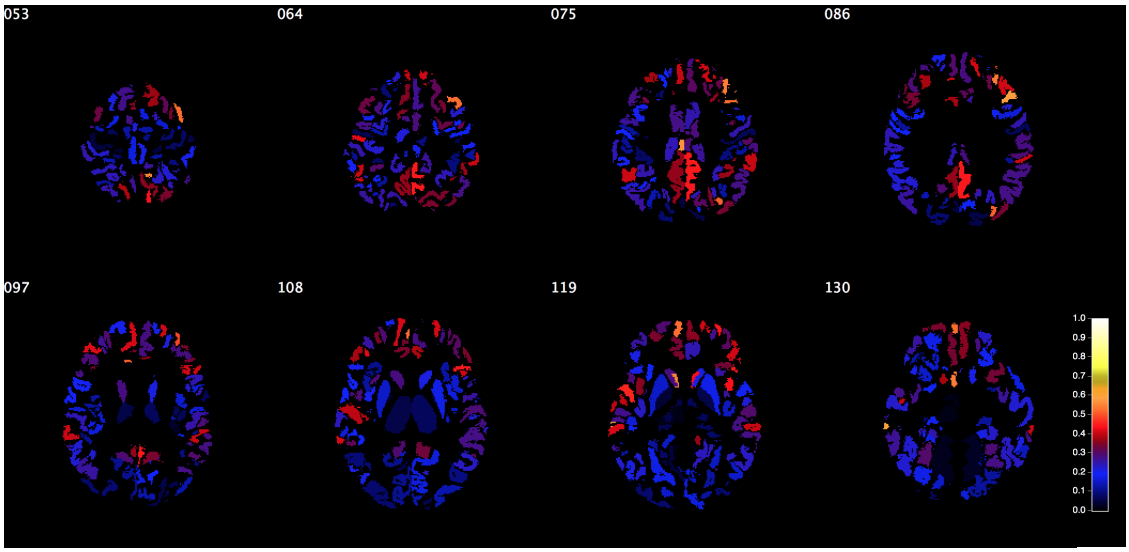

(b) SUVR

Figure 4.8: Maps of ROI-wise relative change between Aβ negative and Aβ positive groups

4.3.2 Connectivity Analysis Results

The average matrices of functional connectivity of the $A\beta$ positive and $A\beta$ negative groups are respectively shown in Figure 4.9(a) and Figure 4.9(b). In both maps the parcels have been reordered according to the resting state networks and the deep grey matter network. Observing the two matrices, therefore, it is possible to identify functional modules, such as the visual network or the default mode network. The RSNs modules pattern is in line with the pattern reported by Gordon and colleagues (E. M. Gordon et al., 2016), except for the two sensory-motor networks, this could be ascribed to the limited SNR of the sequence exploited during the resting state fMRI acquisition. The group average connection weights range from 0.10 to 0.86 for both $A\beta$ positive and $A\beta$ negative groups.
The results of the statistical analysis carried out on functional connectivity matrices and derived graph theory measures are listed in Table 4.3 and in columns two and three of Table 4.5.
In short, differences were found in within-network connection weights distribution at whole brain level and for the following resting state networks: cingulo-opercularis network, ventral attention network, dorsal attention network and fronto-parietal network. Moreover, the same networks and the default mode network resulted significantly different also in extra-network connection weights distribution. The connectivity matrices and connections distribution of VAN, DAN, and FPN are represented in Figure 4.10(a), Figure 4.10(b) and Figure4.10(c). Observing Figure 4.10, it could be noted that the intrinsic connectivity of these networks was on average significantly greater in the negative group than in the positive group. Although for some RSNs, such as the networks depicted in Figure 4.10, structural pattern differences was identifiable by visual inspection, no statistical difference were found in the related matrices structure. As the Krzanowski test is a permutation test, which in this case was implemented in the exact form, the absence of significant differences could be mainly attributed to the reduced dataset.
Furthermore, concerning graph theory measures, differences were found in betweenness centrality and local efficiency at whole brain level. Albeit not significant after multiple comparisons correction, all the considered DMN graph measures except node strength were found to differ between the groups.
Figures 4.11(a) and 4.11(b) show respectively the average matrices of struc-

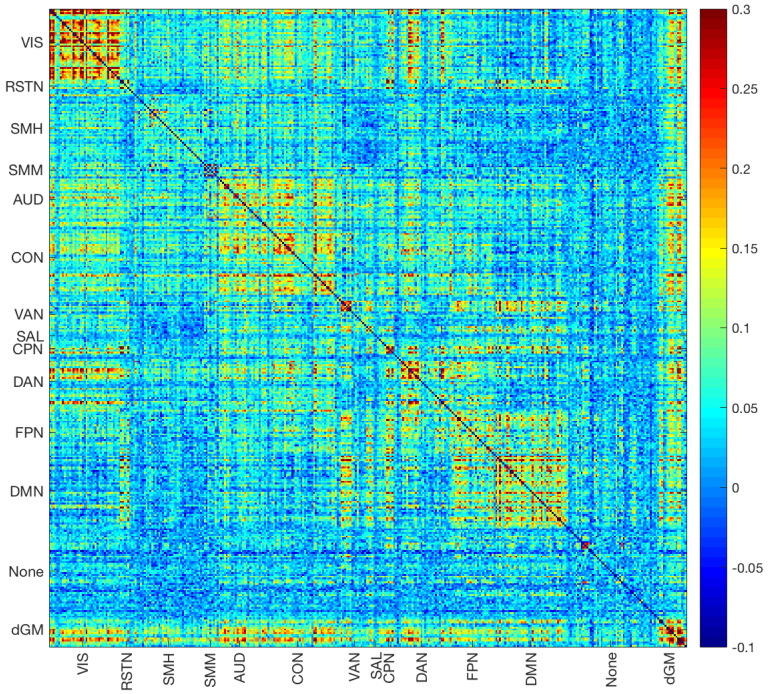

(a) Aβ positive group

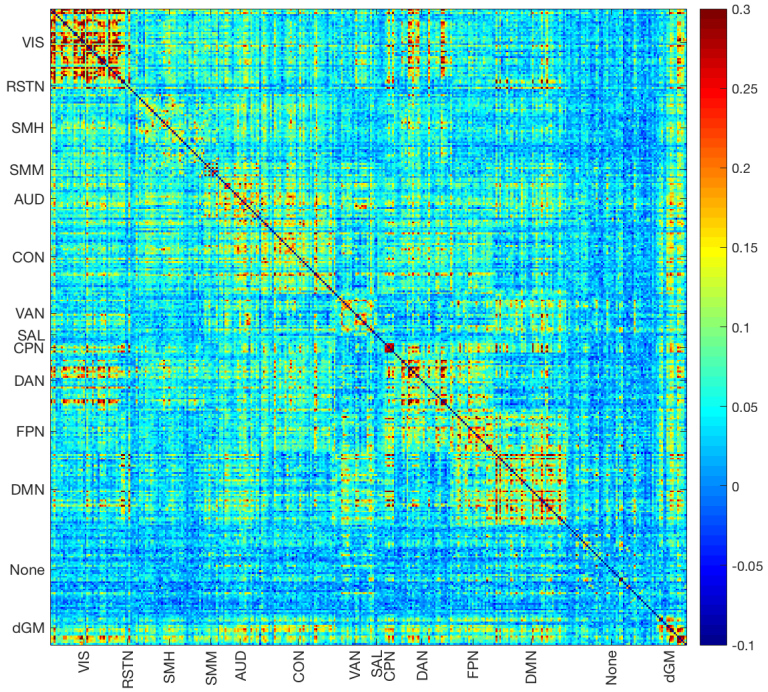

(b) Aβ negative group

Figure 4.9: Average functional connectivity matrices obtained for the two groups.

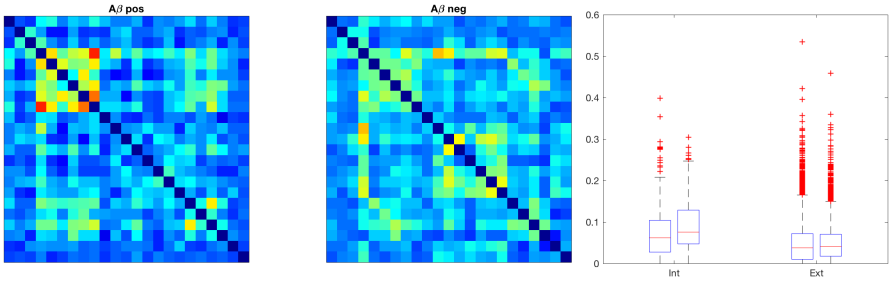

(a) Ventral-attention Network

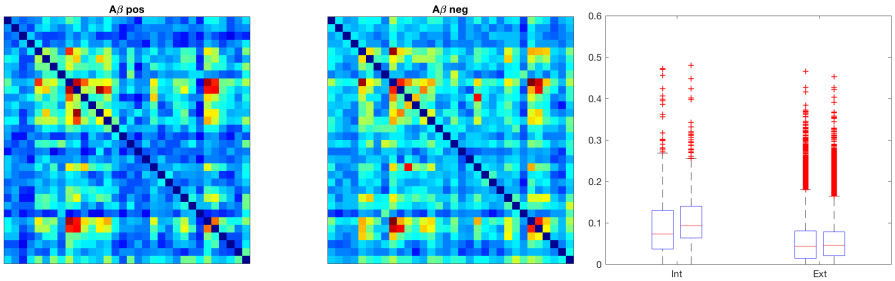

(b) Dorsal-attention Network

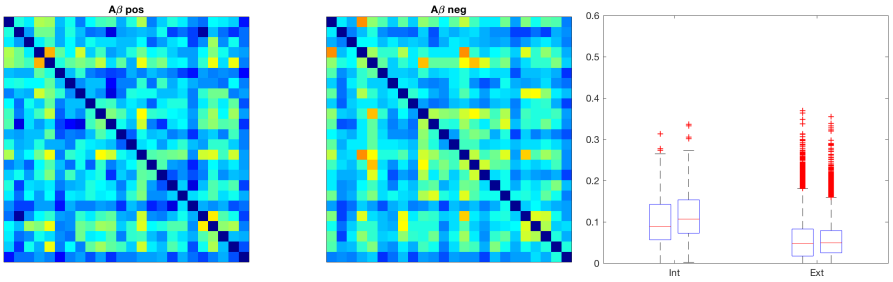

(c) Fronto-parietal Network

Figure 4.10: Resting state networks for which the intrinsic and extrinsic connection distributions resulted significantly different between Aβ negative and positive groups. The matrices on the two panels on the left represent the average RSN functional connectivity network respectively of Aβ positive and Aβ negative patients (links' weight ranges from -0.1 to 0.3). On the right panel: left hand side boxplot of intrinsic connection weights of Aβ positive (left) and Aβ negative (right), right hand side boxplot of extrinsic connection weights of Aβ positive (left) and Aβ negative (right).

Network	Distr.		Struct.	Graph Measures				
	median	dispersion		Deg	Str	BC	CC	EL
Whole Brain	✓	✓	-	-	-	✓	✓†	✓
VIS	-	-	-	-	-	-	-	-
RSTN	-	-	-	-	-	-	-	-
SMH	-	-	-	-	-	-	-	-
SMM	-	-	-	-	-	-	-	-
AUD	-	-	-	-	-	-	-	-
CON	✓	✓	-	-	-	-	-	-
VAN	✓	✓	-	-	-	-	-	-
SAL	-	-	-	-	-	-	-	-
CPN	-	-	-	-	-	-	-	-
DAN	✓	✓	-	-	-	-	-	-
FPN	✓	✓	-	-	-	-	-	-
DMN	-	-	-	✓†	-	✓†	✓†	✓†
dGM	-	-	-	-	-	-	-	-

Table 4.3: Summary of the results obtained with the statistical analysis carried out on the functional connectivity matrices (intrinsic connections) and the graph measures derived from them. Symbols ✓, ✓† and - stand respectively for significant difference after multiple comparison correction, significant difference when no multiple comparison correction is performed, and no statistical difference

tural connectivity of the $A\beta$ positive and $A\beta$ negative groups. As for functional connectivity, parcels were reordered according to the functional network. In this case, however, due to the choice of the connection weight measure, it was more difficult to identify the functional modules. Conversely, inter- and intra-hemispheric connections within and between networks were more evident, as intra-hemispheric connections commonly had weights higher (depicted in red-scaled colours in Figure 4.11(a) and Figure 4.11(b)) than inter-network. The group average connection weights ranged between 1 and 2.42 10^3 streamlines in the negative group, and from 1 to 3.15 10^4 streamlines in the negative group. The whole brain distribution of structural connection weights was significantly different between the groups both in median and in dispersion, and all the whole brain connectome-derived graph measures, except the betweenness centrality, were significantly different between the groups. The only network that, when no multiple comparison correction was performed, resulted to significantly differ between the two groups was the DMN. For this network we also found differences in clustering coefficient (p-value 0.01 uncorrected). All the structural connectivity statistical analysis results are listed in Table 4.4 and in column four and five of Table 4.5.

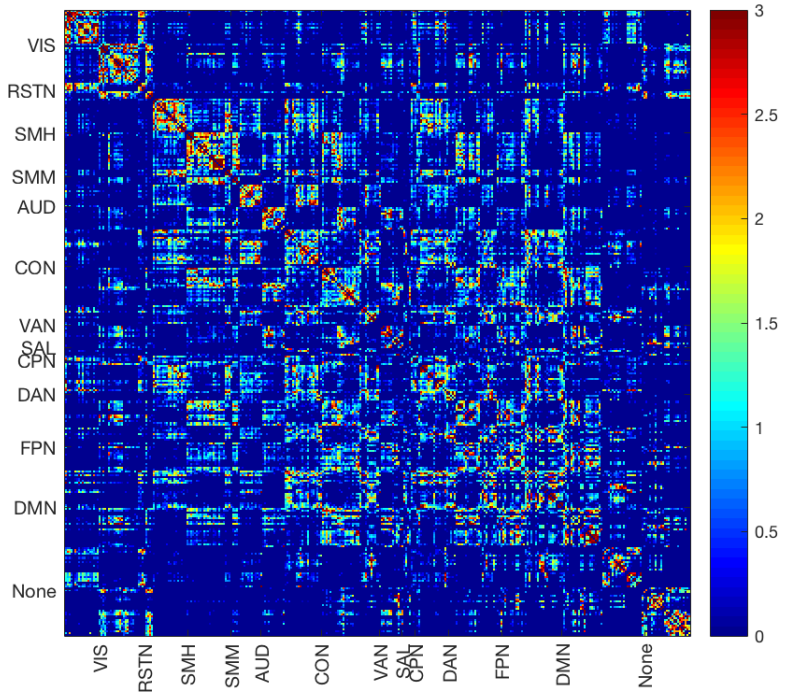

(a) Aβ positive group

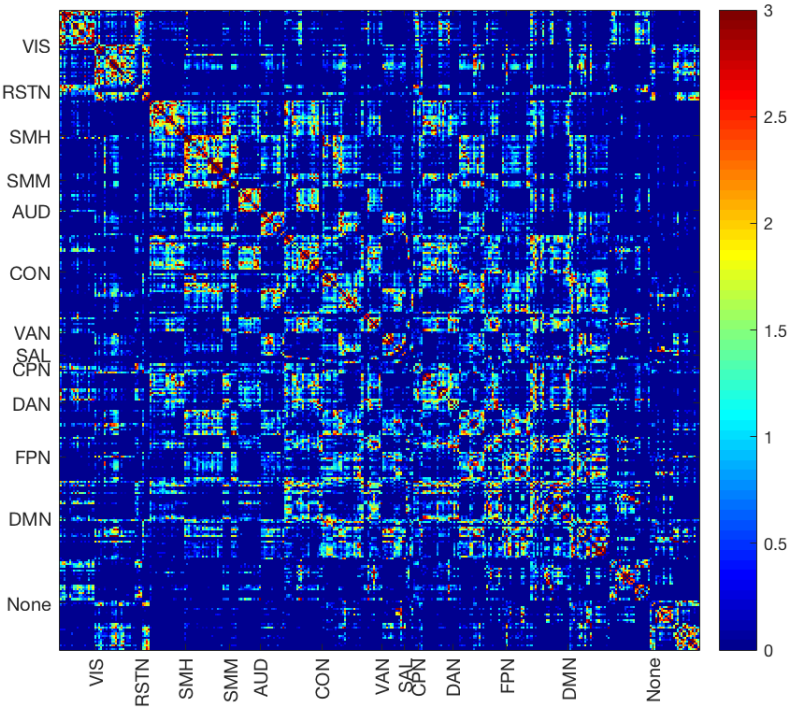

(b) Aβ negative group

Figure 4.11: Average structural connectivity matrices obtained for the two groups.

Network	Distr.		Struct.	Graph Measures				
	median	dispersion		Deg	Str	BC	CC	EL
Whole Brain	✓	✓	-	✓†	✓†	-	✓†	✓
VIS	-	-	-	-	-	-	-	-
RSTN	-	-	-	-	-	-	-	-
SMH	-	-	-	-	-	-	-	-
SMM	-	-	-	-	-	-	-	-
AUD	-	-	-	-	-	-	-	-
CON	-	-	-	-	-	-	-	-
VAN	-	-	-	-	-	-	-	-
SAL	-	-	-	-	-	-	-	-
CPN	-	-	-	-	-	-	-	-
DAN	-	-	-	-	-	-	-	-
FPN	-	-	-	-	-	-	-	-
DMN	✓†	✓†	-	-	-	-	✓†	-
dGM	-	-	-	-	-	-	-	-

Table 4.4: Summary of the results obtained with the statistical analysis carried out on the structural connectivity matrices (intrinsic connections) and the graph measures derived from them. Symbols ✓, ✓† and - stand respectively for significant difference after multiple comparison correction, significant difference when no multiple comparison correction is performed, and no statistical difference. **Distr.** and **Struct.** respectively refer to distribution of the link weights and connectivity matrix structure.

Network	Functional connectivity Distribution		Structural connectivity Distribution	
	median	dispersion	median	dispersion
VIS	-	-	-	-
RSTN	-	-	-	-
SMH	-	-	-	-
SMM	-	-	-	-
AUD	-	-	-	-
CON	✓	✓	-	-
VAN	✓	✓	-	-
SAL	-	-	-	-
CPN	-	-	-	-
DAN	✓	✓	-	-
FPN	✓	✓	-	-
DMN	✓	✓	✓†	✓†
dGM	-	-	-	-

Table 4.5: Summary of the results obtained with the statistical analysis carried out on extrinsic connections of functional and structural connectivity matrices. Symbols ✓, ✓† and - stand respectively for significant difference after multiple comparison correction, significant difference when no multiple comparison correction is performed, and no statistical difference.

4.3.3 Multimodal Integration Results

Correlation analyses between structural and functional network measures, and the PET-derived physiological features were carried out only at whole brain level and for the resting state network that we found to significantly differ between the two groups, namely VAN, FPN, DAN and DMN.

Albeit in an uncorrected for multiple comparison framework, changes in functional connectivity node strength, clustering coefficient and local efficiency significantly correlated with increase in amyloid load in $A\beta$ positive patients. The scatter-plots of the $\Delta SUVR$ versus ΔStr, ΔCC and ΔEL are represented in Figure 4.13, the obtained Pearson's correlations were respectively 0.46 (p-value 0.016), 0.50 (p-value 0.009) and 0.47 (p-value 0.012). Moreover, changes in node degree and strength were significantly related to the reduction of K_1 in the default mode network (respectively R=-0.33 p-value=0.036, R=-0.32 p-value 0.04), as reported in Figure 4.12.

Variations in structural-connectivity-derived graph measures were not significantly related either to amyloid load increase or to reduction of cerebral blood flow proxy.

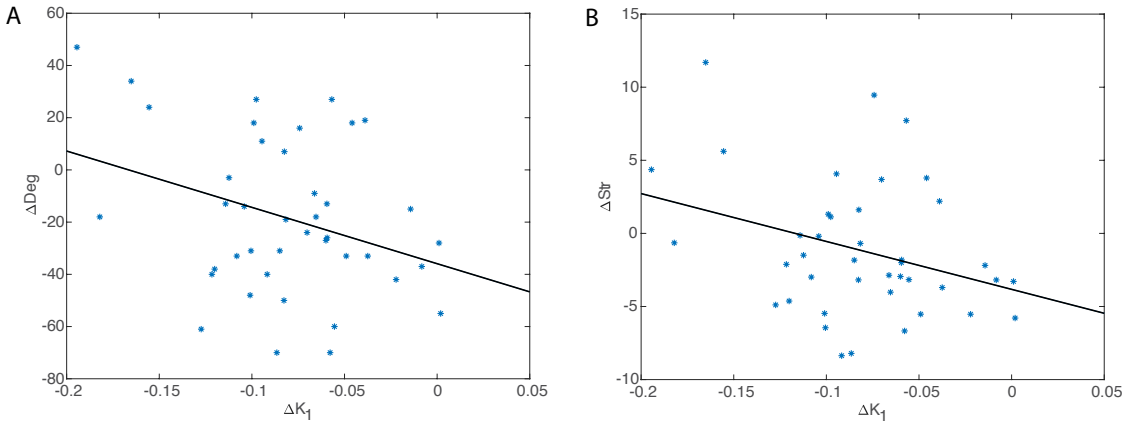

Figure 4.12: Scatter-plot of ROI-wise changes in K_1 versus changes in FC-derived graph measures obtained for the Default Mode Network. Panel A and B represent respectively changes in node degree (ΔDeg) and node strength (ΔStr). The black line in each scatter plot depict the linear fit of the data.

4.4 Conclusion

In this chapter the proof-of-concept application of the developed clinical framework to a dataset of patients affected by Parkinson's disease with concurrent cognitive impairment has been described. PD represent an interesting benchmark for the framework as the pathophysiological basis of the cognitive impairment and dementia in Parkinson disease is considered to be multifactorial with heterogeneous underlying pathophysiology and neuropsychological phenotype (Edison, Rowe, et al., 2008), hence, a multimodal approach to investigate this condition could potentially be very effective in understanding the causes and the progress of the disease (Monchi, Hanganu, and Bellec, 2016).

The analysis was mainly focused on connectivity alteration and how these could be related to changes in cerebral blood flow and to grey matter βamyloid burden. The comparisons were performed between two groups of PD patients, namely the Aβ-POS group that consist in patients that exhibit an altered grey matter pattern of amyloid load that is compatible with the pattern observed in Alzheimer's disease, and Aβ-NEG group for which no significant βamyloid burden was found.

The choice to refer changes in connectivity to perfusion and to βamyloid load was supported by literature findings. Indeed, in PD patients changes in connectivity has been proven to be related to cognitive impairment by several studies such as the one proposed by Peraza and colleagues where

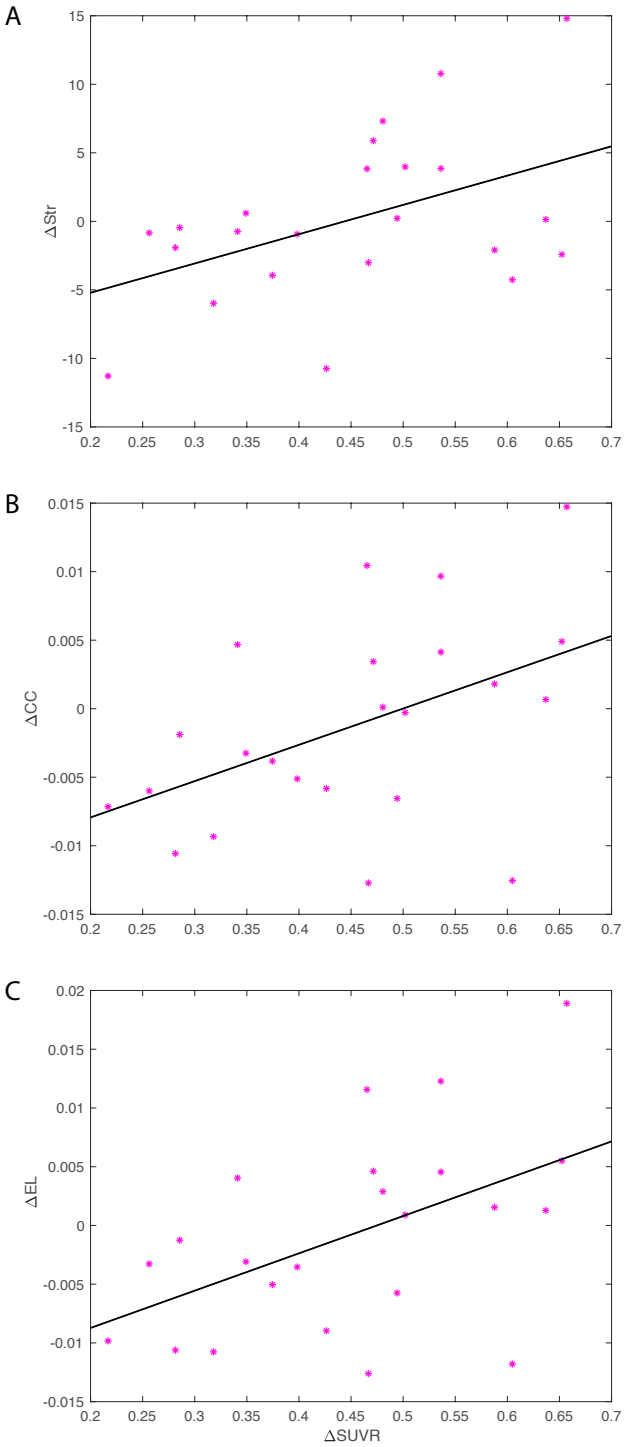

Figure 4.13: Scatter-plot of ROI-wise changes in SUVR versus changes in FC-derived graph measures obtained for the Ventral Attention Network. Panel A, B, C represent respectively changes in node strength (ΔStr), clustering coefficient (ΔCC) and local efficiency (Δ EL). The black line in each scatter plot depict the linear fit of the data.

lower functional connectivity or significant disconnection were found in cognitively impaired PD patients when compared with healthy controls (Peraza et al., 2015). Analogous results were obtained in DMN intrinsic connectivity by Zhan and colleagues (Zhan et al., 2018) and by Taylor and colleagues (Taylor, Kambeitz-Ilankovic, Gesierich, Simon-Vermot, Franzmeier, Araque Caballero, et al., 2016) and described for attention-related fronto-parietal RSN by Lopes and colleagues (Lopes et al., 2017). In addition, graph theory measures applied to resting state functional connectivity matrices were employed by Abòs and colleagues as robust features to discriminate PD patients cognitive status. Moreover, βamyloid burden has been observed in PD with concurrent dementia both in (Edison, Rowe, et al., 2008) and in (Hepp et al., 2016). The described pattern is similar to that recognized in AD patients and, according to (Gomperts et al., 2013), is related to cognitive decline and connectivity in PDD. The hypothesis that amyloid contributes to dementia initially came from the Alzheimer field, where excessive Aβ is viewed as an early, perhaps inciting, event in a cascade of pathologic changes leading to synaptic loss, neuronal degeneration, and clinical dementia and was then transposed in PDD. In particular that burden seems to affect the executive function networks (Gomperts et al., 2013; Campbell et al., 2015), i.e. the previously mentioned networks.

On the other hand, Rodell and colleagues identified perfusion as a factor that plays an important role in AD-related cognitive impairment (Rodell et al., 2017), more specifically a reduced cerebral blood flow was observed in patients affected by dementia, for these reason we search for a potential link between the pattern of decreased perfusion and the altered functional connectivity.

The proposed framework was able to produce satisfactory results in the clinical experimental setting. In particular, concerning the PET data it allowed us to go beyond the clinically common static analysis (i.e. SUV computation) and to assess, beside the amyloid load, a proxy of the cerebral blood flow. To note that at the time it was not possible to quantify the CBF in any other way as, due to limited scanner time, no other MR sequence such as dynamic susceptibility contrast could have been added to the protocol, and that using this approach it was not necessary to perform an additional contrast injection, with evident advantage for the patient. From literature it was clear the relationship between the influx rate constant (K_1) obtained through the compartmental modelling of the ^{11}C-PiB (a ^{18}F-Flutemetamol analogous) dynamic and the cerebral blood flow, however, to estimate a reliable proxy of

CBF from our dataset, two were the main problems that have to be faced: the absence of arterial samples to be used as model input function and the limited dynamic acquisition time window (i.e. 0-20min after injection). To solve the first problem it was decided to employ an image derived input function, while to address the second it was proposed to employ a reduced model to fit the dynamic PET data corresponding to the first 3min after the tracer injection. As for every signal, the capability to accurately extract the image derived input function is tightly related to the PET time framing reconstruction. Therefore, thanks to the developed wrapper that implement the off-line PET reconstruction, it was evaluated which was the best PET reconstruction time framing for the extraction of the IDIF in the present dataset. Although the injection duration shortness and variability, the selected time grid has led to a good CNR images that allowed us to easily drawn the pool of voxels ta be used for the IDIF extraction, and to consistent results among the group. Consistency was expected as it was hypothesised that the patients did not suffer from significant pathologies affecting the large vessels of the neck. In spite of these interesting and reproducible results, to rigorously validate our choices and entirely confirm the reliability of the obtained IDIF further data are needed. In particular, a direct comparison with the gold standard technique, i.e. arterial blood sampling, is required, however, at the time of the study these kind of data were not available.

Regarding the CBF proxy, estimates obtained using the model introduced in the previous chapter (i.e. 1TC-1k) are in line with the ^{18}F-Flutemetamol literature findings. Moreover, from a purely qualitative perspective, the spatial pattern of the quantified maps is compatible for both groups with the cerebral blood flow pattern known from physiology. One of the advantages offered by this type of approach if compared with the static approach such as the SUV computation proposed in (E. Rodriguez-Vieitez et al., 2016), is that beside the estimates of K_1 we also obtained the coefficient of variation of those estimates, i.e an index of reliability of the results. In particular, this index could be used to discard areas where the estimate process becomes critical or where the images' signal-to-noise ratio does not accomplish the model hypotheses and is not compatible with the model fitting, and where probably also the SUV value is not reliable.

The provided results as well as the finding in ^{11}C-PiB literature support the aptness of the proposed method, nonetheless, the absence of PET full dynamics and of arterial input function has prevented us from fully validating it. Indeed, although, as demonstrated in Chapter 3, the model structure has

proved to be adequate when applied to ^{11}C-PiB dynamics in the 0-3min time window, the appropriateness of this structure needs to be verified also for the ^{18}F-Flutemetamol. In addition, considering that the propagation of the input uncertainty to the estimates of kinetic parameters is a well know phenomenon, as clearly described in the work of Cheng and colleagues (Cheng and Yetik, 2011), it could be convenient to evaluate the impact of the use of IDIF instead of AIF on the compartmental modelling results.
Albeit the dataset limitations, the K_1 maps has shown to be able to detected significant differences between the two groups of patients. In particular, an evident decrease in perfusion has been found in the Aβ-POS group when compared with the Aβ-NEG group. This is in line with the findings reported in the AD literature, where a significant reduction in CBF were described by means of ASL techniques by Schuff and colleagues (Schuff et al., 2009) and by Binnewijzend and colleagues (Binnewijzend et al., 2013), and related to the βamyloid load by Mattsson and colleagues (Mattsson et al., 2014).
Considering the MR side of the study, fMRI and DTI sequences fine tuning has led to good data, in line with the research state-of-art requirements, as well as to reliable connectivity matrices that resembled literature known modularity pattern. For what concerns functional connectivity the two matrices exhibited a resting state networks modularity pattern that is mainly comparable with findings reported by Siegel and colleagues (J. S. Siegel et al., 2015) and by Gordon and colleagues (E. M. Gordon et al., 2016), where the same functional parcellation atlas was exploited. To note that, although from a whole brain point of view the match with the literature was good, the two sensory-motor network modules were found be less evident in our results (even in healthy controls, not reported here), this was ascribed to a limited MR-sequence-related tSNR of the cortical areas involved in those two networks. Concerning structural connectivity, the resulted matrices are in agreement with the reports of Hagmann and colleagues (Hagmann et al., 2008). It should be noted that, at the time this work of thesis started, this kinds of study were not feasible in the clinical setting of the Nuclear Medicine Unit of the University Hospital of Padova, as the multiband was not exploited and data were collected using only vendor sequences.
Finally, concerning the framework for the multimodal integration of features of pathophysiology and connectivity, albeit applied on this limited set of data, it has proved to be a promising tool to define the interplay between the neurodegenerative processes and the functional and structural altered connectivity.

Performing a multimodal integration based on an atlas-based approach (i.e. at ROI level) instead of voxel-wise analysis, allowed us to work with a better signal to noise ratio signals and to avoid the step of normalization of all the images to a common space, with clear advantages linked both to the fact that it was possible to work in the space of the single subject and of the single collected modality, and to the fact that the estimation of this transformation in subjects with evident atrophy such as the PDD patients can be particularly complex and accurate not very accurate.
At the same time, as suggested by Mijalkov and colleagues (Mijalkov et al., 2017), the use of graph metrics borrowed from the information theory has proved to be a particularly convenient tool to summarise nodal behaviour within the network. This way it was possible to directly compare PET and MR results, as for each ROI and for each modality we has only a single value provided by the analysis of that specific modality data.
What was found with this multimodal analysis was a significant correlation between the amyloid load and the changes in cognitive network, such as the VAN and DAN, that according to the literature are modified in Parkinson's disease when cognitive impairment is present (Gratwicke, Jahanshahi, and Foltynie, 2015; Peraza et al., 2015). In addition a significant correlation was found between the decrease in perfusion and the reduction in node degree and strength of DMN ROIs, which is in agreement with the studies conducted on AD patients, where DMN connectivity alteration were reported to be related to changes in perfusion of the involved areas (Lou et al., 2016).
Although, from a methodological point of view, this study has shown that the developed framework is appropriate for the integrated study of PDD connectivity, further data is needed to confirm the clinical value of the presented preliminary findings as well as the robustness of the proposed solutions. Increasing the number of patients in the study would not only increase the statistical power, but would also allows the inclusion in the statistical analysis of possible confounding factors, such as disease duration, time of conversion from MCI to dementia, age and APOE genotype. For this purpose further acquisitions are still ongoing.

Chapter 5

Connectivity Mapping to Guide Neuro-Surgery of Brain Tumours

5.1 Introduction

In this chapter is described and discussed a second proof-of-concept application of the proposed framework. The framework was employed for collecting, reconstructing and analysing images of a single patient suffering from high grade glioma, which is the most frequent type of primary tumours of the central nervous system in adults according to (Fernandes et al., 2017), and the most common and aggressive form of primary intracranial tumour (Ghinda et al., 2018).
Oncological field is probably the first and most common area of application of simultaneous PET/MRI acquisitions as they benefit of simultaneity from different perspective (Catana, 2017). Indeed, combining PET and MR has been proved to provide a better estimate of the tumour extent, a more accurate tumour grading, and to be a potentially efficient tools for therapy optimization (Miller-Thomas and Benzinger, 2017), as this approach leads to a more comprehensive picture of tumour and peritumoural tissues.
An accurate tumour grading could be achieved by means of integration of contrast MR imaging and metabolic imaging, especially for gliomas, as reported in (Pirotte et al., 2006). Indeed, high grade tumours are typically characterized by a high rate of glucose metabolism and increased ^{18}F-FDG uptake and a concurrent breakdown of the blood-brain barrier, that could be identified by MR contrast images and is typically associated with a poor prognosis, according to (Herholz, 2017).
In particular, the knowledge of the spatial pattern and extent of the tumour and of the altered morphology of the surrounding brain tissue may be a valuable tool for planning the therapy. Neurosurgical resection is the standard of care for gliomas and mounting evidence suggests that more extensive

surgical resection, which is typically based on FLAIR hyper-intensities and ^{18}F-FDG uptake, is associated with longer life expectancy for both low- and high-grade gliomas (Ghinda et al., 2018). The benefits of a radical resection in prolonging survival and facilitating adjuvant therapy need to be balanced against the risk of significantly altering the quality of life of the patients.
The multimodal approach represent a potentially useful tool in this respect, as merging physiological information quantified not only from PET and MR static data, but also from dynamic data could possibly allow to better distinguish tumour core region, necrosis, surrounding vasogenic oedema region, functionally altered or suffering regions and changes in the course of the white matter bundles (via diffusion tensor imaging). As suggested by Ghinda and colleagues (Ghinda et al., 2018), additional useful elements for planning the treatment can be provided by connectivity studies, that can for example highlighting regions where a residual activity persists and whose resection could negatively affect the patient's quality of life. At the same time a dynamic study of the most commonly employed PET tracer (i.e. ^{18}F-FDG) can provide further insight of the physiological processes that are taking place in this regions (i.e. perfusion and glucose oxidative phosphorylation).
The proposed framework was hence applied to those type of data to evaluate the feasibility of a ^{18}F-FDG quantitative dynamic study in the clinical setting of the Nuclear Department of the Padova University Hospital PET/MR scanner and to explore the opportunity offered by an integrated connectivity study approach in mapping peritumoural areas with residual activity that could potentially reveal useful in guiding the planing of the surgical resection.
The study was designed as a longitudinal study in which patients were imaged just before the surgery, after a month and three month later. Acquisitions were planned in order to follow changes both in connectivity and metabolism. Since at the time this thesis was written only the first time point of a single patient was acquired, in what follows are reported the preliminary results obtained on this first subject. Further acquisitions are ongoing.

5.2 Materials and Methods

5.2.1 Dataset

The framework of reconstruction and analysis was applied to the data collected in the first patient of the longitudinal study, a 37 years old male, suffering from high grade glioma located in the left frontal lobe. The same pipeline will be used to reconstruct and quantify the images of all the patients enrolled in this study. The acquisitions are still ongoing.
In particular, the available data are related to the first patient acquisition, before being subjected to surgical operation.

5.2.2 PET/MRI Brain Imaging Acquisition Protocol

Simultaneous PET/MRI scans were acquired at the Nuclear Medicine Unit, Department of Medicine – University Hospital of Padova, on a Siemens Biograph mMR (Siemens Medical Solutions USA, Inc.) equipped with a commercial PET transparent 16-channels head neck coil.
A 70min of ^{18}F-FDG positron emission tomography imaging was acquired, starting immediately before the radiopharmaceutical administration.
The MR brain imaging protocol included the following sequences:

- Ultra-short Time Echo (UTE), TR/TE1/TE2 11.9/0.07/2.46 ms, voxel dimension of 1.6x1.6x1.6 mm^3, FOV 300 mm, 192 slices
- Time-of-flight (TOF) MR angiography, TR/TE 24/4.16 ms, voxel dimension of 0.4x0.4x1 mm^3, FOV 200 mm, 96 slices (positioned at the level of the carotid arteries)
- 3D T1 Magnetization-Prepared Rapid Gradient-Echo (MPRAGE) TR/TE 2400/3.2 ms, voxel dimension of 1x1x1mm^3, FOV 256 mm, 160 slices
- 3D T2-weighted, TR/TE 3200/536ms, voxel dimension of 1x1x1mm^3, FOV 256 mm, 160 slices
- 3D T2-weighted Fluid Attenuated Inversion Recovery (FLAIR) TR/TE 5000/395 ms, voxel dimension of 1x1x1mm^3, FOV 250 mm, 160 slices
- Two Diffusion Tensor Imaging (DTI), SMS (CMRR, R014) 2, TR/TE 5255/104 ms, voxel dimension of 2x2x2mm^3, FOV 220 mm, 68 slices, 2 shell at b-value of 700 and 2855 (99 directions), AP and PA encoding direction respectively (~18min)

- Resting state functional MRI (fMRI) Echo-planar Imaging (EPI), SMS (CMRR, R014) 2, TR/TE 1260/30 ms, FA 68° (set by Ernst Criteria), voxel dimension of 3x3x3mm^3, FOV 204 mm, 40 slices, anterior-posterior (AP) phase encoding direction, 750 dynamic scan (~15min)
- Two fMRI geometrically matched spin echo (SE) EPI, two-fold acceleration with GRAPPA, SMS 1, AP and posterior-anterior (PA) phase encoding direction

Data were collected following the order of the previous list. To note that, as one of the interest of the study was to temporally match the metabolic consumption with the functional connectivity, the resting state fMRI was acquired at the end of the MR protocol in correspondence of the tail of the PET dynamics (i.e. when the tracer reached its steady state).
Concerning the PET protocol, a dose of 261 MBq (according to the patient's body mass index and glycaemia) of ^{18}F-FDG was administered by an intravenous bolus injection. As no MR-compatible injection pump was available, the radiotracer was manually intravenously administered . The injection and subsequent saline flush lasted less then 30 seconds. ^{18}F-FDG PET emission data were acquired in 3D list-mode format. As for the the study reported in the previous chapter, no arterial blood sample was collected because the facility that houses the PET/MRI scanner does not have an MR-compatible arterial sampling system.

5.2.3 PET Data Analysis

PET Images Reconstruction

PET images were reconstructed outside the scanner using the implemented in-house Matlab scripts that wrap the e7-tool reconstruction functions according to the pipeline described in Chapter 3. Therefore, firstly acquired sinogram was corrected for scatter, dead time and attenuation due to head and radio-frequency coil, then decay and normalization correction was performed, and finally the ordinary Poisson ordered subset expectation maximization (OP-OSEM) algorithm with 3 iterations and 21 subset was applied to the corrected sinogram to reconstruct PET images (matrix size 256x256x127, voxel size 2.8x2.8x2 mm^3). The μmap employed in the attenuation correction step was computed from the T1 MPRAGE using the (Izquierdo-Garcia et al., 2014) method. To avoid increasing partial volume effect, no further spatial

smoothing was applied to the obtained images.

PET Time Binning

As we were aimed at employing the compartmental modelling to describe the tracer kinetics within the tissues and no arterial sampling were available, also for this second application we employed an image derived input function as input for the model, therefore, PET dynamics were reconstructed at different time framing and it was selected the binning that allows a better identification and description of the image derived input function.
In contrast to what was found in the literature regarding the ^{18}F-Flutemetamol kinetic studies, where the number of papers is limited and the employed PET temporal binning is quite consistent among the studies, concerning the ^{18}F-FDG, the number of studies is much higher and the framing definitely less consistent (an example of the variability of the time binning used in ^{18}F-FDG dynamic reconstruction is reported in Table 5.1). For this reason it was not

References	Area	Time Binning
Bowen et al., 2013	HB	4x30s, 3x60s, 2x150s,2x300s, 4x600s
Christen et al., 2015	HM	12x10s, 4x120s, 10x300s
Hattori et al., 2004	HB	4x30s, 4x120s, 10x300s
Huisman et al., 2012	HB	6x10s, 2x30s, 3x60s, 2x150s, 2x300s,4x600s
Kawai et al., 2005	HB	1x40s,2x20s, 4x40s, 4x60s, 4x180s, 8x300s
Lucignani et al., 1993	HB	5x60s, 5x120s, 21x300s
Mosconi et al., 2007	HB	4x30s, 8x60s, 10x300s
O'Sullivan et al., 2010	HB	4x15s, 4x30s, 4x60s, 4x180s, 14x300s
Reivich et al., 1985	HB	10x180s, 1x300s
Sari et al., 2017	HB	6x10s, 2x30s, 3x60s, 2x150s, 2x300s,4x600s
Bertoldo et al., 2001	HM	12x15s, 4x30s, 3x60s, 1x120s, 22x300s

Table 5.1: List of some PET time framing reported in literature. HB stands for Human Brain, and HM for Human Muscle (thigh skeletal muscle).

possible to test each single time grid, conversely, it was decided to reduce the number of tests and to evaluate the performance of only two sampling grid. The first time grid (*TG1*) was the one exploited by Sari and colleagues (Sari et al., 2017) and was selected for two reasons: first, the obtained dynamic in that paper was exploited to extract the IDIF and is reported to perform properly, and, second, it was also used in other studies, such as the one of (Huisman

et al., 2012). The second time grid (*TG2*) was borrowed from studies performed by Bertoldo and colleagues with ^{15}O-H_2O (Bertoldo et al., 2001) and consisted in framing intervals of 10x6s, 8x15s, 7x60s and 2x1500s. The choice of this grid was driven by the necessity of having an higher number of samples during the first two minutes of the PET dynamic. Indeed, due to the duration of the radiopharmaceutical administration (less than $30s$) that was considerably sorter than the common injection duration, which typically lasts up to $2min$, a faster activity curve was expected for the current data. Since data were available for only one patient it was not possible to use consistency among the dataset to support the selection of the best performing time grid. In this case we preferred the time grid that, given the same pool of voxel within the two common carotids, led to higher values of IDIF peak amplitude and lower values of time to peak. The pool of voxels was derived directly from the PET images of the patient using a three step process: first, the TOF image mapped into the PET space was used to identify the voxels of the main neck vessels (i.e. the left and right common carotid) by means of a simple threshold (manually selected). Second, a subset of vessel voxel was selected using a hierarchical clustering approach (derived from the one proposed in (Peruzzo et al., 2011)) applied to the reconstructed dynamics of the vessel voxels. Finally, the IDIF was computed as the average dynamic of this subset.

To note that unlike what it has been proposed in the work of Sari and colleagues (Sari et al., 2017) where TOF and PET data were acquired in two separate systems, it has been choose to use the signal of neck large vessels (i.e. the common carotids, that in our case were included in the PET camera field of view) to reduce the partial volume effect and increase the reliability of the estimates, as suggested in (Zanotti-Fregonara et al., 2011).

In what follows the dynamic PET images reconstructed using the most appropriate time grid for IDIF extraction is named as $dynPET_{IDIF}$.

Once the best performing grid was selected, as the compartmental modelling hypothesis is that the arterial input is not affected by noise, the extracted dynamic has been fitted using the tree-exponential model as proposed by Feng and colleagues (Feng, Huang, and X. Wang, 1993). As for the previous study, the time to peak and peak amplitude were fixed in order to reduce the number of model's parameters that would have been estimated.

Given the speed of intravenous injection, the three exponential model proved to be adequate to our data, so no more complex modelling, such as the one proposed in (Tonietto, Rizzo, Veronese, and Bertoldo, 2015) in which also the

injection duration is modelled, was required.
In addition to IDIF devoted framing, PET data were reconstructed employing a second time binning ($dynPET_{FIT}$) with framing intervals of 8x30s, 8x60s and 12x240s. As the reliability of the model estimates depends on the signal to noise ratio of the voxel/region activity signal, we adopted this second time grid in which the sampling step, especially for the first frames, was longer than the previous one in order to increase the count statistics. The time grid was in agreement the majority of the framing reported in Table 5.1. The signal sampled using this second time grid was employed as tissue tracer concentration to estimate the kinetic parameters with the compartmental modelling.
Finally, a static image was reconstructed, i.e. a single frame was obtained by the integration of the event counts in the time windows comprised between 40 and 60 minutes after the tracer injection. This last image was mainly produced for clinical purpose.

PET Images Preprocessing

The goal of the analysis was to integrate the different informations coming from PET and MRI data analysis to identify tissues were residual activity was still present despite the presence of the tumour. To do so, it was necessary to take into account that the tumoural mass significantly altered the geometry and the spatial pattern of the brain tissue. Thus, in contrast to the approach carried out in the previous study, PET analysis was performed at voxel level and then the results were mapped in the subject's structura image space. For comparison purposes, we also necessary to perform a tissue segmentation (i.e. WM, GM and CSF) and tumour delineation, as we will discuss later in this chapter these two steps were carried out on the T1w MPRAGE image.
Segmentations were then mapped into the PET space. For this patient, the mapping was simply performed applying the affine transformation from MR to PET reference system that is always estimated by the scanner. In general, it is important to verify the efficiency of this step because if during the acquisition patients moves a lot, this transform is not accurate and the following coregistation results in a not negligible mismatch between MR and PET images.
Exploiting the scanner transform also the TOF angiography was registered into the PET, in order to be used as guide to extract the IDIF, as suggested in (Fung and Richard E. Carson, 2013) and in (Sari et al., 2017).
Finally, taking advantage of the EPI (resting state fMRI and DTI) acquisitions, it was possible to verify that there were no large movements of the patient

head during the scan, if related to the PET scanner spatial resolution (i.e. 4.3 mm, as reported in (G. Delso, Furst, et al., 2011)), and thus, it was decided not to perform any motion correction step.

PET Modelling and Quantification of Tissue Metabolic Activity

The ^{18}F-FDG PET data modelling and quantification of the tissue metabolic activity was carried out using a compartmental modelling approach.
No model selection was required as the optimal compartmental model for the description of the ^{18}F-FDG dynamics within the brain tissues has been known for several decades, since it was developed by Sokoloff in 1977 (Sokoloff et al., 1977) for autoradiographic ^{14}C-deoxyglucose (^{14}C-DG) method in rat brain and subsequently modified for ^{18}F-FDG human applications by Phelps and colleagues (Phelps et al., 1979) and by Schmidt and colleagues (K. Schmidt et al., 1992). It is a 2 compartment and 3-rate-constant (2TC-3k) model.
The model structure and the related differential equation are reported respectively in Figure 5.1 and Equation 5.1:

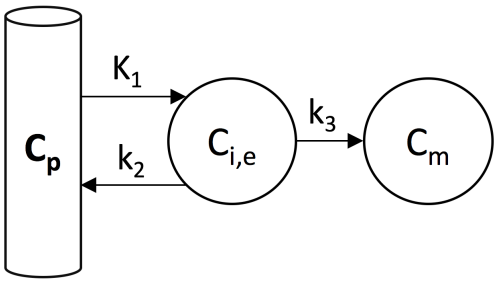

Figure 5.1: Structure of the 2TC-3k model for measuring the metabolic rate of glucose with ^{18}F-FDG (adapted from (Sokoloff et al., 1977)). C_P, arterial plasma ^{18}F-FDG concentration; $C_{i,e}$, tracer interstitial and intracellular concentration; C_m, ^{18}F-FDG 6-phosphate intracellular concentration; K_1 and k_2, ^{18}F-FDG transport from plasma to interstitial-intracellular space and back, respectively; k_3, ^{18}F-FDG phosphorylation

$$\begin{cases} \frac{dC_{i,e}(t)}{dt} = K_1 C_P(t) + (k_2 + k_3) C_{i,e}(t) & C_{i,e}(0) = 0 \\ \frac{dC_m(t)}{dt} = k_3 C_{i,e}(t) & C_m(0) = 0 \\ C_T(t) = (1 - V_b)(C_{i,e}(t) + C_m(t)) + V_b C_b(t) & \end{cases} \tag{5.1}$$

where C_P represents the arterial plasma ^{18}F-FDG concentration; $C_{i,e}$, the tracer interstitial and intracellular concentration; C_m, the ^{18}F-FDG 6-phosphate intracellular concentration; C_T represents the total activity concentration within the voxel; $C_b(t)$, the arterial blood tracer concentration; K_1 $(ml/cm^3/min)$

and k_2 $(1/min)$, the ^{18}F-FDG transport from plasma to interstitial-intracellular space and back, respectively; k_3 $(1/min)$, the ^{18}F-FDG phosphorylation; and finally V_b is the fraction of the total volume (i.e. voxel) occupied by blood pool (K. C. Schmidt and F E Turkheimer, 2002).
The model prediction of the fitted image derived input function was employed as nose-free arterial input of the model. The presence of radiometabolites do not affect the ^{18}F-FDG tracer (Zanotti-Fregonara et al., 2011), therefore, no additional hypothesis or processing was required.
The compartmental model parameters were estimated at voxel level using the weighted non-linear least square approach applied to the $dynPET_{FIT}$ voxel dynamic reconstruction. Weights were chosen optimally as:

$$w(t_i) = \frac{\Delta t_i}{C_{voxel}(t_i)} \tag{5.2}$$

where t_i is the time instant, Δt_i is the length of the scanning interval and $C_{voxel}(t_i)$ is the voxel emission activity at time t_i (as suggested in (E. Carson, Cobelli, and Finkelstein, 1983)). Finally, during the fitting, the $C_b(t)$ was supposed to be equal to the $C_P(t)$, i.e. negligible tracer uptake of the red-blood cell. This an implicit assumption in the use of IDIF that was validated for ^{18}F-FDG in a previous study by Gambhir and colleagues for the 120min time period (Gambhir et al., 1989).
In order to verify the reliability of the estimated parameters, those findings were compared with literature results. The comparison was carried out limiting the analysis to the grey matter far from the diffuse oedema in the tumour contra-lateral hemisphere. The average of each model parameter was computed over this selected area. To note that only reliable estimates were comprised in the testing, namely estimates with sufficient precision (CV < 100%) and physiologically plausible (K_1,k_2,k_3 >0, and V_b ranging form 0 to 1).

5.2.4 MRI Data Analysis

Anatomical Images Preprocessing

The extent of the tumour in this patient caused a significant alteration of the brain morphology, for this reason it was not possible to perform either an advanced preprocessing, such as the surface mapping, or a fine parcellation of the structural images such as the one proposed by Gordon and colleagues.

But rather, the anatomical images preprocessing consisted only in a manual tumour delineation and in a basic tissue segmentation.
The tumour extent was delineate by an expert physician using the FLAIR as well as the T2w image. While the tissue segmentation of the T1 MPRAGE image was performed using the Advanced Normalization Tools software (ANTs). Briefly, the image was corrected for bias field inhomogeneity and then segmented into white matter, grey matter, cerebrospinal liquid, deep grey matter, cerebellum, and brain stem using the probabilistic tissue segmentation implemented in the ANTs *Atropos* tool. Moreover, to discriminate between left and right hemisphere the MICCAI2012 atlas parcellation was performed, as described in the previous chapter.

Functional Connectivity Analysis

The goal of functional connectivity analysis was to characterized the resting state networks (RSNs) of the patients. In particular, the interest was in identifying possible functional alteration of those networks, that could be related to the presence of the tumour, and RSN regions where no appreciable change was detectable. Due to the significant impact of the tumour on the brain anatomy, to study the RSN it was decided to employ a data-driven approach instead of an atlas-based approach. This choice was made because we were aware of the limited efficiency of the parcellation process in case of significant morphological deformations.

Resting State fMRI Data Preprocessing The resting state acquisition of the patient was preprocessed in the individual space using a combination of ANTs software and FMRIB Software Library (FSL, S. M. Smith, Jenkinson, et al., 2004).
Functional images were corrected for readout distortion, using the two SE images and the FSL's TOPUP algorithm (J. L. R. Andersson, Skare, and Ashburner, 2003). Data were then corrected for head motion with ANTs' *antsMotionCorr*, specifically, a 12-degree of freedom affine transformation was estimated to realign each volume to the single-band acquired volume.
To compare functional results with the feature extracted with the other imaging technique, it was necessary to map the fMRI space to the T1 MPRAGE space. The functional images were spatially normalized to the single subject MPRAGE in a two-step process: first, to single-band reference volume was registered to the T2w image using an affine transform and an additional diffeomorphic deformation field limited to the anterior-posterior direction;

then, the T2w image was rigidly registered to T1w. The estimated displacement fields and affine matrices were combined into a single concatenated transformation, which mapped fMRI space into the MPRAGE reference system; this transformation was then used to move the RSNs maps obtained in the fMRI space to the MPRAGE space with a single interpolation step.

Resting State Networks The resting-state connectivity pattern was inferred from the preprocessed patient fMRI data using the independent component analysis (ICA) technique. This is one of the most widely used techniques in the study of functional connectivity (Fox, 2010). Briefly, ICA is a multivariate voxel-based approach that considers all voxels dynamic at once and performs a dataset separation into distinct systems or networks that are correlated in their spontaneous fluctuations but also maximally independent in the spatial domain.
For this analysis the FSL's Multivariate Exploratory Linear Optimized Decomposition into Independent Components (MELODIC) software was employed. A relatively high number of independent component (IC) was chosen, i.e. 100 components, according to what was proposed by Allen and colleagues (Allen et al., 2012). Resting state components were then manually identified, the selection was made on the basis of the IC source time dynamics and frequency behaviour, and of the IC spatial pattern. In particular, components were marked as artefactual when either IC spatial pattern mainly overlapped structures of non interest or vascular structure such as the superior sagittal sinus, or IC frequency content was principally confined in the high frequencies (i.e. in a frequency range higher than $0.1Hz$).
Thanks to the high number of IC, the main resting state networks were clearly identified, i.e. the default mode network (DMN), the visual network, the auditory network, executive control, etc, and the signal noise content discarded. Nonetheless, we mainly focused of the DMN because its spatial pattern was heavily affected by the presence of the tumour and has been found to fall in FLAIR areas of altered signal that would have been potentially considered completely compromised.

Structural Connectivity Analysis

The white matter projections linking cortical and subcortical regions are typically altered in presence of large tumour, in particular, some fibres are interrupted and others changes their path (Potgieser et al., 2014). Changes in

the major tracts can be delineated using the so-called tractography or fibre-tracking algorithms.
Being able to follow the direction of the bundles allows us to give a description not only of the structure itself, but also of the reliability of the observed residual activity and connectivity. The idea was to test whether there were a residual or undamaged structural connectivity that underpinned the functional links recognised with the fMRI analysis. For this reason, the study of structural connectivity on this patient did not focus on the entire brain but rather was focused on the connectivity between the nodes of the identified functional networks, and, in particular to the default mode network.
To note that the use of RSN maps derived directly from the patient avoids the problem of having to match the altered anatomy of the patient with that of different resting state network templates present in the literature and allowed us to work with subject specific data driven maps.

DTI MR Data Processing Diffusion MR data processing was performed using the MRtrix3 software (http://www.mrtrix.org).
As previously mentioned, patient head motion during acquisition is a major challenge for diffusion imaging data, therefore for the patient's DTI data a manual data checking was performed to ensure motion-corrupted volumes were identified and discarded, a step that works like the data censoring in fMRI. The number of not discarded volumes was higher than 60, hence, it was possible to proceed the analysis.
Data preprocessing was then executed using the *dwidenoise* and *dwipreproc* scripts. The *dwidenoise* was applied both to blip up and down DTI acquisition (i.e. AP and PA acquisition of the same weighting gradient direction). It improves the SNR of the diffusion data reducing the effect of thermal noise, and exploits data redundancy in the PCA domain using the prior knowledge that the eigenspectrum of random covariance matrices is described by the universal Marchenko Pastur distribution (Veraart et al., 2016). This *dwipreproc* script then execute the actual preprocessing of diffusion image data and includes eddy current-induced distortion correction, motion correction (i.e. realignment of volumes), and susceptibility-induced distortion correction (using the two acquired encoding directions of each gradient direction and the FSL's TOPUP tool) (J. L. R. Andersson, Skare, and Ashburner, 2003; J. L. Andersson and Sotiropoulos, 2016; S. M. Smith, Jenkinson, et al., 2004).

The multi-shell constrained spherical deconvolution as reported in (Jeurissen et al., 2014) and implemented in the MRTrix3 software was used to compute the fibre orientation density function (FOD). From the estimated FOD the 5-millions-streamlines tractogram was computed using the probabilistic fibre-tracking algorithm implemented by default in MRTrix3 with the option anatomically-constrained tractography (ACT, R. E. Smith et al., 2012) turned on and the minimum-length constrain set at 4 mm. In short, the algorithm identifies suitable position from which to initiate the streamline (the seed point), propagates the track along the estimated fibre orientation, and terminates the track when appropriate termination criteria are met. ACT causes streamlines only to terminate precisely at the grey matter - white matter interface, within sub-cortical grey matter, or at the inferior edge of the image. Whereas minimum-length criterion essentially acts as a noise filter, removing short spurious tracks for which the support is poor given the diffusion image data. Moreover, in order to improve the quantitative nature of whole-brain streamlines reconstructions the spherical-deconvolution informed filtering of Tractograms (SIFT, R. E. Smith et al., 2013) was applied to the obtained tractogram. This approach carry out a track pruning based on the FOD, which in our case resulted in a 2.5-million-streamlines tractogram.

Resting State Network Structural connectivity In order to analyse the connectivity between regions among the same RSN, the maps of the main RSNs were mapped into the DTI space and used as seeds to restrict the tractogram to the bundles just originating from the nodes of the specific network (i.e. seed based approach), using the MRtrix3 *tckedit* script.

5.3 Preliminary Results

In this session the preliminary results obtained for the first patient of this study are reported and briefly discussed. The report will follow the Material and Methods session order. We will firstly show and discuss results obtained from the ^{18}F-FDG PET data, then the resting state network functional and structural connectivity will be described and and finally some results of the multimodal integration will be shown.

5.3.1 PET Data Analysis Results

As regard the optimal time binning for the image derived input function, the *TG2* framing has resulted to be the best as, given the same pool of voxels dynamics identified by means of the TOF image, it has led to a lower time to peak and higher peak amplitude value. In particular, the time to peaks obtained for $TG1$ and $TG2$ were respectively of 55s and 51s, and the peak amplitudes respectively of 40.6kBq/ml and 64.4kBq/ml (with a percentage increase of 37.2%). The IDIF dynamics achieved using the two time grids, limited to the first 5min, are depicted in Figure 5.2. From the figure it is clear how the second framing leads to a less disperse IDIF, with an full width at half maximum (FWHM) that decrease from 31.2s of $TG1$ to 9.5s of $TG2$.
The complete ^{18}F-FDG image derived input function obtained from $dynPET_{IDIF}$

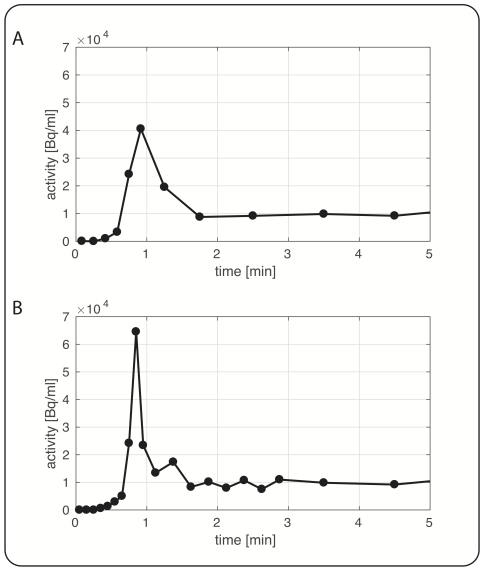

Figure 5.2: Image derived input functions obtained reconstructing the PET volumes using the $TG1$ time binning (panel A) and the $TG2$ time binning (panel B).

data as well as the Feng model prediction are reported in panel A of Figure 5.3. In the same figure, it is also depicted an example of arterial sampling obtained for a ^{18}F-FDG study (described in (Bertoldo et al., 2001)) where intravenous injection lasted 2min, instead of the 30s of the present study. Looking at the two curves it can be clearly perceived how injection period influences the input function shape and why in this study the Feng model was considered to be sufficiently reasonable to fit the extracted IDIF dynamic. Indeed, the Feng model was aimed at describing the impulse response function of the circulatory system (Feng, Huang, and X. Wang, 1993).

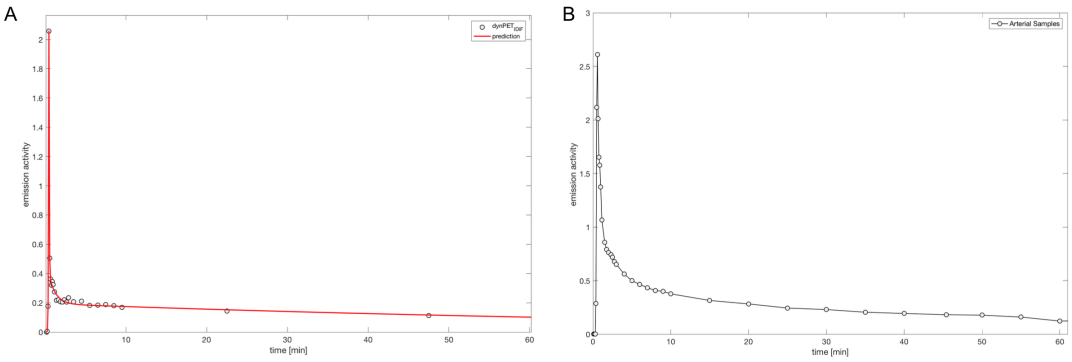

Figure 5.3: Image derived input function: panel A, normalised patient's IDIF (grey dots) and Feng model prediction (red line) (intravenous injection duration: $30s$); panel B, normalized arterial sampling input function obtained in a study where the intravenous injection lasted $2min$. To note that for both the time activity curves the peak amplitude was employed for normalization purpose.

The parametric maps of the model estimates are reported for eight representative slices in Figure 5.4 and 5.5. The needed of two different figures is due to the extent of the tumour. The maps show a significant hypo-metabolism (K_3 and K_i maps) and hypo-perfusion (K_1) both in the tumoural and in the peritumoural area, that suggest a diffuse suffering also in the surrounding tissues. From a purely qualitative point of view, it could be said that the observed pattern seems to be closely related to the oedema pattern depicted in FLAIR image (first row of the image), even if there are areas where a the FLAIR signal is altered but this corresponds neither to appreciable changes in k_3 nor in K_1.

For what concern the comparison of the compartmental modelling estimates in the tumour unaffected grey matter with the literature results, as the values of the literature findings are very variable, it was chosen to consider as reference for the comparison the average values of what was found in literature. The studies we referred to for this comparison are the following: (Sari et al., 2017), (O'Sullivan et al., 2010), (Bowen et al., 2013), (Hattori et al., 2004), (Kawai et al., 2005), (Mosconi et al., 2007), (Reivich et al., 1985), (Heiss et al., 1984) and (Lucignani et al., 1993), (Huisman et al., 2012). We considered the studies' findings in healthy grey matter tissues and briefly summarised them in Table 5.2. In that table are also reported the average and standard deviation of each parameter computed across the group of considered studies. Concerning the tumour contral-lateral grey matter a 1.2% of voxels results were discarded due to limited precision or not physiological parameters value. The average of the assessed micro- and macro-parameters in this potentially tumour unaffected region are the following: K_1, 0.16$\pm$0.06

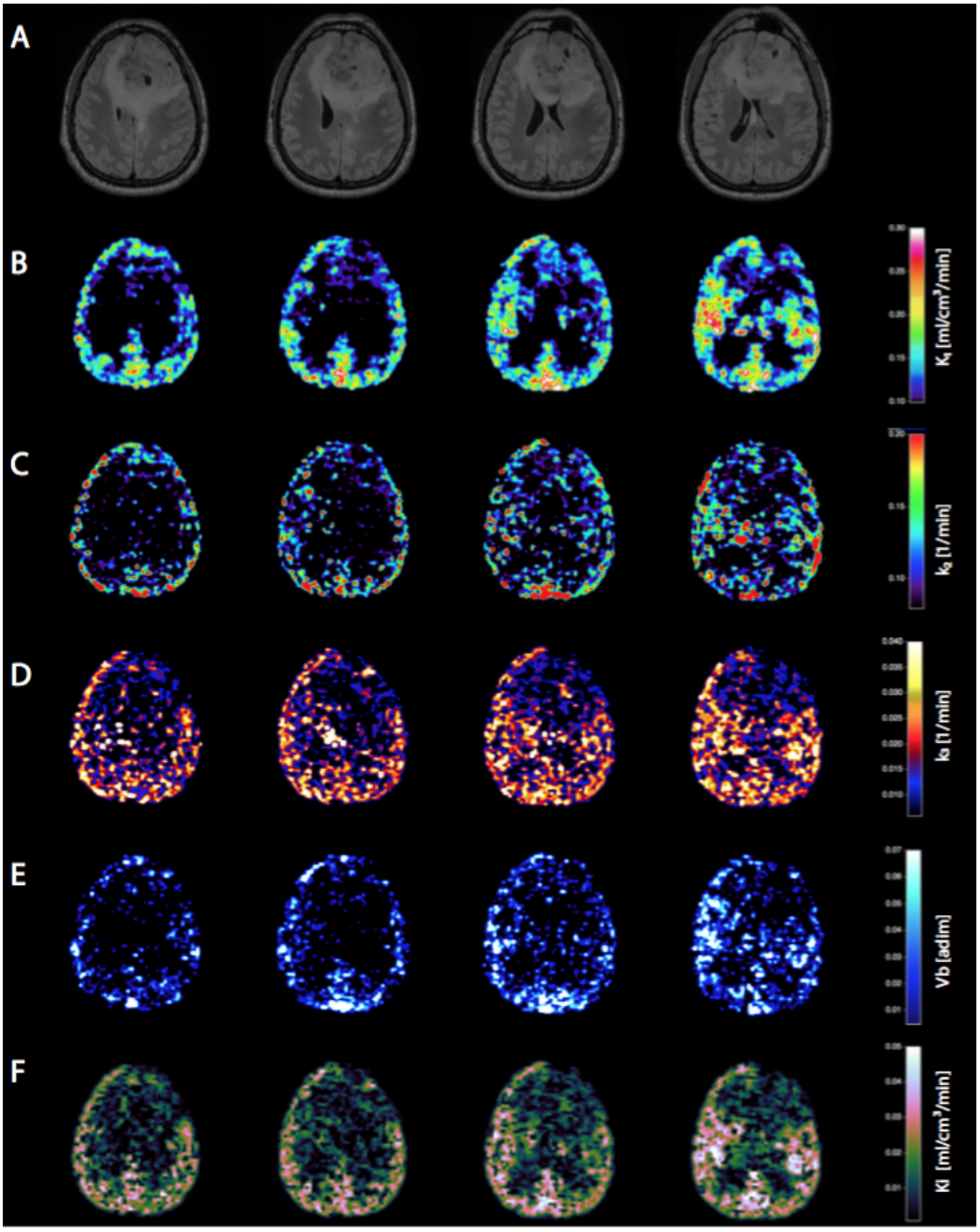

Figure 5.4: Compartmental Modelling results (tumour's upper slices). Parametric maps of K_1 (panel B), k_2 (panel C), k_3 (panel D), V_b (panel E) and Ki (panel F) estimates. Panel A, structural T2-weighted Fluid Attenuated Inversion Recovery (FLAIR).

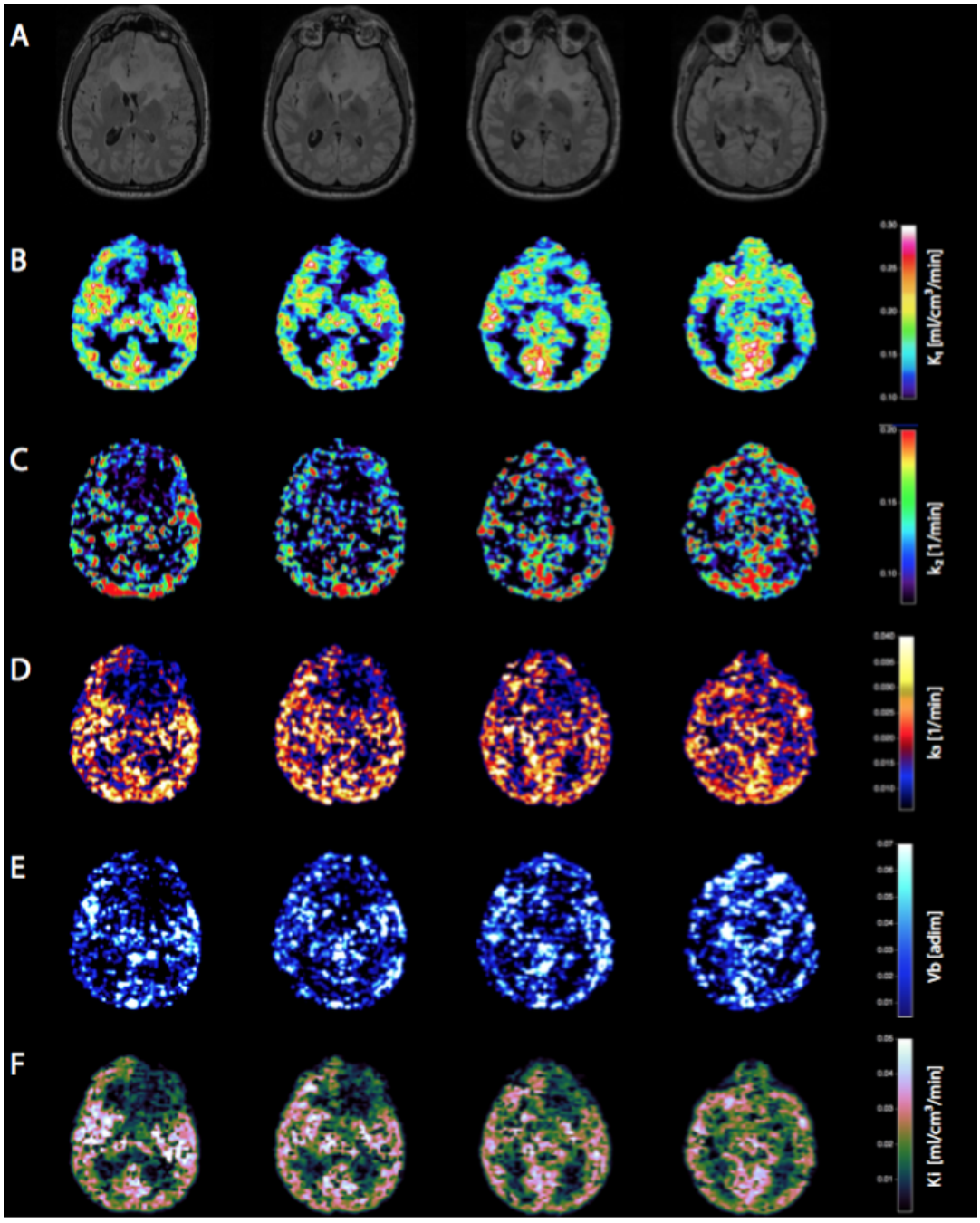

Figure 5.5: Compartmental Modelling results (tumour's lower slices). Parametric maps of K_1 (panel B), k_2 (panel C), k_3 (panel D), V_b (panel E) and Ki (panel F) estimates. Panel A, structural T2-weighted Fluid Attenuated Inversion Recovery (FLAIR).

References	K_1	k_2	k_3	V_b	$Input$
Bowen et al., 2013	0.068±0.023	0.18±0.06	0.09±0.025	–	AIF
Hattori et al., 2004	0.010±0.014	0.23±0.08	0.175±0.04	0.04±0.02	AIF
Huisman et al., 2012	0.062±0.008	0.071±0.04	0.067±0.03	–	AIF
Heiss et al., 1984	0.07±0.1	0.13±0.15	0.06±0.082	–	AIF
Kawai et al., 2005	0.082±0.012	–	0.064±0.014	–	AIF
Lucignani et al., 1993	0.11±0.02	0.07±0.02	0.04±0.01	–	AIF
Mosconi et al., 2007	0.11±0.03	0.3±0.08	0.11±0.02		AIF
O'Sullivan et al., 2010	0.13±0.05	0.15±0.1	0.1±0.1	0.085±0.05	AIF
Reivich et al., 1985	0.105±0.006	0.148±0.008	0.074±0.005		AIF
Sari et al., 2017	0.43±0.1	0.22±0.06	0.046±0.007	0.076±0.02	IDIF
Overall	0.120±0.098	0.18±0.065	0.08±0.036	0.06±0.024	

Table 5.2: Summary of literature results of ^{18}F-FDG compartmental modelling applied to the time activity curves of healthy grey matter. For each study are reported the estimates of the model parameters (i.e. K_1, k_2, k_3, V_b), as well as the type of input function employed. – refers to estimate not reported in the corresponding paper. AIF stands for arterial sampling and IDIF for image derived input function. The Overall row refers to the average and standard deviation of the parameter computed across the studies.

$ml/cm^3/min$; k_2, 0.09±0.09 $1/min$; k_3, 0.04±0.01 $1/min$; V_b, 0.03±0.10; K_i, 0.04±0.02 $ml/cm^3/min$. These results are reasonably in line with values reported in Table 5.2.

5.3.2 Resting State Connectivity Analysis Results

Independent component analysis performed on functional MR data has been able to identify the major resting state networks. In Figure 5.6 and 5.7 era respectively depicted the default mode network and the sensory-motor network spatial pattern. The default mode network is altered in the frontal regions of the right hemisphere, where the anterior cingulate cortex node of the network is completely absent, whereas residual connectivity in the left frontal lobe is recognised, even in regions of altered FLAIR signal. On the contrary, SMN is entirely present, but the network's spatial pattern is modified due to the presence of the tumour and oedema. Concerning the analysis of structural connectivity, the attention was focused on the DMN connectivity. The obtained tractogram restricted to this network is reported in Figure 5.8. Connection between posterior cingulate cortex and anterior cingulate cortex is present only for the hemisphere contra-lateral to the tumour, while links between the other nodes of the network are maintained and consistent

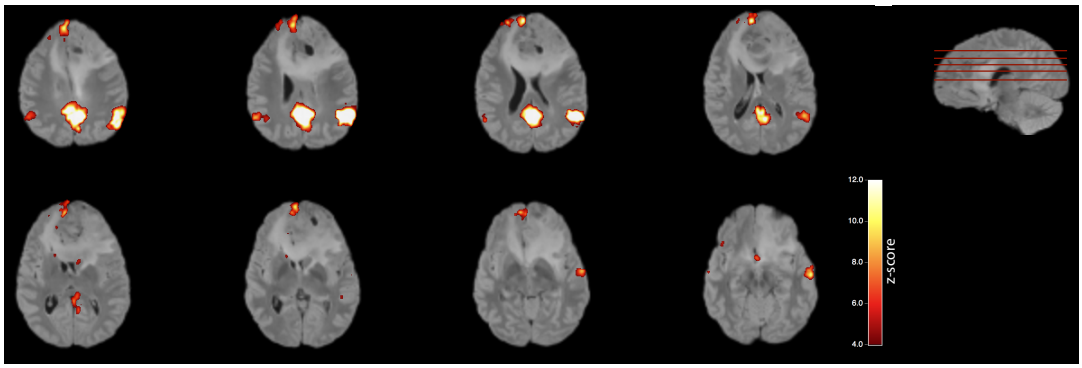

Figure 5.6: Axial view of the patient's default mode network spatial pattern. The map of the network (IC z-score, hot scale) is over-imposed on the FLAIR structural image (grey scale). In the upper-right corner, FLAIR sagittal view on which the reported slices are marked in red.

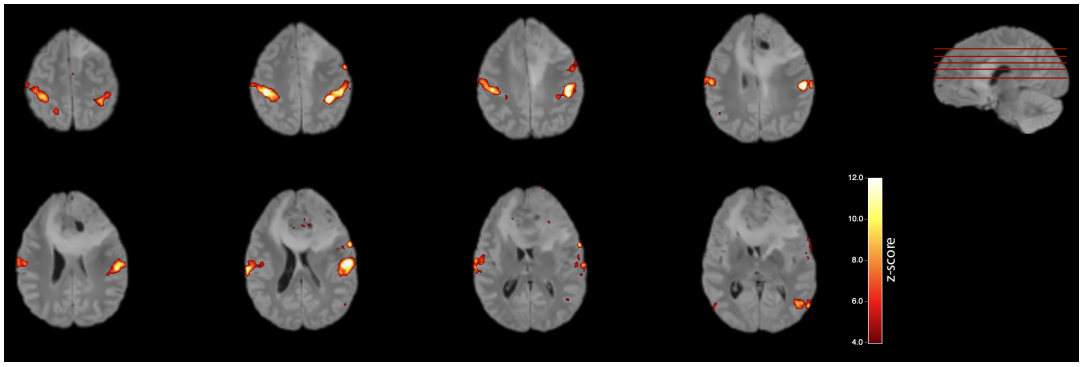

Figure 5.7: Axial view of the patient's sensory-motor network spatial pattern. The map of the network (IC z-score, hot scale) is over-imposed on the FLAIR structural image (grey scale). In the upper-right corner, FLAIR sagittal view on which the reported slices are marked in red.

with the well known pattern of the DMN, reported for example in (Horn et al., 2014).

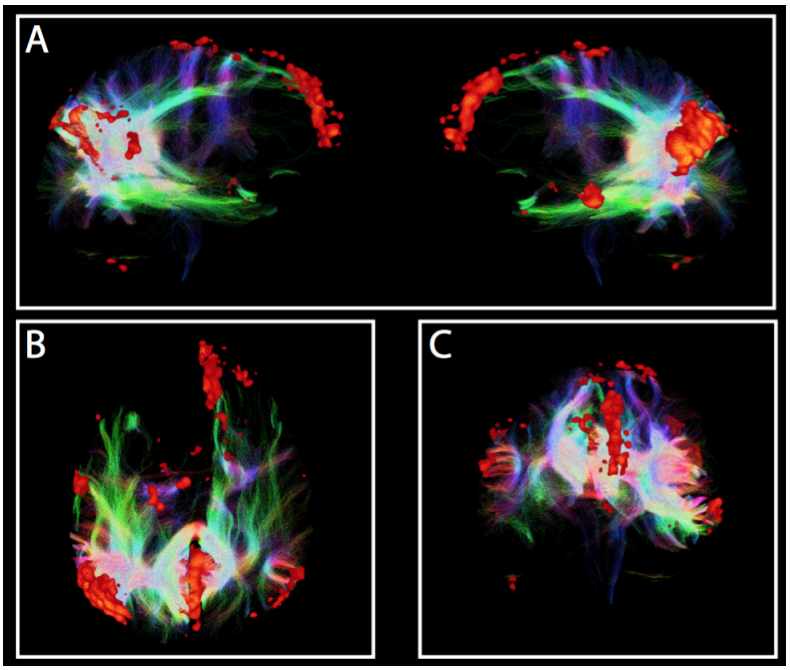

Figure 5.8: Patient's 3D tractogram colour map restricted to the patient's default mode network seed areas. Panel A, sagittal view form left and right hand side; panel B, axial view; panel C, coronal view. DMN seeds are in hot scale, according to the z-score values of the patient's DMN related independent component. Colour coding is exploited to show the direction of the fibre bundles, as default: red indicates directions in the X axis (right to left or left to right), green directions in the Y axis (posterior to anterior or anterior to posterior), and blue directions in the Z axis (foot-to-head direction or vice versa). (Radiological convention)

5.3.3 Multimodal Integration of Connectivity and Metabolic Features

The Figures 5.9 and 5.10 show how it is possible to relate our preliminary PET and MR results in order to describe the functional and structural behaviour of tumoural and peritumoural regions.
From a qualitative perspective, the metabolic and functional pattern are relates. In the first figure, the areas of activation of the sensor-motor network correspond to regions where cortical metabolism is similar to that of the healthy tissue. While, concerning the second figure, the integration of the two information enables us to identify both regions where a residual activity is present and regions where no activity can be identified. Indeed, although in the FLAIR image the DMN frontal portion is covered by oedema, the presence of residual activity can be proved from different points of view: ICA

identifies activation areas for which PET indicates metabolic consumption (oxidative phosphorylation) and perfusion not-negligible, moreover, those areas are anatomically linked to the rest of the network, as indicate by the structural connectivity analysis.

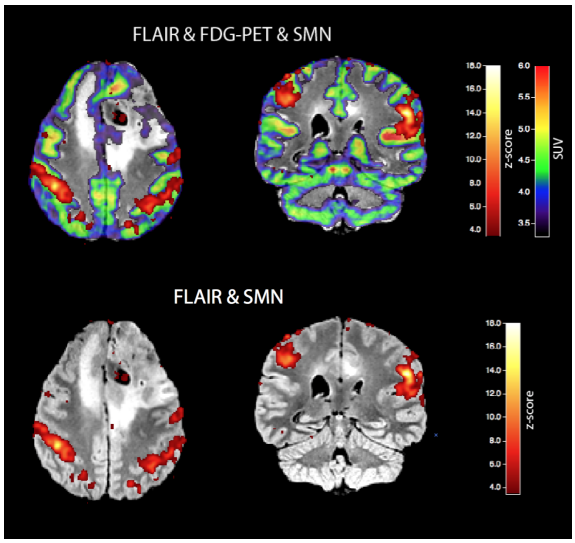

Figure 5.9: Multimodal maps of the sensory-motor network. First row depicts FLAIR structural image (grey) with over-impose standard uptake value map (rainbow) and spatial map of z-scored independent component related to SMN (hot). Second row depicts axial and coronal views of the FLAIR structural image with over-impose spatial map of the SMN.

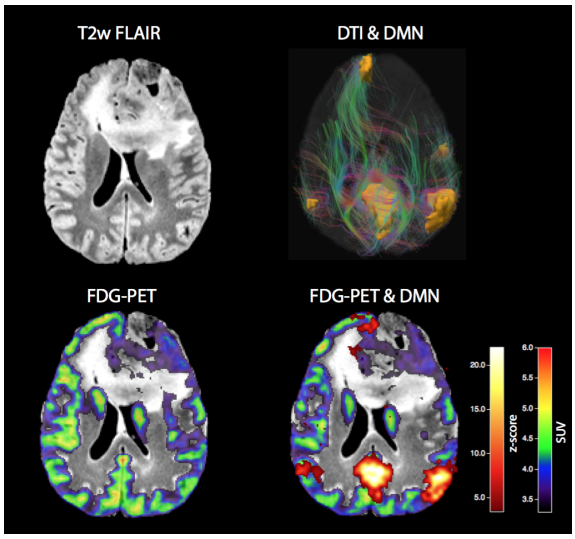

Figure 5.10: Multimodal maps of the default mode network. Top-left panel, FLAIR structural image (grey); top-right panel, DMN tractogram; bottom-left, metabolic consumption (standard uptake value, rainbow) over-imposed on FLAIR; bottom-right, DMN spatial map (hot) and metabolic consumption (rainbow) over-imposed on FLAIR.

5.4 Conclusion

The proposed framework has proved to be appropriate also for this second application, although limited to a single proof-of-concept case. As regard the analyses carried out on PET data, several limitations related to the specific clinical setting has to be faced, namely the minimal injected dose (which however was in line with the clinical indication of Azienda Italiana del Farmaco) that typically leads to limited signal to noise, the absence of an automatic pump to the tracer injection (which would allowed us to set the injection speed and to avoid collecting input function poorly in line with literature), the absence of an arterial sampling system (to be used as input function of the compartmental model that describes the tracer kinetics) and of venous samples of the tracer concentration (to be used possibly as scaling factor to correct the image derived input function tail as in population based input function described in (Zanotti-Fregonara et al., 2011)). Nonetheless, it was possible to carry out a quantitative analysis of the PET dynamics though a compartmental modelling approach using an image derived input function. This function was computed using the MR TOF image to precisely guide the selection of the voxels within the common carotid arteries, as suggested by the work of Fung and colleagues (Fung and Richard E. Carson, 2013) where however the PET camera FOV includes only the external and internal carotids. In particular, it was hypothesised that, extracting this input function from the common carotid arteries, the partial volume effect was negligible as mean diameters of those structure are $6.52 \pm 0.98 mm$ in men and $6.10 \pm 0.80 mm$ in women (according to Krejza et al., 2006) whereas the PET camera resolution of the Biograph mMR scanner is $4.3 mm$ (G. Delso, Furst, et al., 2011). Moreover, being aware of the impact of time sampling on the ability of detect a dynamic signal, two different time binning for PET images reconstruction were tested to evaluate which one was the better in describing the IDIF shape. A direct comparison between the obtained IDIF and population arterial input functions was not feasible due to the short duration of the tracer injection. However the consistency of the kinetic parameter quantified using the compartmental modelling, with the literature findings supports the reliability of the assessed IDIF. To note that to perform a fair comparison it was necessary to identify regions of grey matter from the tumour area and FLAIR hyper-intense area. Notably, when the compartmental modelling will be applied to tumour regions further confirmation of the aptness of the

2TC-3k model in describing the kinetics will be necessary, as for some particularly active tumours, the tissues alterations may be so critical that the two compartments could collapse in a single compartment.
Beside a comparison with literature, a robust validation of the results was not possible because of the lack of arterial samples to be used as input function. Moreover, to confirm those preliminary results it is fundamental applying the same framework of reconstruction and analyses to a wider pool of patients as one of the major limitation of this study is that it was carried only on one single patient.
Concerning the MR side of the study, the fMRI and DTI sequences tunning has lead to a state-of-art signal in both signals. The images quality was comparable with what is reported in literature (not shown here) as well as the estimated connectivity.
In addition, these very preliminary results has proved to be interesting and promising in terms of delineating areas with residual activity. Indeed, thanks to a multimodal integration of the two techniques results based on connectivity it was possible to highlight areas where MR structural images have displayed an altered signal intensities but both connectivity and metabolism analyses have proved that a remaining tissues activity was present. Clearly the type of information in clinical setting where the surgery has to be planned could be particularly useful. However, although this approach seems to be promising it is necessary to verify is feasibility on a wider dataset with a longitudinal approach. To this end further acquisitions are still ongoing.

Chapter 6

Conclusions

In recent years, the study of brain connectivity has received growing interest from neuroscience field, from a point of view both of a pathological condition and of a healthy brain. PET-MRI simultaneous acquisition has proven to be a promising tool for the this type of studies as it can provide complementary multimodal information about the physiological and pathophysiological processes as well as about the brain functional activity and structure. The great challenge that has been faced with this thesis was to export this kind of analysis into a clinical experimental setting, such as the one housed in the Nuclear Medicine Department of the Padova Hospital. For this purpose a framework of acquisition, reconstruction and quantification has been developed. During this PhD programme several aspects of the hybrid PET-MRI acquisition have been addressed. At first, we dealt with the planning of MR image acquisition protocols so that they could provide images that were suitable for functional and structural connectivity analysis at state-of-art level, and at the same time that could meet the constraints imposed by the clinic, particularly in terms of time. To this end, a fine tuning of the MR pulse sequences was required, both to reduce acquisition times and to improve image resolution, field of view and signal to noise ratio.
Then, we have been involved in the reconstruction of PET images, for which a pipeline for the scanner off-line reconstruction has been implemented. The pipeline includes a step of advanced attenuation correction step, which leads to a better attenuation correction with respect to the scanner one, and provides the possibility of reconstructing the list mode PET dynamics using different time grids. In particular, the possibility of reconstructing on different time grids has proved to be very useful in the PET quantification phase. The quantification of PET dynamics was performed through a compartmental modelling approach, which required an accurate input function. One of the main limitation our clinical setting is the lack of arterial blood samples to be used as input function, therefore it was necessary to employ an input

function derived directly from the PET images. To this end it was fundamental to reconstruct the PET signals identifying and using a time sampling grid suitable for detecting the shape of the IDIF signal.
A second severe constrain imposed by the clinical setting is the duration of the PET/MR acquisition. The compartmental model that better describe a tracer dynamic is typically developed and estimated using PET data collected over a long period, however this was not the case of first of the two studies described in this work. As we were interested at computing a proxy of the cerebral blood flow, which in literature has been proven to be quantifiable using long PET scan of ^{11}C-PiB, it was necessary to develop and evaluate how to reduce the well known compartmental model of our tracer that is an analogous of ^{11}C-PiB to reliably estimate this parameter. The proposed reduced model has proved to be adequate in describing the collected data and estimating reliable proxy of CBF.
Once optimized, the acquisition setting was applied to two different studies, a first conducted on patients affected by Parkinson's Disease and dementia (PDD), and a second one on high grade gliomas.
The acquisition framework as well as the implemented analysis pipeline proved to be adequate to the clinical context and in both cases provided promising results. Indeed, in the case of the PDD study thanks to the analyses conducted, it was possible to obtain first results on the relationship between the pathophysiological process underlying the dementia (i.e. amyloid burden and decrease of cerebral blood flow) and the structural and functional variations experienced by resting state cognitive networks. While, concerning the study of high-grade gliomas, the integrated approach to the study of connectivity has allowed to identify regions with residual activity and thus to provide information of potential interest for clinical practice.
Overall, although additional data is needed to confirm the our first clinical results, simultaneous PET/MRI acquisitions and the implemented analysis pipeline have proven to be a good tool for studying the pathological alterations in connectivity.
With this thesis we have shown two promising proof-of-concept applications of the proposed framework to study the alterations of brain connectivity in relation to ongoing pathological processes. But ongoing acquisitions on patients affected by high grade glioma will lead to a wider dataset for which it will be exiting find new ways of combining structural, functional, and metabolic informations possibly introducing causal interactions between them, in order to better understand the pathology.

References

Aiello, Marco, Carlo Cavaliere, and Marco Salvatore (2016). "Hybrid PET/MR imaging and brain connectivity". In: *Frontiers in Neuroscience* 10.MAR, pp. 1–8. ISSN: 1662453X. DOI: 10.3389/fnins.2016.00064.

Aiello, Marco, Elena Salvatore, et al. (2015). "Relationship between simultaneously acquired resting-state regional cerebral glucose metabolism and functional MRI: A PET/MR hybrid scanner study". In: *NeuroImage* 113, pp. 111–121. ISSN: 10959572. DOI: 10.1016/j.neuroimage.2015.03.017.

Akaike, Hirotugu (1974). "A New Look at the Statistical Model Identification". In: *IEEE Transactions on Automatic Control* 19.6, pp. 716–723. ISSN: 15582523. DOI: 10.1109/TAC.1974.1100705.

Alexander, Daniel C. and Gareth J. Barker (2005). "Optimal imaging parameters for fiber-orientation estimation in diffusion MRI". In: *NeuroImage* 27.2, pp. 357–367. ISSN: 10538119. DOI: 10.1016/j.neuroimage.2005.04.008.

Allen, Elena A. et al. (2012). "Tracking whole-brain connectivity dynamics in the resting state". In: *Cerebral Cortex* 24.3, pp. 663–676. ISSN: 10473211. DOI: 10.1093/cercor/bhs352.

Alsop, David C. et al. (2015). "Recommended implementation of arterial spin-labeled Perfusion mri for clinical applications: A consensus of the ISMRM Perfusion Study group and the European consortium for ASL in dementia". In: *Magnetic Resonance in Medicine* 73.1, pp. 102–116. ISSN: 15222594. DOI: 10.1002/mrm.25197.

Anderson, Jeffrey S. et al. (2011). "Reproducibility of single-subject functional connectivity measurements". In: *American Journal of Neuroradiology* 32.3, pp. 548–555. ISSN: 01956108. DOI: 10.3174/ajnr.A2330.

Andersson, Jesper L R, Stefan Skare, and John Ashburner (2003). "How to correct susceptibility distortions in spin-echo echo-planar images: Application to diffusion tensor imaging". In: *NeuroImage* 20.2, pp. 870–888. ISSN: 10538119. DOI: 10.1016/S1053-8119(03)00336-7.

Andersson, Jesper L.R. and Stamatios N. Sotiropoulos (2016). "An integrated approach to correction for off-resonance effects and subject movement in

diffusion MR imaging". In: *NeuroImage* 125, pp. 1063–1078. ISSN: 10959572. DOI: 10.1016/j.neuroimage.2015.10.019.

Atzil, Shir et al. (2017). "Dopamine in the medial amygdala network mediates human bonding". In: *Proceedings of the National Academy of Sciences* 114.9, pp. 2361–2366. ISSN: 0027-8424. DOI: 10.1073/pnas.1612233114.

Avants, Brian B., Nicholas J. Tustison, Gang Song, et al. (2011). "A reproducible evaluation of ANTs similarity metric performance in brain image registration". In: *NeuroImage* 54.3, pp. 2033–2044. ISSN: 10538119. DOI: 10.1016/j.neuroimage.2010.09.025.

Avants, Brian B., Nicholas J. Tustison, Michael Stauffer, et al. (2014). "The Insight ToolKit image registration framework". In: *Frontiers in Neuroinformatics* 8.April, pp. 1–13. ISSN: 1662-5196. DOI: 10.3389/fninf.2014.00044.

Azeez, Azeezat K. and Bharat B. Biswal (2017). "A Review of Resting-State Analysis Methods". In: *Neuroimaging Clinics of North America* 27.4, pp. 581–592. ISSN: 15579867. DOI: 10.1016/j.nic.2017.06.001.

Baik, Kyoungwon et al. (2014). "Dopaminergic modulation of resting-state functional connectivity in de novo patients with Parkinson's disease". In: *Human Brain Mapping* 35.11, pp. 5431–5441. ISSN: 10970193. DOI: 10.1002/hbm.22561.

Bailey, Dale L et al. (2005). *Positron emission tomography*. Springer-Verlag London. ISBN: 1852337982.

Barrett, H. H., D. W. Wilson, and B. M.W. Tsui (1994). "Noise properties of the EM algorithm. I. Theory". In: *Physics in Medicine and Biology* 39.5, pp. 833–846. ISSN: 00319155. DOI: 10.1088/0031-9155/39/5/004.

Basser, Peter J (1995). "Inferring Microstructural Features and the Physiological State of Tissues from Diffusion- Weighted Images". In: *Nmr in Biomedicine* 8.September, pp. 333–344. ISSN: 10991492. DOI: 10.1002/nbm.1940080707.

Bassett, D. S. et al. (2008). "Hierarchical Organization of Human Cortical Networks in Health and Schizophrenia". In: *Journal of Neuroscience* 28.37, pp. 9239–9248. ISSN: 0270-6474. DOI: 10.1523/JNEUROSCI.1929-08.2008.

Behzadi, Yashar et al. (2007). "A component based noise correction method (CompCor) for BOLD and perfusion based fMRI". In: *NeuroImage* 37.1, pp. 90–101. ISSN: 10538119. DOI: 10.1016/j.neuroimage.2007.04.042.

Benjamini, Yoav and Yosef Hochberg (1995). *Controlling the false discovery rate: a practical and powerful approach to multiple testing*. DOI: 10.2307/2346101.

Berker, Yannick and Yusheng Li (2016). "Attenuation correction in emission tomography using the emission data-A review". In: *Medical Physics* 43.2, pp. 807–832. ISSN: 00942405. DOI: 10.1118/1.4938264.

Bertoldo, Alessandra et al. (2001). "Kinetic modeling of [(18)F]FDG in skeletal muscle by PET: a four-compartment five-rate-constant model." In: *American journal of physiology. Endocrinology and metabolism* 281.3, E524–E536. ISSN: 0193-1849.

Binnewijzend, Maja A. A. et al. (2013). "Cerebral Blood Flow Measured with 3D Pseudocontinuous Arterial Spin-labeling MR Imaging in Alzheimer Disease and Mild Cognitive Impairment: A Marker for Disease Severity". In: *Radiology* 267.1, pp. 221–230. ISSN: 0033-8419. DOI: 10.1148/radiol.12120928.

Birn, Rasmus M. et al. (2013). "The effect of scan length on the reliability of resting-state fMRI connectivity estimates". In: *NeuroImage* 83, pp. 550–558. ISSN: 10538119. DOI: 10.1016/j.neuroimage.2013.05.099.

Biswal, Bharat (2015). "Resting-State Functional Connectivity". In: *Brain Mapping: An Encyclopedic Reference*. Vol. 1. Elsevier, pp. 581–585. ISBN: 9780123970251. DOI: 10.1016/B978-0-12-397025-1.00335-3.

Biswal, Bharat et al. (1995). "Functional connectivity in the motor cortex of resting human brain using echo-planar mri". en. In: *Magnetic Resonance in Medicine* 34.4, pp. 537–541. ISSN: 07403194. DOI: 10.1002/mrm.1910340409.

Biundo, R., L. Weis, and A. Antonini (2016). "Cognitive decline in Parkinson's disease: the complex picture". In: *npj Parkinson's Disease* 2.1, p. 16018. ISSN: 2373-8057. DOI: 10.1038/npjparkd.2016.18.

Biundo, R., L. Weis, S. Bostantjopoulou, et al. (2016). "MMSE and MoCA in Parkinson's disease and dementia with Lewy bodies: a multicenter 1-year follow-up study". In: *Journal of Neural Transmission* 123.4, pp. 431–438. ISSN: 14351463. DOI: 10.1007/s00702-016-1517-6.

Blomquist, Gunnar et al. (2008). "Unidirectional Influx and Net Accumulation of PIB." In: *The open neuroimaging journal* 2, pp. 114–25. ISSN: 1874-4400. DOI: 10.2174/1874440000802010114.

Bowen, Spencer L et al. (2013). "Influence of the partial volume correction method on 18 F-fluorodeoxyglucose brain kinetic modelling from dynamic PET images reconstructed with resolution model based OSEM". In: *Physics*

in Medicine and Biology 58.20, pp. 7081–7106. ISSN: 0031-9155. DOI: 10.1088/0031-9155/58/20/7081.

Brier, M. R. et al. (2012). "Loss of Intranetwork and Internetwork Resting State Functional Connections with Alzheimer's Disease Progression". In: *Journal of Neuroscience* 32.26, pp. 8890–8899. ISSN: 0270-6474. DOI: 10.1523/JNEUROSCI.5698-11.2012.

Brooks, David J. (2009). "Imaging amyloid in Parkinson's disease dementia and dementia with Lewy bodies with positron emission tomography". In: *Movement Disorders* 24.SUPPL. 2, pp. 742–747. ISSN: 08853185. DOI: 10.1002/mds.22581.

Burgos, Ninon et al. (2014). "Attenuation correction synthesis for hybrid PET-MR scanners: Application to brain studies". In: *IEEE Transactions on Medical Imaging* 33.12, pp. 2332–2341. ISSN: 1558254X. DOI: 10.1109/TMI.2014.2340135.

Campbell, Meghan C et al. (2015). "CSF proteins and resting-state functional connectivity in Parkinson disease CSF proteins and resting-state functional connectivity in Parkinson disease". In: MAY, pp. 2413–2422. ISSN: 1526-632X. DOI: 10.1212/WNL.0000000000001681.

Carney, Jonathan P.J. et al. (2006). "Method for transforming CT images for attenuation correction in PET/CT imaging". In: *Medical Physics* 33.4, pp. 976–983. ISSN: 00942405. DOI: 10.1118/1.2174132.

Carson, E, Claudio. Cobelli, and Ludwik Finkelstein (1983). *The mathematical modelling of metabolic and endocrine systems*. New York: J. Wiley, p. 394. ISBN: 0-471-08660-6.

Carson, Richard E (2003). "Tracer Kinetic Modeling in PET". In: *Positron Emission Tomography: Basic Science*, pp. 147–179. ISSN: 15568598. DOI: 10.1016/j.cpet.2007.08.003.

Carson, Richard E., Margaret E Daube-Witherspoon, and Peter Herscovitch (1998). *Quantitative functional brain imaging with positron emission tomography*. Academic Press, p. 503. ISBN: 9780121613402.

Caruyer, Emmanuel et al. (2013). "Design of multishell sampling schemes with uniform coverage in diffusion MRI". In: *Magnetic Resonance in Medicine* 69.6, pp. 1534–1540. ISSN: 07403194. DOI: 10.1002/mrm.24736.

Catana, C. (2017). "Principles of Simultaneous PET/MR Imaging". In: *Magnetic Resonance Imaging Clinics of North America* 25.2, pp. 231–243. ISSN: 15579786. DOI: 10.1016/j.mric.2017.01.002.

Catana, C. et al. (2010). "Toward Implementing an MRI-Based PET Attenuation-Correction Method for Neurologic Studies on the MR-PET Brain Prototype". In: *Journal of Nuclear Medicine* 51.9, pp. 1431–1438. ISSN: 0161-5505. DOI: 10.2967/jnumed.109.069112.

Catani, Marco et al. (2013). "Connectomic approaches before the connectome". In: *NeuroImage* 80, pp. 2–13. ISSN: 10538119. DOI: 10.1016/j.neuroimage.2013.05.109.

Cecchin, Diego et al. (2017). "Brain PET and functional MRI: why simultaneously using hybrid PET/MR systems?" In: *The Quarterly Journal of Nuclear Medicine and Molecular imaging* 61.4, pp. 345–359. DOI: 10.23736/S1824-4785.17.03008-4.

Chen, Bing et al. (2015). "Individual variability and test-retest reliability revealed by ten repeated resting-state brain scans over one month". In: *PLoS ONE* 10.12, pp. 1–21. ISSN: 19326203. DOI: 10.1371/journal.pone.0144963.

Chen, J. Jean, H. Diana Rosas, and David H. Salat (2011). "Age-associated reductions in cerebral blood flow are independent from regional atrophy". In: *NeuroImage* 55.2, pp. 468–478. ISSN: 10538119. DOI: 10.1016/j.neuroimage.2010.12.032.

Chen, Kewei et al. (1998). "Noninvasive Quantification of the Cerebral Metabolic Rate for Glucose Using Positron Emission Tomography, 18 F-Fluoro-2-Deoxyglucose, the Patlak Method, and an Image-Derived Input Function". In: *Journal of Cerebral Blood Flow & Metabolism* 18.7, pp. 716–723. ISSN: 0271-678X. DOI: 10.1097/00004647-199807000-00002.

Chen, Y. J. et al. (2015). "Relative 11C-PiB Delivery as a Proxy of Relative CBF: Quantitative Evaluation Using Single-Session 15O-Water and 11C-PiB PET". In: *Journal of Nuclear Medicine* 56.8, pp. 1199–1205. ISSN: 0161-5505. DOI: 10.2967/jnumed.114.152405.

Chen, Yasheng and Hongyu An (2017). "Attenuation Correction of PET/MR Imaging". In: *Magnetic Resonance Imaging Clinics of North America* 25.2, pp. 245–255. ISSN: 15579786. DOI: 10.1016/j.mric.2016.12.001.

Cheng, Yafang and Imam Şamil Yetik (2011). "Propagation of blood function errors to the estimates of kinetic parameters with dynamic PET". In: *International Journal of Biomedical Imaging* 2011, p. 234679. ISSN: 16874188. DOI: 10.1155/2011/234679.

Chiang, Sharon and Zulfi Haneef (2014). *Graph theory findings in the pathophysiology of temporal lobe epilepsy*. DOI: 10.1016/j.clinph.2014.04.004.

Christen, Thomas et al. (2015). "Noncontrast mapping of arterial delay and functional connectivity using resting-state functional MRI: A study in moyamoya patients". In: *Journal of Magnetic Resonance Imaging* 41.2, pp. 424–430. ISSN: 15222586. DOI: 10.1002/jmri.24558.

Ciris, P. A. and R. Todd Constable (2015). "MRI and fMRI Optimizations and Applications". In: *Brain Mapping: An Encyclopedic Reference*. Vol. 1. Elsevier, pp. 183–190. ISBN: 9780123970251. DOI: 10.1016/B978-0-12-397025-1.00021-X.

Coyle, Joseph T. et al. (2016). "A Perspective on the history of the concept of "disconnectivity" in schizophrenia". In: *Harv Rev Psychiatry* 24.2, pp. 80–86. ISSN: 1527-5418. DOI: 10.1097/HRP.0000000000000102.

Crone, Christian (1963). "The Permeability of Capillaries in Various Organs as Determined by Use of the 'Indicator Diffusion' Method". In: *Acta Physiologica Scandinavica* 58.4, pp. 292–305. ISSN: 1365201X. DOI: 10.1111/j.1748-1716.1963.tb02652.x.

Delso, G., M. Carl, et al. (2014). "Anatomic Evaluation of 3-Dimensional Ultrashort-Echo-Time Bone Maps for PET/MR Attenuation Correction". In: *Journal of Nuclear Medicine* 55.5, pp. 780–785. ISSN: 0161-5505. DOI: 10.2967/jnumed.113.130880.

Delso, G., S. Furst, et al. (2011). "Performance Measurements of the Siemens mMR Integrated Whole-Body PET/MR Scanner". In: *Journal of Nuclear Medicine* 52.12, pp. 1914–1922. ISSN: 0161-5505. DOI: 10.2967/jnumed.111.092726.

Delso, G., F. Wiesinger, et al. (2015). "Clinical Evaluation of Zero-Echo-Time MR Imaging for the Segmentation of the Skull". In: *Journal of Nuclear Medicine* 56.3, pp. 417–422. ISSN: 0161-5505. DOI: 10.2967/jnumed.114.149997.

Delso, Gaspar and Sibylle Ziegler (2009). "PET/MRI system design". In: *European Journal of Nuclear Medicine and Molecular Imaging* 36.SUPPL. 1, pp. 86–92. ISSN: 16197070. DOI: 10.1007/s00259-008-1008-6.

Dijk, Koene R A van, Mert R. Sabuncu, and Randy L. Buckner (2012). "The influence of head motion on intrinsic functional connectivity MRI". In: *NeuroImage* 59.1, pp. 431–438. ISSN: 10538119. DOI: 10.1016/j.neuroimage.2011.07.044.

Edison, P., D. J. Brooks, et al. (2009). "Strategies for the generation of parametric images of [11C]PIB with plasma input functions considering discriminations and reproducibility". In: *NeuroImage* 48.2, pp. 329–338. ISSN: 10538119. DOI: 10.1016/j.neuroimage.2009.06.079.

Edison, P., C. C. Rowe, et al. (2008). "Amyloid load in Parkinson's disease dementia and Lewy body dementia measured with [11C]PIB positron emission tomography". In: *Journal of Neurology, Neurosurgery & Psychiatry* 79.12, pp. 1331–1338. ISSN: 0022-3050. DOI: 10.1136/jnnp.2007.127878.

Eldib, Mootaz et al. (2016). "Attenuation Correction for Magnetic Resonance Coils in Combined PET/MR Imaging A Review". In: *PET Clinics* 11.2, pp. 151–160. ISSN: 18799809. DOI: 10.1016/j.cpet.2015.10.004.

Elman, Jeremy A. et al. (2016). "Effects of Beta-Amyloid on Resting State Functional Connectivity Within and between Networks Reflect Known Patterns of Regional Vulnerability". In: *Cerebral Cortex* 26.2, pp. 695–707. ISSN: 14602199. DOI: 10.1093/cercor/bhu259.

Farid, Karim et al. (2015). "Early-phase 11C-PiB PET in amyloid angiopathy-related symptomatic cerebral hemorrhage: Potential diagnostic value?" In: *PLoS ONE* 10.10, pp. 1–11. ISSN: 19326203. DOI: 10.1371/journal.pone.0139926.

Farquharson, Shawna et al. (2016). *Diffusion Tensor Imaging: A Practical Handbook*. Springer New York. ISBN: 978-1-4939-3118-7. DOI: 10.1007/978-1-4939-3118-7{_}20.

Feinberg, David A. and Kawin Setsompop (2013). "Ultra-fast MRI of the human brain with simultaneous multi-slice imaging". In: *Journal of Magnetic Resonance* 229, pp. 90–100. ISSN: 10907807. DOI: 10.1016/j.jmr.2013.02.002.

Feng, Dagan, Sung Cheng Huang, and Xinmin Wang (1993). "Models for computer simulation studies of input functions for tracer kinetic modeling with positron emission tomography". In: *International Journal of Bio-Medical Computing* 32.2, pp. 95–110. ISSN: 00207101. DOI: 10.1016/0020-7101(93)90049-C.

Fernandes, C. et al. (2017). *Glioblastoma*. Ed. by S. De Vleeschouwer. Codon Oubblication Brisbane, pp. 197–241. ISBN: 9780994438126. DOI: 10.15586/codon.glioblastoma.2017.

Fischl, Bruce, M. I. Sereno, and A. M. Dale (1999). "Cortical Surface-Based Analysis: II: Inflation, Flattening, and a Surface-Based Coordinate System". In: *NeuroImage* 9.2, pp. 195–207. ISSN: 10538119. DOI: 10.1006/nimg.1998.0396.

Forsberg, Anton et al. (2012). "The use of PIB-PET as a dual pathological and functional biomarker in AD". In: *Biochimica et Biophysica Acta - Molecular*

Basis of Disease 1822.3, pp. 380–385. ISSN: 09254439. DOI: 10.1016/j.bbadis.2011.11.006.

Fox, Michael D. (2010). "Clinical applications of resting state functional connectivity". In: *Frontiers in Systems Neuroscience* 4.June. ISSN: 16625137. DOI: 10.3389/fnsys.2010.00019.

Friston, K. J. (1994). "Functional and effective connectivity in neuroimaging: A synthesis". In: *Human Brain Mapping* 2.1-2, pp. 56–78. ISSN: 10659471. DOI: 10.1002/hbm.460020107.

— (2011). "Functional and Effective Connectivity: A Review". In: *Brain Connectivity* 1.1, pp. 13–36. ISSN: 2158-0014. DOI: 10.1089/brain.2011.0008.

Friston, K. J. et al. (1993). "Functional Connectivity: The Principal-Component Analysis of Large (PET) Data Sets". In: *Journal of Cerebral Blood Flow & Metabolism* 13.1, pp. 5–14. ISSN: 0271-678X. DOI: 10.1038/jcbfm.1993.4.

Fung, Edward K. and Richard E. Carson (2013). "Cerebral blood flow with [15O]water PET studies using an image-derived input function and MR-defined carotid centerlines". In: *Physics in Medicine and Biology* 58.6, pp. 1903–1923. ISSN: 00319155. DOI: 10.1088/0031-9155/58/6/1903.

Gambhir, S S et al. (1989). "Simple noninvasive quantification method for measuring myocardial glucose utilization in humans employing positron emission tomography and fluorine-18 deoxyglucose." In: *Journal of nuclear medicine : official publication, Society of Nuclear Medicine* 30.3, pp. 359–366. ISSN: 0161-5505.

Gelb, Douglas J., Eugene Oliver, and Sid Gilman (1999). "Diagnostic Criteria for Parkinson Disease". In: *Archives of Neurology* 56.1, p. 33. ISSN: 0003-9942. DOI: 10.1001/archneur.56.1.33.

Ghinda, Diana C. et al. (2018). "How much is enough—Can resting state fMRI provide a demarcation for neurosurgical resection in glioma?" In: *Neuroscience and Biobehavioral Reviews* 84.December 2017, pp. 245–261. ISSN: 18737528. DOI: 10.1016/j.neubiorev.2017.11.019.

Gjedde, Albert et al. (2013). "Blood-brain transfer of Pittsburgh compound B in humans". In: *Frontiers in Aging Neuroscience* 5.NOV, pp. 1–9. ISSN: 16634365. DOI: 10.3389/fnagi.2013.00070.

Glasser, Matthew F. et al. (2013). "The minimal preprocessing pipelines for the Human Connectome Project". In: *NeuroImage* 80, pp. 105–124. ISSN: 10538119. DOI: 10.1016/j.neuroimage.2013.04.127.

Glover, Gary H. (2011). *Overview of functional magnetic resonance imaging*. DOI: 10.1016/j.nec.2010.11.001.

Gomperts, SN et al. (2013). "Amyloid is linked to cognitive decline in patients with Parkinson disease without dementia." In: *Neurology* 80.1, pp. 85–91. ISSN: 0028-3878. DOI: 10.1212/WNL.0b013e31827b1a07.

Gong, Kuang et al. (2017). "Attenuation Correction for Brain PET imaging using Deep Neural Network based on Dixon and ZTE MR images". In: pp. 1–14. URL: http://arxiv.org/abs/1712.06203.

Gonzalez-Castillo, Javier et al. (2014). "The spatial structure of resting state connectivity stability on the scale of minutes". In: *Frontiers in Neuroscience* 8.8 JUN, pp. 1–19. ISSN: 1662453X. DOI: 10.3389/fnins.2014.00138.

Gordon, Evan M. et al. (2016). "Generation and Evaluation of a Cortical Area Parcellation from Resting-State Correlations". In: *Cerebral Cortex* 26.1, pp. 288–303. ISSN: 14602199. DOI: 10.1093/cercor/bhu239.

Gratwicke, James, Marjan Jahanshahi, and Thomas Foltynie (2015). "Parkinson's disease dementia: A neural networks perspective". In: *Brain* 138.6, pp. 1454–1476. ISSN: 14602156. DOI: 10.1093/brain/awv104.

Greicius, Michael D. et al. (2007). "Resting-State Functional Connectivity in Major Depression: Abnormally Increased Contributions from Subgenual Cingulate Cortex and Thalamus". In: *Biological Psychiatry* 62.5, pp. 429–437. ISSN: 00063223. DOI: 10.1016/j.biopsych.2006.09.020.

Griswold, Mark A. et al. (2002). "Generalized Autocalibrating Partially Parallel Acquisitions (GRAPPA)". In: *Magnetic Resonance in Medicine* 47.6, pp. 1202–1210. ISSN: 07403194. DOI: 10.1002/mrm.10171.

Grothe, Michel J. and Stefan J. Teipel (2016). "Spatial patterns of atrophy, hypometabolism, and amyloid deposition in Alzheimer's disease correspond to dissociable functional brain networks". In: *Human Brain Mapping* 37.1, pp. 35–53. ISSN: 10970193. DOI: 10.1002/hbm.23018.

Gunn, R. N., S. R. Gunn, and V. J. Cunningham (2001). "Positron emission tomography compartmental models." In: *Journal of Cerebral Blood Flow and Metabolism* 21.6, pp. 635–652. ISSN: 0271-678X. DOI: 10.1097/00004647-200106000-00002.

Haacke, Mark E et al. (1999). *Magnetic Resonance Imaging: Physical Principles and Sequence Design*. ISBN: 9780471720850. DOI: 10.1063/1.3554697.

Haggstrom, I. et al. (2015). "A Monte Carlo Study of the Dependence of Early Frame Sampling on Uncertainty and Bias in Pharmacokinetic Parameters from Dynamic PET". In: *Journal of Nuclear Medicine Technology* 43.1, pp. 53–60. ISSN: 0091-4916. DOI: 10.2967/jnmt.114.141754.

Hagmann, P. et al. (2008). "Mapping the structural core of human cerebral cortex". In: *PLoS Biology* 6.7, pp. 1479–1493. ISSN: 15449173. DOI: 10.1371/journal.pbio.0060159.

Hammer, B. E. (1991). *NMR-PET scanner apparatus*. DOI: https://doi.org/10.1016/0730-725X(91)90402-8.

Hammer, Bruce E., Nelson L. Christensen, and Brian G. Heil (1994). "Use of a magnetic field to increase the spatial resolution of positron emission tomography". In: *Medical Physics* 21.12, pp. 1917–1920. ISSN: 00942405. DOI: 10.1118/1.597178.

Han, Xiao (2017). "MR-based synthetic CT generation using a deep convolutional neural network method:" in: *Medical Physics* 44.4, pp. 1408–1419. ISSN: 00942405. DOI: 10.1002/mp.12155.

Hatashita, Shizuo et al. (2014). "18F Flutemetamol amyloid-beta PET imaging compared with [11C]PIB across the spectrum of Alzheimer's disease". In: *European Journal of Nuclear Medicine and Molecular Imaging* 41.2, pp. 290–300. ISSN: 16197089. DOI: 10.1007/s00259-013-2564-y.

Hattori, N et al. (2004). "Acute changes in regional cerebral (18)F-FDG kinetics in patients with traumatic brain injury". In: *J Nucl Med* 45.5, pp. 775–783. ISSN: 0161-5505.

He, Biyu J. et al. (2007). "Breakdown of Functional Connectivity in Frontoparietal Networks Underlies Behavioral Deficits in Spatial Neglect". In: *Neuron* 53.6, pp. 905–918. ISSN: 08966273. DOI: 10.1016/j.neuron.2007.02.013.

He, Yong et al. (2009). "Neuronal networks in Alzheimer's disease". In: *Neuroscientist* 15.4, pp. 333–350. ISSN: 10738584. DOI: 10.1177/1073858409334423.

Heiss, W.-D. et al. (1984). "Regional Kinetic Constants and Cerebral Metabolic Rate for Glucose in Normal Human Volunteers Determiend by Dynamic Positron Emission Tomography of [18F]-2-Fluoro-2-deoxy-D-glucose". In: *Journal of Cerebral Blood Flow & Metabolism* 4, pp. 212–223.

Henkin, Robert E. et al. (2006). *Nuclear Medicine (2nd ed.)* Mosby. ISBN: 978-0323028981.

Hepp, Dagmar H. et al. (2016). "Distribution and load of amyloid-b pathology in Parkinson disease and dementia with lewy bodies". In: *Journal of Neuropathology and Experimental Neurology* 75.10, pp. 936–945. ISSN: 15546578. DOI: 10.1093/jnen/nlw070.

Herholz, Karl (2017). "Brain Tumors: An Update on Clinical PET Research in Gliomas". In: *Seminars in Nuclear Medicine* 47.1, pp. 5–17. ISSN: 15584623. DOI: 10.1053/j.semnuclmed.2016.09.004.

Heurling, Kerstin et al. (2015). "Parametric imaging and quantitative analysis of the PET amyloid ligand [18F]flutemetamol". In: *NeuroImage* 121, pp. 184–192. ISSN: 10959572. DOI: 10.1016/j.neuroimage.2015.07.037.

Heußer, Thorsten et al. (2017). "MLAA-based attenuation correction of flexible hardware components in hybrid PET/MR imaging". In: *EJNMMI Physics* 4.1. ISSN: 21977364. DOI: 10.1186/s40658-017-0177-4.

Hirsch, Jochen G. et al. (2003). "Deviations from the diffusion tensor model as revealed by contour plot visualization using high angular resolution diffusion-weighted imaging (HARDI)". In: *Magnetic Resonance Materials in Physics, Biology and Medicine* 16.2, pp. 93–102. ISSN: 09685243. DOI: 10.1007/s10334-003-0011-y.

Horn, Andreas et al. (2014). "The structural-functional connectome and the default mode network of the human brain". In: *NeuroImage* 102.P1, pp. 142–151. ISSN: 10959572. DOI: 10.1016/j.neuroimage.2013.09.069.

Horwitz, B., R. Duara, and S. I. Rappoport (1984). "of glucose rates between brain regions: Application to healthy males in a reduced state of sensory input". In: *Journal of Cerebral Blood Flow and Metabolism* 4, pp. 484–499.

Horwitz, Barry (2003). "The elusive concept of brain connectivity". In: *NeuroImage* 19.2, pp. 466–470. ISSN: 10538119. DOI: 10.1016/S1053-8119(03)00112-5.

Hoy, A. R. and A. L. Alexander (2015). "Diffusion MRI". In: *Brain Mapping: An Encyclopedic Reference*. Vol. 1. Elsevier, pp. 47–52. ISBN: 9780123970251. DOI: 10.1016/B978-0-12-397025-1.00005-1.

Hsiao, Ing Tsung et al. (2012). "Correlation of early-phase 18F-florbetapir (AV-45/Amyvid) PET images to FDG images: Preliminary studies". In: *European Journal of Nuclear Medicine and Molecular Imaging* 39.4, pp. 613–620. ISSN: 16197070. DOI: 10.1007/s00259-011-2051-2.

Hudson, H Malcolm and Richard S Larkin (1994). "Ordered Subsets of Projection Data". In: *IEEE transactions on medical imaging* 13.4, pp. 601–609. ISSN: 0278-0062. DOI: 10.1109/42.363108.

Huisman, M C et al. (2012). "Cerebral blood flow and glucose metabolism in healthy volunteers measured using a high-resolution PET scanner". In: *European Journal of Nuclear Medicine and Molecular Imaging Research* 2.1, pp. 1–9. ISSN: 2191-219X. DOI: 10.1186/2191-219X-2-63.

Izquierdo-Garcia, D. et al. (2014). "An SPM8-Based Approach for Attenuation Correction Combining Segmentation and Nonrigid Template Formation: Application to Simultaneous PET/MR Brain Imaging". In: *Journal of*

Nuclear Medicine 55.11, pp. 1825–1830. ISSN: 0161-5505. DOI: 10.2967/jnumed.113.136341.

Janvin, Carmen Cristea et al. (2006). "Subtypes of mild cognitive impairment in Parkinson's disease: Progression to dementia". In: *Movement Disorders* 21.9, pp. 1343–1349. ISSN: 08853185. DOI: 10.1002/mds.20974.

Jeurissen, Ben et al. (2014). "Multi-tissue constrained spherical deconvolution for improved analysis of multi-shell diffusion MRI data". In: *NeuroImage* 103, pp. 411–426. ISSN: 10959572. DOI: 10.1016/j.neuroimage.2014.07.061.

Jezzard, P and R S Balaban (1995). "Correction for Geometric Distortion in Echo-Planar Images from B0 Field Variations". In: *Magnetic Resonance in Medicine* 34.1, pp. 65–73. ISSN: 0740-3194. DOI: 10.1002/mrm.1910340111.

Jezzard, Peter (2012). "Correction of geometric distortion in fMRI data". In: *NeuroImage* 62.2, pp. 648–651. ISSN: 10538119. DOI: 10.1016/j.neuroimage.2011.09.010.

Jo, Hang Joon, Stephen J. Gotts, et al. (2013). "Effective preprocessing procedures virtually eliminate distance-dependent motion artifacts in resting state FMRI". In: *Journal of Applied Mathematics* 2013. ISSN: 1110757X. DOI: 10.1155/2013/935154.

Jo, Hang Joon, Ziad S. Saad, et al. (2010). "Mapping sources of correlation in resting state FMRI, with artifact detection and removal". In: *NeuroImage* 52.2, pp. 571–582. ISSN: 10538119. DOI: 10.1016/j.neuroimage.2010.04.246.

Kawai, Nobuyuki et al. (2005). "Evaluation of tumor FDG transport and metabolism in primary central nervous system lymphoma using [lSF]fluorodeoxyglucose (FDG) positron emission tomography (PET) kinetic analysis". In: *Annals of Nuclear Medicine* 19.8, pp. 685–690.

Keereman, V., Y. Fierens, et al. (2010). "MRI-Based Attenuation Correction for PET/MRI Using Ultrashort Echo Time Sequences". In: *Journal of Nuclear Medicine* 51.5, pp. 812–818. ISSN: 0161-5505. DOI: 10.2967/jnumed.109.065425.

Keereman, V., P. Mollet, et al. (2013). "Challenges and current methods for attenuation correction in PET/MR". In: *Magnetic Resonance Materials in Physics, Biology and Medicine* 26.1, pp. 81–98. ISSN: 09685243. DOI: 10.1007/s10334-012-0334-7.

Kinahan, P E et al. (1998). "Attenuation correction for a combined 3D PET / CT scanner Attenuation correction for a combined 3D PET / CT scanner". In: 2046.1998, pp. 2046–2053. DOI: 10.1118/1.598392.

Kisler, Kassandra et al. (2017). "Cerebral blood flow regulation and neurovascular dysfunction in Alzheimer disease". In: *Nature Reviews Neuroscience* 18.7, pp. 419–434. ISSN: 1471-003X. DOI: 10.1038/nrn.2017.48.

Krejza, Jaroslaw et al. (2006). "Carotid artery diameter in men and women and the relation to body and neck size". In: *Stroke* 37.4, pp. 1103–1105. ISSN: 00392499. DOI: 10.1161/01.STR.0000206440.48756.f7.

Krzanowski, W. J. (1993). "Permutational tests for correlation matrices". In: *Statistics and Computing* 3.1, pp. 37–44. ISSN: 09603174. DOI: 10.1007/BF00146952.

Ladefoged, Claes N. et al. (2017). "A multi-centre evaluation of eleven clinically feasible brain PET/MRI attenuation correction techniques using a large cohort of patients". In: *NeuroImage* 147.December 2016, pp. 346–359. ISSN: 10959572. DOI: 10.1016/j.neuroimage.2016.12.010.

Lammertsma, Adriaan A. (2002). "Radioligand studies: Imaging and quantitative analysis". In: *European Neuropsychopharmacology* 12.6, pp. 513–516. ISSN: 0924977X.

Lang, E. W. et al. (2012). "Brain connectivity analysis: A short survey". In: *Computational Intelligence and Neuroscience* 2012.iii. ISSN: 16875265. DOI: 10.1155/2012/412512.

Lebedev, Alexander V. et al. (2014). "Large-scale resting state network correlates of cognitive impairment in Parkinson's disease and related dopaminergic deficits". In: *Frontiers in Systems Neuroscience* 8.April, pp. 1–12. ISSN: 1662-5137. DOI: 10.3389/fnsys.2014.00045.

Lee, M H, C D Smyser, and J S Shimony (2013). "Resting-state fMRI: a review of methods and clinical applications." In: *AJNR. American journal of neuroradiology* 34.10, pp. 1866–72. ISSN: 1936-959X. DOI: 10.3174/ajnr.A3263.

Lee, Tzu C. et al. (2016). "Morphology supporting function: attenuation correction for SPECT/CT, PET/CT, and PET/MR imaging". In: *Q J Nucl Med Mol Imaging* 60.1, pp. 25–39.

Legéndy, C R (1975). "Three principles of brain function and structure." In: *The International journal of neuroscience* 6.5, pp. 237–54. ISSN: 0020-7454. DOI: 10.3109/00207457509149497.

Leinonen, Ville et al. (2014). "Diagnostic effectiveness of quantitative [18F]flutemetamol PET imaging for detection of fibrillar amyloid β using cortical biopsy histopathology as the standard of truth in subjects with idiopathic normal pressure hydrocephalus". In: *Acta Neuropathologica Communications* 2.1, p. 46. ISSN: 2051-5960. DOI: 10.1186/2051-5960-2-46.

Li, Xianjin and Kewei Chen (2000). "Optimal image sampling schedule for both image-derived input and output functions in PET cardiac studies". In: *IEEE Transactions on Medical Imaging* 19.3, pp. 233–242. ISSN: 02780062. DOI: 10.1109/42.845181.

Liang, X. et al. (2013). "Coupling of functional connectivity and regional cerebral blood flow reveals a physiological basis for network hubs of the human brain". In: *Proceedings of the National Academy of Sciences* 110.5, pp. 1929–1934. ISSN: 0027-8424. DOI: 10.1073/pnas.1214900110.

Lopes, Renaud et al. (2017). "Cognitive phenotypes in parkinson's disease differ in terms of brain-network organization and connectivity". In: *Human Brain Mapping* 38.3, pp. 1604–1621. ISSN: 10970193. DOI: 10.1002/hbm.23474.

Lou, Wutao et al. (2016). "Changes of cerebral perfusion and functional brain network organization in patients with mild cognitive impairment". In: *Journal of Alzheimer's Disease* 54.1, pp. 397–409. ISSN: 18758908. DOI: 10.3233/JAD-160201.

Lowe, Val J. et al. (2017). "Comparison of [18F]Flutemetamol and [11C]Pittsburgh Compound-B in cognitively normal young, cognitively normal elderly, and Alzheimer's disease dementia individuals". In: *NeuroImage: Clinical* 16.August, pp. 295–302. ISSN: 22131582. DOI: 10.1016/j.nicl.2017.08.011.

Lucignani, G. et al. (1993). "Measurement of regional cerebral glucose utilization with fluorine-18-FDG and PET in heterogeneous tissues: theoretical considerations and practical procedure". In: *Journal of Nuclear Medicine* 34.3, pp. 360–369. ISSN: 0161-5505.

Lundman, Josef A et al. (2017). "Effect of gradient field nonlinearity distortions in MRI-based attenuation maps for PET reconstruction". In: *Physica Medica* 35, pp. 1–6. ISSN: 1724191X. DOI: 10.1016/j.ejmp.2017.02.019.

Maquet, Pierre et al. (1990). "Reproducibility of cerebral glucose utilization measured by PET and the [18F]-2-fluoro-2-deoxy-d-glucose method in resting, healthy human subjects". In: *European Journal of Nuclear Medicine* 16.4-6, pp. 267–273. ISSN: 03406997. DOI: 10.1007/BF00842779.

Marcus, Daniel S. et al. (2011). "Informatics and Data Mining Tools and Strategies for the Human Connectome Project". In: *Frontiers in Neuroinformatics* 5.June, pp. 1–12. ISSN: 1662-5196. DOI: 10.3389/fninf.2011.00004.

Martinez-Moller, A. et al. (2009). "Tissue Classification as a Potential Approach for Attenuation Correction in Whole-Body PET/MRI: Evaluation

with PET/CT Data". In: *Journal of Nuclear Medicine* 50.4, pp. 520–526. ISSN: 0161-5505. DOI: 10.2967/jnumed.108.054726.

Mattsson, N. et al. (2014). "Association of brain amyloid-β with cerebral perfusion and structure in Alzheimer's disease and mild cognitive impairment". In: *Brain* 137.5, pp. 1550–1561. ISSN: 14602156. DOI: 10.1093/brain/awu043.

McKeith, I. G. et al. (2005). "Diagnosis and management of dementia with Lewy bodies: Third report of the DLB consortium". In: *Neurology* 65.12, pp. 1863–1872. ISSN: 00283878. DOI: 10.1212/01.wnl.0000187889.17253.b1.

Mehranian, Abolfazl, Hossein Arabi, and Habib Zaidi (2016). "Vision 20/20: Magnetic resonance imaging-guided attenuation correction in PET/MRI: Challenges, solutions, and opportunities". In: *Medical Physics* 43.3, pp. 1130–1155. ISSN: 00942405. DOI: 10.1118/1.4941014.

Meyer, P. T. et al. (2011). "Dual-Biomarker Imaging of Regional Cerebral Amyloid Load and Neuronal Activity in Dementia with PET and 11C-Labeled Pittsburgh Compound B". In: *Journal of Nuclear Medicine* 52.3, pp. 393–400. ISSN: 0161-5505. DOI: 10.2967/jnumed.110.083683.

Mijalkov, Mite et al. (2017). "BRAPH: A Graph Theory Software for the Analysis of Brain Connectivity". In: *Plos one* 12.8. Ed. by Satoru Hayasaka. ISSN: 1932-6203. DOI: http://dx.doi.org/10.1101/106625.

Mikhno, A. et al. (2008). "Voxel-Based Analysis of 11C-PIB Scans for Diagnosing Alzheimer's Disease". In: *Journal of Nuclear Medicine* 49.8, pp. 1262–1269. ISSN: 0161-5505. DOI: 10.2967/jnumed.107.049932.

Miller-Thomas, Michelle M. and Tammie L.S. Benzinger (2017). "Neurologic Applications of PET/MR Imaging". In: *Magnetic Resonance Imaging Clinics of North America* 25.2, pp. 297–313. ISSN: 15579786. DOI: 10.1016/j.mric.2016.12.003.

Monchi, Oury, Alexandru Hanganu, and Pierre Bellec (2016). "Markers of cognitive decline in PD: The case for heterogeneity". In: *Parkinsonism and Related Disorders* 24, pp. 8–14. ISSN: 18735126. DOI: 10.1016/j.parkreldis.2016.01.002.

Mosconi, Lisa et al. (2007). "Quantitation, regional vulnerability, and kinetic modeling of brain glucose metabolism in mild Alzheimer's disease". In: *European Journal of Nuclear Medicine and Molecular Imaging* 34.9, pp. 1467–1479. ISSN: 16197070. DOI: 10.1007/s00259-007-0406-5.

Mountz, James M. et al. (2015). "Comparison of qualitative and quantitative imaging characteristics of [11C]PiB and [18F]flutemetamol in normal

control and Alzheimer's subjects". In: *NeuroImage: Clinical* 9, pp. 592–598. ISSN: 22131582. DOI: 10.1016/j.nicl.2015.10.007.

Mourik, J. E M et al. (2009). "Image-derived input functions for PET brain studies". In: *European Journal of Nuclear Medicine and Molecular Imaging* 36.3, pp. 463–471. ISSN: 16197070. DOI: 10.1007/s00259-008-0986-8.

Muzic, Raymond F. and Frank P. DiFilippo (2015). "PET/MRI - Technical Review". In: 49.3, pp. 242–254. DOI: 10.1053/j.ro.2014.10.001.

Nelissen, Natalie et al. (2008). "Kinetic Modelling in Human Brain Imaging". In: *Positron emission tomography—current clinical and research aspects, InTech*, pp. 55–84. DOI: 10.5772/30052.

Nelissen, N. et al. (2009). "Phase 1 Study of the Pittsburgh Compound B Derivative 18F-Flutemetamol in Healthy Volunteers and Patients with Probable Alzheimer Disease". In: *Journal of Nuclear Medicine* 50.8, pp. 1251–1259. DOI: 10.2967/jnumed.109.063305.

Novikov, Dmitry S., Valerij G. Kiselev, and Sune N. Jespersen (2018). "On modeling". In: *Magnetic Resonance in Medicine* 79.6, pp. 3172–3193. ISSN: 15222594. DOI: 10.1002/mrm.27101.

Nuyts, Johan et al. (2013). "Completion of a truncated attenuation image from the attenuated PET emission data". In: *IEEE Transactions on Medical Imaging* 32.2, pp. 237–246. ISSN: 02780062. DOI: 10.1109/TMI.2012.2220376.

Ogawa, S et al. (1990). "Brain magnetic resonance imaging with contrast dependent on blood oxygenation." In: *Proceedings of the National Academy of Sciences of the United States of America* 87.24, pp. 9868–72. ISSN: 0027-8424. DOI: 10.1073/pnas.87.24.9868.

Oppenheim, Alan V., Alan S. Willsky, and Syed Hamid. Nawab (1997). *Signals and Systems*. Prentice Hall, p. 957. ISBN: 9780138147570.

O'Sullivan, F. et al. (2010). "Kinetic quantitation of cerebral pet-fdg studies without concurrent blood sampling: Statistical recovery of the arterial input function". In: *IEEE Transactions on Medical Imaging* 29.3, pp. 610–624. ISSN: 02780062. DOI: 10.1109/TMI.2009.2029096.

Pasquini, Lorenzo et al. (2017). "Individual Correspondence of Amyloid-β and Intrinsic Connectivity in the Posterior Default Mode Network Across Stages of Alzheimer's Disease". In: *Journal of Alzheimer's Disease* 58.3, pp. 763–773. ISSN: 18758908. DOI: 10.3233/JAD-170096.

Paulus, D. H., L. Tellmann, and H. H. Quick (2013). "Towards improved hardware component attenuation correction in PET/MR hybrid imaging". In: *Physics in Medicine and Biology* 58.22, pp. 8021–8040. ISSN: 13616560. DOI: 10.1088/0031-9155/58/22/8021.

Paulus, Daniel H. and Harald H. Quick (2016). "Hybrid Positron Emission Tomography/Magnetic Resonance Imaging: Challenges, Methods, and State of the Art of Hardware Component Attenuation Correction". In: *Investigative Radiology* 51.10, pp. 624–634. ISSN: 15360210. DOI: 10.1097/RLI.0000000000000289.

Peraza, Luis R. et al. (2015). "Resting state in Parkinson's disease dementia and dementia with Lewy bodies: Commonalities and differences". In: *International Journal of Geriatric Psychiatry* 30.11, pp. 1135–1146. ISSN: 10991166. DOI: 10.1002/gps.4342.

Peruzzo, Denis et al. (2011). "Automatic selection of arterial input function on dynamic contrast-enhanced MR images". In: *Computer Methods and Programs in Biomedicine* 104.3, e148–e157. ISSN: 01692607. DOI: 10.1016/j.cmpb.2011.02.012. URL: http://dx.doi.org/10.1016/j.cmpb.2011.02.012.

Petrou, Myria et al. (2012). "Aβ-Amyloid deposition in patients with parkinson disease at risk for development of dementia". In: *Neurology* 79.11, pp. 1161–1167. ISSN: 00283878. DOI: 10.1212/WNL.0b013e3182698d4a.

Phelps, M. E. et al. (1979). "Tomographic measurement of local cerebral glucose metabolic rate in humans with (F-18)2-fluoro-2-deoxy-D-glucose: Validation of method". In: *Annals of Neurology* 6.5, pp. 371–388. ISSN: 15318249. DOI: 10.1002/ana.410060502.

Pichler, B. J. et al. (2008). "Positron Emission Tomography/Magnetic Resonance Imaging: The Next Generation of Multimodality Imaging?" In: *Seminars in Nuclear Medicine* 38.3, pp. 199–208. ISSN: 00012998. DOI: 10.1053/j.semnuclmed.2008.02.001.

Pirotte, Benoît et al. (2006). "Integrated positron emission tomography and magnetic resonance imaging–guided resection of brain tumors: a report of 103 consecutive procedures". In: *Journal of Neurosurgery* 104.2, pp. 238–253. ISSN: 0022-3085. DOI: 10.3171/jns.2006.104.2.238. URL: http://thejns.org/doi/10.3171/jns.2006.104.2.238.

Popescu, L.M., S. Matej, and R.M. Lewitt (2004). "Iterative image reconstruction using geometrically ordered subsets with list-mode data". In: *IEEE Symposium Conference Record Nuclear Science 2004.* Vol. 6. IEEE, pp. 3536–3540. ISBN: 0-7803-8700-7. DOI: 10.1109/NSSMIC.2004.1466649.

Potgieser, A. R. E. et al. (2014). "The role of diffusion tensor imaging in brain tumor surgery: a review of the literature." In: *Clinical neurology and neurosurgery* 124, pp. 51–8. ISSN: 1872-6968. DOI: 10.1016/j.clineuro.2014.06.009.

Power, Jonathan D., Kelly A. Barnes, et al. (2012). "Spurious but systematic correlations in functional connectivity MRI networks arise from subject motion". In: *NeuroImage* 59.3, pp. 2142–2154. ISSN: 10538119. DOI: https://doi.org/10.1093/cercor/bhs352.

Power, Jonathan D., A. Mitra, et al. (2014). "Methods to detect, characterize, and remove motion artifact in resting state fMRI". In: *NeuroImage* 84, pp. 320–341. ISSN: 10538119. DOI: 10.1016/j.neuroimage.2013.08.048.

Power, Jonathan D., Bradley L. Schlaggar, and Steven E. Petersen (2015). *Recent progress and outstanding issues in motion correction in resting state fMRI*. DOI: 10.1016/j.neuroimage.2014.10.044.

Price, Julie C et al. (2005). "Kinetic modeling of amyloid binding in humans using PET imaging and Pittsburgh Compound-B." In: *Journal of Cerebral Blood Flow and Metabolism* 25.11, pp. 1528–47. DOI: 10.1038/sj.jcbfm.9600146.

Qi, Jinyi and Richard M Leahy (2006). *Iterative reconstruction techniques in emission computed tomography*. DOI: 10.1088/0031-9155/51/15/R01.

Qiu, Maolin et al. (2017). "Multi-modal analysis of functional connectivity and cerebral blood flow reveals shared and unique effects of propofol in large-scale brain networks". In: *NeuroImage* 148.January, pp. 130–140. ISSN: 10959572. DOI: 10.1016/j.neuroimage.2016.12.080.

Quick, Harald H. (2014). "Integrated PET/MR". In: *Journal of Magnetic Resonance Imaging* 39.2, pp. 243–258. ISSN: 10531807. DOI: 10.1002/jmri.24523.

Rapisarda, E et al. (2010). "Image-based point spread function implementation in a fully 3D OSEM reconstruction algorithm for PET". In: *Physics in Medicine and Biology* 55.14, pp. 4131–4151. ISSN: 00319155. DOI: 10.1088/0031-9155/55/14/012.

Raylman, Raymond R., John M. Caraher, and Gary D Hutchins (1993). "Sampling requirements for dynamic cardiac PET studies using image-derived input functions." In: *Journal of nuclear medicine : official publication, Society of Nuclear Medicine* 34.3, pp. 440–447. ISSN: 0161-5505.

Raylman, Raymond R., Stan Majewski, et al. (2006). "Simultaneous MRI and PET imaging of a rat brain". In: *Physics in Medicine and Biology* 51.24, pp. 6371–6379. ISSN: 00319155. DOI: 10.1088/0031-9155/51/24/006.

Reilhac, Anthonin et al. (2008). "Simulation-based evaluation of OSEM iterative reconstruction methods in dynamic brain PET studies". In: *NeuroImage* 39.1, pp. 359–368. ISSN: 10538119. DOI: 10.1016/j.neuroimage.2007.07.038.

Reivich, M. et al. (1985). "Glucose metabolic rate kinetic model parameter determination in humans: the lumped constants and rate constants for [18F]fluorodeoxyglucose and [11C]deoxyglucose." In: *Journal of Cerebral Blood Flow and Metabolism* 5.2, pp. 179–192. ISSN: 0271-678X. DOI: 10.1038/jcbfm.1985.24.

Renkin, EM (1959). "Transport of potassium-42 from blood to tissue in isolated mammalian skeletal muscles". In: *Am J Physiol* 197.6, pp. 1205–1210. ISSN: 0002-9513. DOI: 10.1152/ajplegacy.1959.197.6.1205.

Renvall, Ville, Cathy Nangini, and Riitta Hari (2014). "All that glitters is not BOLD: Inconsistencies in functional MRI". In: *Scientific Reports* 4. ISSN: 20452322. DOI: 10.1038/srep03920.

Riedl, Valentin et al. (2016). "Metabolic connectivity mapping reveals effective connectivity in the resting human brain". In: *Proceedings of the National Academy of Sciences* 113.8, E1127–E1127. ISSN: 0027-8424. DOI: 10.1073/pnas.1600692113. URL: http://www.pnas.org/lookup/doi/10.1073/pnas.1600692113.

Riedl, V. et al. (2014). "Local Activity Determines Functional Connectivity in the Resting Human Brain: A Simultaneous FDG-PET/fMRI Study". In: *Journal of Neuroscience* 34.18, pp. 6260–6266. ISSN: 0270-6474. DOI: 10.1523/JNEUROSCI.0492-14.2014. URL: http://www.jneurosci.org/cgi/doi/10.1523/JNEUROSCI.0492-14.2014.

Rocca, M. A., E. De Meo, and M. Filippi (2016). "Functional MRI in investigating cognitive impairment in multiple sclerosis". In: *Acta Neurologica Scandinavica* 134.July, pp. 39–46. ISSN: 16000404. DOI: 10.1111/ane.12654.

Rocca, M. et al. (2012). "Large-scle neuronal network dysfunction in relapsing-remitting multiple sclerosis." In: *Neurology*, pp. 1449–1458.

Rodell, Anders B. et al. (2017). "Cerebral blood flow and Aβ-amyloid estimates by WARM analysis of [11C]PiB uptake distinguish among and between neurodegenerative disorders and aging". In: *Frontiers in Aging Neuroscience* 8.JAN, pp. 1–11. ISSN: 16634365. DOI: 10.3389/fnagi.2016.00321.

Rodriguez-Vieitez, Elena et al. (2017). "Comparability of [(18)F]THK5317 and [(11)C]PIB blood flow proxy images with [(18)F]FDG positron emission tomography in Alzheimer's disease." In: *Journal of Cerebral Blood Flow and Metabolism* 37.2, pp. 740–749. ISSN: 1559-7016. DOI: 10.1177/0271678X16645593.

Rodriguez-Vieitez, E. et al. (2016). "Comparison of Early-Phase 11C-Deuterium-L-Deprenyl and 11C-Pittsburgh Compound B PET for Assessing Brain Perfusion in Alzheimer Disease". In: *Journal of Nuclear Medicine* 57.7, pp. 1071–1077. ISSN: 0161-5505. DOI: 10.2967/jnumed.115.168732.

Rubinov, M. and O. Sporns (2010). "Complex network measures of brain connectivity: Uses and interpretations". In: *NeuroImage* 52.3, pp. 1059–1069. ISSN: 10538119. DOI: 10.1016/j.neuroimage.2009.10.003.

Saha, Gopal B. (2010). *Basics of PET Imaging*. Springer, New York, NY. ISBN: 978-1-4419-0804-9. DOI: 10.1007/978-1-4419-0805-6.

Sander, C. Y. et al. (2013). "Neurovascular coupling to D2/D3 dopamine receptor occupancy using simultaneous PET/functional MRI". In: *Proceedings of the National Academy of Sciences* 110.27, pp. 11169–11174. ISSN: 0027-8424. DOI: 10.1073/pnas.1220512110.

Sari, Hasan et al. (2017). "Estimation of an image derived input function with MR-defined carotid arteries in FDG-PET human studies using a novel partial volume correction method". In: 37.4, pp. 1398–1409. DOI: 10.1177/0271678X16656197.

Savio, Alexandre et al. (2017). "Resting-State Networks as Simultaneously Measured with Functional MRI and PET". In: *Journal of Nuclear Medicine* 58.8, pp. 1314–1317. ISSN: 0161-5505. DOI: 10.2967/jnumed.116.185835.

Schlyer, D. et al. (2007). "A simultaneous PET/MRI scanner based on RatCAP in small animals". In: *IEEE Nuclear Science Symposium Conference Record* 5, pp. 3256–3259. ISSN: 10957863. DOI: 10.1109/NSSMIC.2007.4436833.

Schmidt, K C and F E Turkheimer (2002). "Kinetic modeling in positron emission tomography." In: *The quarterly journal of nuclear medicine : official publication of the Italian Association of Nuclear Medicine (AIMN) [and] the International Association of Radiopharmacology (IAR)* 46.1, pp. 70–85. ISSN: 1125-0135. DOI: 10.1016/B978-012744482-6.50026-0.

Schmidt, K. et al. (1992). "Errors introduced by tissue heterogeneity in estimation of local cerebral glucose utilization with current kinetic models of the [18F]fluorodeoxyglucose method". In: *Journal of Cerebral Blood Flow*

and Metabolism 12.5, pp. 823–834. ISSN: 0271678X. DOI: 10.1038/jcbfm.1992.114.

Schoonheim, Menno M et al. (2015). "Thalamus structure and function determines severity of cognitive impairment in multiple sclerosis". In: *Neurology* 84.8, pp. 776–783. ISSN: 1526-632X. DOI: 10.1212/WNL.0000000000001285.

Schuff, Norbert et al. (2009). "Cerebral blood flow in ischemic vascular dementia and Alzheimer's disease, measured by arterial spin-labeling magnetic resonance imaging". In: *Alzheimer's and Dementia* 5.6, pp. 454–462. ISSN: 15525260. DOI: 10.1016/j.jalz.2009.04.1233.

Ségonne, F., A. M. Dale, et al. (2004). "A hybrid approach to the skull stripping problem in MRI". In: *NeuroImage* 22.3, pp. 1060–1075. ISSN: 10538119. DOI: 10.1016/j.neuroimage.2004.03.032.

Ségonne, F., Jenni Pacheco, and Bruce Fischl (2007). "Geometrically accurate topology-correction of cortical surfaces using nonseparating loops". In: *IEEE Transactions on Medical Imaging* 26.4, pp. 518–529. ISSN: 02780062. DOI: 10.1109/TMI.2006.887364.

Sekine, T. et al. (2016). "Clinical Evaluation of Zero-Echo-Time Attenuation Correction for Brain 18F-FDG PET/MRI: Comparison with Atlas Attenuation Correction". In: *Journal of Nuclear Medicine* 57.12, pp. 1927–1932. ISSN: 0161-5505. DOI: 10.2967/jnumed.116.175398.

Setsompop, K. et al. (2012). "Improving diffusion MRI using simultaneous multi-slice echo planar imaging". In: *NeuroImage* 63.1, pp. 569–580. ISSN: 10538119. DOI: 10.1016/j.neuroimage.2012.06.033.

Sheffield, Julia M. and Deanna M. Barch (2016). *Cognition and resting-state functional connectivity in schizophrenia*. DOI: 10.1016/j.neubiorev.2015.12.007.

Sheline, Yvette I et al. (2010). "Resting-state functional MRI in depression unmasks increased connectivity between networks via the dorsal nexus". In: *Proceedings of the National Academy of Sciences* 107.24, pp. 11020–11025. ISSN: 0027-8424. DOI: 10.1073/pnas.1000446107.

Shi, Kuangyu et al. (2017). "Individual refinement of attenuation correction maps for hybrid PET/MR based on multi-resolution regional learning". In: *Computerized Medical Imaging and Graphics* 60, pp. 50–57. ISSN: 18790771. DOI: 10.1016/j.compmedimag.2016.11.005.

Siegel, J. S. et al. (2015). "The effects of hemodynamic lag on functional connectivity and behavior after stroke". In: *Journal of Cerebral Blood Flow & Metabolism*, p. 0271678X15614846. ISSN: 1559-7016. DOI: 10.1177/0271678X15614846.

Siegel, Joshua S., Anish Mitra, et al. (2016). "Data Quality Influences Observed Links Between Functional Connectivity and Behavior". In: *Cerebral Cortex*, pp. 1–11. ISSN: 1047-3211. DOI: 10.1093/cercor/bhw253.

Siegel, Joshua S., Jonathan D. Power, et al. (2014). "Statistical improvements in functional magnetic resonance imaging analyses produced by censoring high-motion data points". In: *Human Brain Mapping* 35.5, pp. 1981–1996. ISSN: 10970193. DOI: 10.1002/hbm.22307.

Sierra-Marcos, Alba (2017). "Regional Cerebral Blood Flow in Mild Cognitive Impairment and Alzheimer's Disease Measured with Arterial Spin Labeling Magnetic Resonance Imaging". In: *International Journal of Alzheimer's Disease* 2017, pp. 1–10. ISSN: 2090-8024. DOI: 10.1155/2017/5479597.

Singh, S. et al. (2015). "Disrupted Functional Connectivity in Schizophrenia: a Resting State Fmri Study". In: *European Psychiatry* 30, p. 907. ISSN: 09249338. DOI: 10.1016/S0924-9338(15)30707-0.

Sled, J G, a P Zijdenbos, and a C Evans (1998). "A nonparametric method for automatic correction of intensity nonuniformity in MRI data." In: *IEEE transactions on medical imaging* 17.1, pp. 87–97. ISSN: 0278-0062. DOI: 10.1109/42.668698.

Smith, Robert E. et al. (2012). "Anatomically-constrained tractography: Improved diffusion MRI streamlines tractography through effective use of anatomical information". In: *NeuroImage* 62.3, pp. 1924–1938. ISSN: 10538119. DOI: 10.1016/j.neuroimage.2012.06.005.

— (2013). "SIFT: Spherical-deconvolution informed filtering of tractograms". In: *NeuroImage* 67, pp. 298–312. ISSN: 10538119. DOI: 10.1016/j.neuroimage.2012.11.049.

Smith, Stephen M., Christian F. Beckmann, et al. (2013). "Resting-state fMRI in the Human Connectome Project". In: *NeuroImage* 80, pp. 144–168. ISSN: 10538119. DOI: 10.1016/j.neuroimage.2013.05.039.

Smith, Stephen M., Mark Jenkinson, et al. (2004). "Advances in functional and structural MR image analysis and implementation as FSL". In: *NeuroImage*. Vol. 23. SUPPL. 1, S208–S219. DOI: 10.1016/j.neuroimage.2004.07.051.

Sokoloff, L. et al. (1977). "The [14 C]Deoxyglucose Method for the Measurement of Local Cerebral Glucose Utilization: Theory, Procedure, and Normal Values in the Conscious and Anesthetized Albino Rat". In: *Journal of Neurochemistry* 28.5, pp. 897–916. ISSN: 0022-3042. DOI: 10.1111/j.1471-4159.1977.tb10649.x.

Sours, Chandler et al. (2015). "Disruptions in resting state functional connectivity and cerebral blood flow in mild traumatic brain injury patients". In: *PLoS ONE* 10.8, pp. 1–20. ISSN: 19326203. DOI: 10.1371/journal.pone.0134019.

Tahmasian, M. et al. (2016). "Based on the Network Degeneration Hypothesis: Separating Individual Patients with Different Neurodegenerative Syndromes in a Preliminary Hybrid PET/MR Study". In: *Journal of Nuclear Medicine* 57.3, pp. 410–415. ISSN: 0161-5505. DOI: 10.2967/jnumed.115.165464.

Tatu, L. et al. (1999). "Arterial territories of the human brain." In: *Front Neurol Neurosci.* 30, pp. 99–110. DOI: 10.1159/000333602.

Taylor, Alexander N.W., Lana Kambeitz-Ilankovic, Benno Gesierich, Lee Simon-Vermot, Nicolai Franzmeier, Miguel Araque Caballero, et al. (2016). "Tract-specific white matter hyperintensities disrupt neural network function in Alzheimer's disease". In: *Alzheimer's and Dementia* 13.3, pp. 225–235. ISSN: 15525279. DOI: 10.1016/j.jalz.2016.06.2358.

Taylor, Alexander N.W., Lana Kambeitz-Ilankovic, Benno Gesierich, Lee Simon-Vermot, Nicolai Franzmeier, Miguel Á. Araque Caballero, et al. (2010). "Tract-specific white matter hyperintensities disrupt neural network function in Alzheimer's disease". In: *Alzheimer's & Dementia: The Journal of the Alzheimer's Association*, c3666–e36. ISSN: 1552-5260. DOI: 10.1016/j.jalz.2016.06.2358.

Thompson, Garth J. et al. (2016). "The Whole-Brain "Global" Signal from Resting State fMRI as a Potential Biomarker of Quantitative State Changes in Glucose Metabolism". In: *Brain Connectivity* 6.6, pp. 435–447. ISSN: 2158-0014. DOI: 10.1089/brain.2015.0394.

Tona, Francesca et al. (2014). "Multiple sclerosis: altered thalamic resting-state functional connectivity and its effect on cognitive function." In: *Radiology* 271.3, pp. 814–821. ISSN: 1527-1315. DOI: 10.1148/radiol.14131688.

Tonietto, Matteo, Gaia Rizzo, Mattia Veronese, and Alessandra Bertoldo (2015). "Modelling arterial input functions in positron emission tomography dynamic studies". In: *Proceedings of the Annual International Conference of the IEEE Engineering in Medicine and Biology Society, EMBS* 2015-Novem, pp. 2247–2250. ISSN: 1557170X. DOI: 10.1109/EMBC.2015.7318839.

Tonietto, Matteo, Gaia Rizzo, Mattia Veronese, Masahiro Fujita, et al. (2016). "Plasma radiometabolite correction in dynamic PET studies: Insights on

the available modeling approaches". In: *Journal of Cerebral Blood Flow and Metabolism* 36.2, pp. 326–339. ISSN: 15597016. DOI: 10.1177/0271678X15610585.

Tournier, Jacques Donald, Fernando Calamante, and Alan Connelly (2007). "Robust determination of the fibre orientation distribution in diffusion MRI: Non-negativity constrained super-resolved spherical deconvolution". In: *NeuroImage* 35.4, pp. 1459–1472. ISSN: 10538119. DOI: 10.1016/j.neuroimage.2007.02.016.

Tournier, Jacques Donald, Fernando Calamante, David G. Gadian, et al. (2004). "Direct estimation of the fiber orientation density function from diffusion-weighted MRI data using spherical deconvolution". In: *NeuroImage* 23.3, pp. 1176–1185. ISSN: 10538119. DOI: 10.1016/j.neuroimage.2004.07.037.

Tournier, Jacques Donald, Susumu Mori, and Alexander Leemans (2011). "Diffusion tensor imaging and beyond". In: *Magnetic Resonance in Medicine* 65.6, pp. 1532–1556. ISSN: 07403194. DOI: 10.1002/mrm.22924.

Turkheimer, Federico E., Mattia Veronese, and Joel Dunn (2014). *Experimental Design and Practical Data Analysis in POSITRON EMISSION TOMOGRAPHY*. CreateSpace Independent Publishing Platform; 1 edition. ISBN: 78-1-49929-582-5.

Tustison, Nicholas J. et al. (2010). "N4ITK: Improved N3 bias correction". In: *IEEE Transactions on Medical Imaging* 29.6, pp. 1310–1320. ISSN: 02780062. DOI: 10.1109/TMI.2010.2046908.

Tyler, J L et al. (1988). "Stability of regional cerebral glucose metabolism in the normal brain measured by positron emission tomography." In: *Journal of nuclear medicine : official publication, Society of Nuclear Medicine* 29.5, pp. 631–42. ISSN: 0161-5505.

Van Essen, David C. et al. (2001). "An Integrated Software Suite for Surface-based Analyses of Cerebral Cortex". In: *Journal of the American Medical Informatics Association* 8.5, pp. 443–459. ISSN: 1067-5027. DOI: 10.1136/jamia.2001.0080443.

Van Velden, F. H P et al. (2008). "Comparison of 3D-OP-OSEM and 3D-FBP reconstruction algorithms for High-Resolution Research Tomograph studies: Effects of randoms estimation methods". In: *Physics in Medicine and Biology* 53.12, pp. 3217–3230. ISSN: 00319155. DOI: 10.1088/0031-9155/53/12/010.

Vandenberghe, S. and P. K. Marsden (2015). "PET-MRI: a review of challenges and solutions in the development of integrated multimodality imaging".

In: *Physics in Medicine and Biology* 60.4, R115–R154. ISSN: 0031-9155. DOI: 10.1088/0031-9155/60/4/R115.

Vandenberghe, S., E. Mikhaylova, et al. (2016). "Recent developments in time-of-flight PET". In: *EJNMMI Physics* 3.1. ISSN: 21977364. DOI: 10.1186/s40658-016-0138-3.

Veraart, Jelle et al. (2016). "Denoising of diffusion MRI using random matrix theory". In: *NeuroImage* 142, pp. 394–406. ISSN: 10959572. DOI: 10.1016/j.neuroimage.2016.08.016.

Vidal, Benjamin et al. (2017). *The Journal of nuclear medicine : JNM*. Vol. 58. supplement 1. Society of Nuclear Medicine, pp. 11–11.

Wagenknecht, Gudrun et al. (2013). "MRI for attenuation correction in PET: Methods and challenges". In: *Magnetic Resonance Materials in Physics, Biology and Medicine* 26.1, pp. 99–113. ISSN: 09685243. DOI: 10.1007/s10334-012-0353-4.

Wald, L. L. and J. R. Polimeni (2015). "High-Speed, High-Resolution Acquisitions". In: *Brain Mapping: An Encyclopedic Reference*. Vol. 1. Elsevier, pp. 103–116. ISBN: 9780123970251. DOI: 10.1016/B978-0-12-397025-1.00011-7.

Wang, Kun et al. (2007). "Altered functional connectivity in early Alzheimer's disease: A resting-state fMRI study". In: *Human Brain Mapping* 28.10, pp. 967–978. ISSN: 10659471. DOI: 10.1002/hbm.20324.

Wang, Liang et al. (2009). "Altered small-world brain functional networks in children with attention-deficit/hyperactivity disorder". In: *Human Brain Mapping* 30.2, pp. 638–649. ISSN: 10659471. DOI: 10.1002/hbm.20530.

Wang, Sandhitsu R. Das, et al. (2011). "A learning-based wrapper method to correct systematic errors in automatic image segmentation: Consistently improved performance in hippocampus, cortex and brain segmentation". In: *NeuroImage* 55.3, pp. 968–985. ISSN: 10538119. DOI: 10.1016/j.neuroimage.2011.01.006.

Wang and P. A. Yushkevich (2013). "Groupwise segmentation with multi-atlas joint label fusion". In: *Lecture Notes in Computer Science (including subseries Lecture Notes in Artificial Intelligence and Lecture Notes in Bioinformatics)*. Vol. 8149 LNCS. PART 1, pp. 711–718. ISBN: 9783642408106. DOI: 10.1007/978-3-642-40811-3{_}89.

Wehrl, Hans F. et al. (2013). "Simultaneous PET-MRI reveals brain function in activated and resting state on metabolic, hemodynamic and multiple temporal scales". In: *Nat Med* 19.9, pp. 1184–1189. ISSN: 1546-170X. DOI: 10.1038/nm.3290.

Wiesinger, Florian et al. (2016). "Zero TE MR bone imaging in the head". In: *Magnetic Resonance in Medicine* 75.1, pp. 107–114. ISSN: 15222594. DOI: 10.1002/mrm.25545.

Wise, T. et al. (2017). "Instability of default mode network connectivity in major depression: A two-sample confirmation study". In: *Translational Psychiatry* 7.4, pp. 1105–7. ISSN: 21583188. DOI: 10.1038/tp.2017.40.

Wollenweber, Scott D. et al. (2013). "Evaluation of an atlas-based PET head attenuation correction using PET/CT & MR Patient Data". In: *IEEE Transactions on Nuclear Science* 60.5, pp. 3383–3390. ISSN: 00189499. DOI: 10.1109/TNS.2013.2273417.

Zaidi, Habib (2006). *Quantitative Analysis in Nuclear Medicine Imaging*. 4. Springer, p. 1522. ISBN: 9780387238548. DOI: 10.1118/1.2716416.

Zaidi, Habib and Bruce Hasegawa (2003). "Determination of the Attenuation Map in Emission Tomography". In: *Journal of Nuclear Medicine* 44.2, pp. 291–315. ISSN: 0161-5505, 2159-662X.

Zaidi, Habib, Marie Louise Montandon, and Abass Alavi (2007). *Advances in Attenuation Correction Techniques in PET*. DOI: 10.1016/j.cpet.2007.12.002.

Zanotti-Fregonara, Paolo et al. (2011). "Image-Derived Input Function for Brain PET Studies: Many Challenges and Few Opportunities". In: *Journal of Cerebral Blood Flow & Metabolism* 31.10, pp. 1986–1998. ISSN: 0271-678X. DOI: 10.1038/jcbfm.2011.107.

Zeng, Ling-Li et al. (2014). "Neurobiological basis of head motion in brain imaging." In: *Proceedings of the National Academy of Sciences of the United States of America* 111.16, pp. 6058–62. ISSN: 1091-6490. DOI: 10.1073/pnas.1317424111.

Zhan, Zhou-Wei et al. (2018). "Abnormal resting-state functional connectivity in posterior cingulate cortex of Parkinson's disease with mild cognitive impairment and dementia". In: *CNS Neuroscience & Therapeutics* November 2017, pp. 1–9. ISSN: 17555930. DOI: 10.1111/cns.12838.

Zhang, Hui et al. (2012). "NODDI: Practical in vivo neurite orientation dispersion and density imaging of the human brain". In: *NeuroImage* 61.4, pp. 1000–1016. ISSN: 10538119. DOI: 10.1016/j.neuroimage.2012.03.072.

Zhang, Nan, Marc L. Gordon, and Terry E. Goldberg (2017). "Cerebral blood flow measured by arterial spin labeling MRI at resting state in normal aging and Alzheimer's disease". In: *Neuroscience and Biobehavioral Reviews*

72, pp. 168–175. ISSN: 18737528. DOI: 10.1016/j.neubiorev.2016.11.023.

Zhou, Yongxia, Fang Yu, and Timothy Q Duong (2015). "White matter lesion load is associated with resting state functional MRI activity and amyloid PET but not FDG in mild cognitive impairment and early Alzheimer's disease patients." en. In: *Journal of magnetic resonance imaging : JMRI* 41.1, pp. 102–9. ISSN: 1522-2586. DOI: 10.1002/jmri.24550.

Zhou, Yuan et al. (2008). "Altered resting-state functional connectivity and anatomical connectivity of hippocampus in schizophrenia". In: *Schizophrenia Research* 100.1-3, pp. 120–132. ISSN: 09209964. DOI: 10.1016/j.schres.2007.11.039.

Zhu, Jiajia et al. (2017). "Altered Coupling between Resting-State Cerebral Blood Flow and Functional Connectivity in Schizophrenia". In: *Schizophrenia Bulletin* 43.6, pp. 1363–1374. ISSN: 17451701. DOI: 10.1093/schbul/sbx051.

Zhu, Xueling et al. (2017). "Rumination and Default Mode Network Subsystems Connectivity in First-episode, Drug-Naive Young Patients with Major Depressive Disorder". In: *Scientific Reports* 7.January, pp. 1–10. ISSN: 20452322. DOI: 10.1038/srep43105.